TOWARDS UNTETHERED SOFT ROBOTS DRIVEN BY ELECTROHYDRAULIC ARTIFICIAL MUSCLES

by

SHANE KARL MITCHELL

B.S. Dickinson College, 2014

M.S. University of Colorado Boulder, 2018

A thesis submitted to the

Faculty of the Graduate School of the

University of Colorado in partial fulfillment

of the requirement for the degree of

Doctor of Philosophy

Paul M. Rady Department of Mechanical Engineering

2020

Committee Members:

Christoph Keplinger

Jay McMahon

Gregory Whiting

Robert MacCurdy

Sean Humbert

Abstract

Mitchell, Shane Karl (Ph.D. Mechanical Engineering)

Towards untethered soft robots driven by electrohydraulic artificial muscles

Thesis directed by Assistant Professor Dr. Christoph Keplinger

As humans, we are continually integrating technology into our everyday lives. From wearable smart watches to autonomous vacuum cleaners, modern day machines are steadily moving out of warehouses and factories and into our homes to enhance our lifestyles. In doing so, there is an ever-growing need for machines that can safely operate in extremely diverse or unpredictable environments, which often includes collaborative spaces near humans. This requirement presents challenges for traditional robots that commonly employ rigid architectures driven by heavy motors, gears, and linkages, which rely on precise computation of the state at each degree of freedom to safely function. Moreover, the underlying mechanics of these modern-day robotic architectures are fundamentally different than those which have evolved naturally; biological organisms exploit a host of compliant, robust, and multifunctional structures that tightly integrate actuation, sensing, and control. These biological structures, in animals for instance, enable feats of strength, agility, and autonomy that are currently impossible for human-made robots.

A paradigm shift in robotic design and implementation is required for the next generation of machines. This approach will reinvent the idea of a robot, moving from a rigid block design to a soft continuum that integrates lightweight, compliant, and versatile components. While this approach will require multi-disciplinary advances in material science, control theory, and engineering, a fundamental component of these machines will ultimately be the actuators that drive

them. Thus, researchers and engineers are developing soft actuators that mimic the strength, speed, and scalability of natural muscle. These bio-inspired components could unlock a multitude of applications for machines, and even blur the lines between science and science fiction. For example, soft wearable robots can provide haptic feedback for an immersive virtual reality experience, ultra-adaptable soft robotic cephalopods could explore marine environments to conduct research and reconnaissance, while highly resilient space robots could explore extraterrestrial environments to uncover the origins of life.

This dissertation is focused on a novel type of soft actuator (or artificial muscle) called a Hydraulically Amplified Self-healing ELectrostatic (HASEL) actuator, and its application to soft robotics devices. The first chapter will explore the state-of-the-art in soft robotics technologies, with a focus on soft actuation. The second chapter will elucidate the fundamentals of HASEL actuators and their application to soft robotic technologies. The third chapter will detail a toolkit based on off-the-shelf-materials that can be used to prototype, fabricate, power, and test HASEL actuators. This chapter will detail exemplary designs of HASEL, their modes of actuation and performance, as well as their application to soft-robotic devices such as a continuum robot capable of grasping and manipulating delicate objects. Continuing to the fourth chapter, a novel design for a linearly contractile actuator is presented, characterized on both an experimental and theoretical basis, and then demonstrated as a soft tubular pump. In the fifth chapter, we develop a state-of-the-art 10-channel high voltage power supply to independently control groups of HASEL actuators. This power supply features a compact form-factor that is about the size of a standard smart phone. Next, chapter six will focus on soft robots for space exploration. A feasibility study details a robot design for asteroid mining, and initial prototypes are discussed with a focus on electrohydraulic actuation and electrostatic adhesion mechanisms for robot locomotion and

grappling. Finally, chapter seven concludes the dissertation with a summary of the developments presented here, while also laying the framework for future studies.

Acknowledgements

I am so grateful for the opportunities that have been given to me over the past 5.5 years as part of the Keplinger Research Group. Without the help of my amazing colleagues, none of the work presented in this dissertation would have been possible. First most, I would like to extend a resounding thank you to Christoph for his guidance and friendship. Without his continued belief in me, I certainly would not be where I am today. I would also like to applaud him for his extremely creative philosophy when it comes to lab work, which has undoubtedly instilled in me a passion for research that I never knew I had before I began working under his tutelage. Next, I would like to thank Timothy Morrissey for taking me under his wing when I first started in the lab and showing me how to conduct world class research with light-heartedness and determination. I will be forever thankful for our initial work together that inspired me to continue pursuing my education. I would also like to thank Eric Acome. Eric and I have collaborated on quite a bit of research over the past few years and I must say that he is one of the most dependable and patient people I know. It has been a true pleasure learning from you. And of course, a huge thank you to Nick Kellaris, whom I've also had the pleasure of working with on many projects over the course of my PhD. I always appreciate our impromptu brainstorming sessions, and your ability to communicate complicated material with patience and grace. I look forward to making the same jokes and finishing each other's sentences over the years to come.

I am honored to have co-founded the company Artimus Robotics with the gentlemen I've mentioned above. I look forward to working closely with them to change the way the world moves. Here's to many more hot wings and dad jokes.

Next, I would like to thank Xingrui Wang and Trent Martin who have both been integral to my first author publications. It was a pleasure learning about Chinese culture from Xingrui and I quite enjoyed our hot pot celebrations. Trent and I have been working together for close to 4 years when he began helping me as a first-year undergraduate. I was hesitant at first, only because Trent was relatively young and inexperienced, but my worries were soon placated as I witnessed his professional work in a research setting. You have a bright future ahead of you my friend!

I would also like to extend a special thank you to the upcoming PhD students in the Keplinger Research Group; namely, Ellen Rumley, Zach Yoder, Ingemar Schmidt, Gavriel Kleinwaks, Sophie Kirkman, and Hyeong-Joon Joo. While at times I may have seemed like a grumpy old 5th year who couldn't be bothered, I truly enjoyed mentoring all of you. I can't thank

you all enough for reminding me what it's like to be an eager and determined researcher trying to make a name for themselves. Never lose that passion and I cannot wait to see what exciting things you all accomplish in the years to come. The sky is the limit for each of you. Also, I would also like to thank Philipp Rothemund for kindly and patiently sharing his immense knowledge and theoretical understanding of HASEL technology.

Additionally, I would like to thank a few students from other labs who I have learned a great deal from in recent years. Thank you Vidyacharan (VC) Gopaluni Venkata, Khoi Ly, Mantas Naris, and Vani Sundaram. Also, I would like to thank my co-advisor Dr. Jay McMahon, whose unique perspective was always welcomed. I greatly enjoyed our conversations at the 2019 NIAC symposium, and I hope we can find a way to continue working together in the future.

Finally, I would like to thank my closest family members for all their support throughout the years. My mother has been a constant source of compassion and guidance, especially through dark times when I needed her the most. My father has always found a way to make me laugh while spurring my creativity and critical thinking; I am very fond of our wacky conversations about applications for HASEL technology. And to my brother, you are one of my closest friends and it is comforting to know that I can always talk to you about anything; I am very proud of you. Lastly, a special pst-pst thank you to my four-legged feline friends, Lynx and Tesla, whose unyielding friendship has enriched my life and taught me not to take the 'little things' for granted. You all inspire me to strive for greatness and I love you all very much.

I would like to thank my funding source, the NASA Innovative Advanced Concepts (NIAC) grant.

Table of Contents

List of Figures

List of Tables

1 Introduction

1.1 Soft robotics

Science fiction is rife with robots. Societies of the future are almost always portrayed with robots working closely alongside humans, or even integrated into human physiology. For example, the HBO Max series *Raised by Wolves* depicts humanoid robot caretakers that raise children on an Earth-like planet after the environmental collapse of Earth (Figure 1.1a). In the popular anime series and motion picture *Ghost in the Shell* the protagonist, Motoko Kusanagi, survives a near death experience, albeit her entire body is replaced by robotic materials affording her incredible agility and resilience, as well as the ability to camouflage her entire body to match her surroundings (Figure 1.1b). In fifth episode of the *Star Wars* saga, Luke Skywalker loses his right lower arm in a lightsaber battle and is given a robotic hand by a physician that is an android (Figure 1.1c).

Figure 1.1: Humanoid robots in popular science fiction. a) An image from the series *Raised by Wolves*. The series features an android caregiver called 'Mother' that must raise children to repopulate the human species. b) The main character in the movie *Ghost in the Shell* can completely camouflage her body with any environment. c) A robot physician tends to Luke Skywalker's prosthetic arm in *Star Wars: The Empire Strikes Back*.

While the above examples are fictitious, the scope of their stories predicts trends in the real-world. That is, robots are poised to influence the future generations on Earth by addressing climate change, labor shortages, providing health care for an aging population, and allowing humans to surpass our physical limitations. While robots today are impressive in their capabilities—especially in controlled environments such as an assembly line in a factory—they

are often ill-suited in unstructured environments and can be dangerous for humans in collaborative situations. In order to realize a future in which robots can adapt to changing tasks and environments, we need machines that are extremely versatile in terms of their decision making and that are based on robotic hardware that can dynamically respond in a variety of situations.

The field of soft robotics challenges the conventional definition of a robot by substituting motors, gears, and metal with more compliant and multifunctional components inspired by those found in biological systems (*1–3*). Soft robots offer an intrinsic adaptability, dexterity, and shock-absorbance that makes them well-suited for safe operation near humans and in unpredictable environments. These features open applications for robots in wearable, surgical, and collaborative robotics (*1*, *4–7*). Moreover, these lightweight and versatile machines can find utility in aerospace and marine engineering, industrial processing and automation, and active camouflaging, Figure 1.2 (*2*, *8–10*).

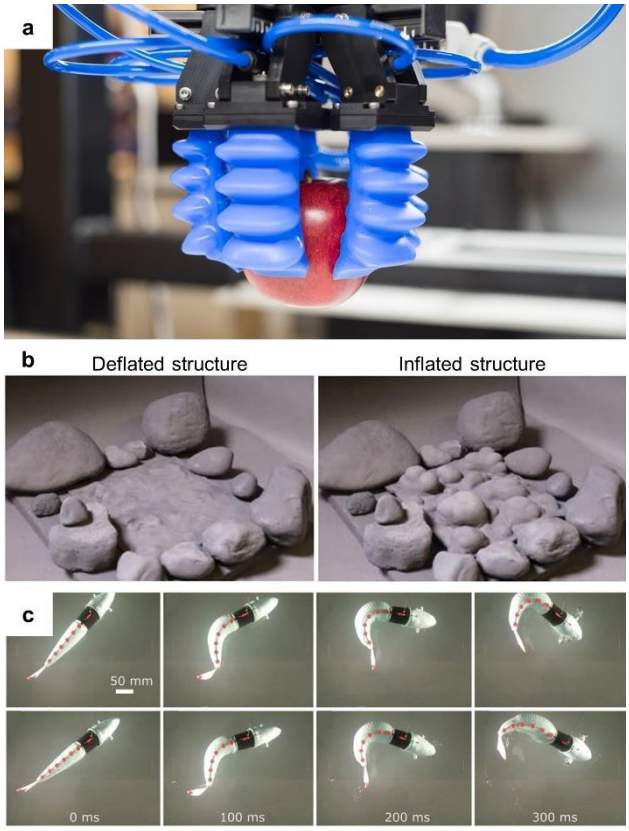

Figure 1.2: Examples of soft robotic technologies. a) The company *Soft Robotics Inc.* specializes in pneumatic end effectors for picking and packaging in industrial automation. b) Stone-shaped active camouflage using stretchable surfaces with programmable 3D texture morphing (*10*). c) A fluidically driven, autonomous soft robotic fish performing a sequence of escape maneuvers (*11*).

1.2 Soft actuators

Soft actuators that mimic the universal performance of natural muscle (*12*, *13*) are critical components for creating the next generation of soft robots that achieve levels of functionality seen only in biological systems. Natural muscle is a marvel of evolution; it enables the rapid wing-flapping rates of a hummingbird, it is strong enough to move an elephant, and it enables the complex motion of an octopus arm, whose versatility is still unmatched by human-made machines. Additionally, muscle continuously regenerates over the lifetime of an organism, heals after damage, and is seamlessly integrated with nerves for sensing (*14*).

Over the past few decades many researchers have attempted to replicate the performance of natural muscle with a synthetic system. One of the earliest examples of an artificial muscle is the McKibben pneumatic actuator in the 1950s, Figure 1.3a (*15*, *16*). This device utilizes a pressurized fluid (usually air or water) to drive shape change of a deformable architecture. McKibben actuators represent a subset of a larger class of soft actuators called soft fluidic actuators. These devices offer diverse modes of actuation (*1*, *15*, *17*, *18*), and an extremely large material and design freedom, Figure 1.3b-d. Soft fluidic actuators have been created using elastomers, thin-films, and even materials engineered to mechanically self-heal after being cut or punctured (*19*). Additionally, they can be manufactured using a variety of techniques like molding and additive manufacturing (*16*). However, pneumatic actuators typically have low efficiency (*20*) (ranging for 5-30%) and experience substantial trade-offs between actuation speed and portability. These actuators require a tether to sources of pressurized fluid, while high-power operation typically necessitates bulky reservoirs of pressurized fluid or compressors that are difficult to miniaturized (*21*, *22*).

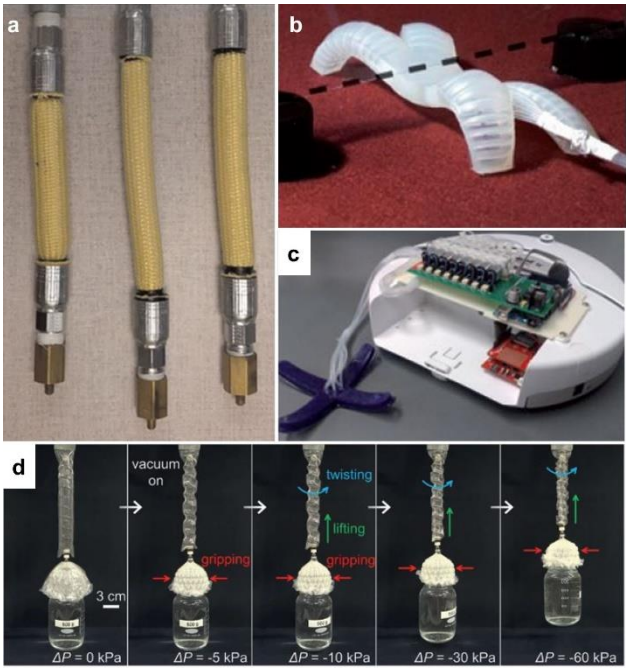

Figure 1.3: Soft fluidic actuators. a) Examples of McKibben actuators (*20*). b) A multi-gait quadruped based on channels of pneumatic networks (*23*). c) A hybrid robot that combines a wheeled hard robot with a pneumatic quadruped (*24*). d) Vacuum driven actuators harness origami for embedded intelligence. A bottle of water is grasped, lifted, and twisted (*17*).

Dielectric elastomer actuators (DEAs) (first introduced in 2000 (*25*)) are stretchable capacitors (Figure 1.4a) that employ electrostatic activation to achieve large actuation strain, high-speed operation, and self-sensing capabilities enabling closed-loop control (*26–29*). DEA devices have been explored for a number of applications including soft grippers, soft motors, antagonist muscle pairs, and active braille displays, to name a few, Figure 1.4b,c (*30–33*). Additionally, the direct electrical activation of DEAs promotes the use of portable driving electronics for untethered robotic applications, Figure 1.4d (*34–36*). Although DEAs have remarkable performance on paper, they suffer from a lack of reliability due to premature failure from dielectric breakdown when scaled to large activation areas (*37*). Moreover, they require stretchable materials for both electrodes and dielectric layers, which restricts material selection and design freedom.

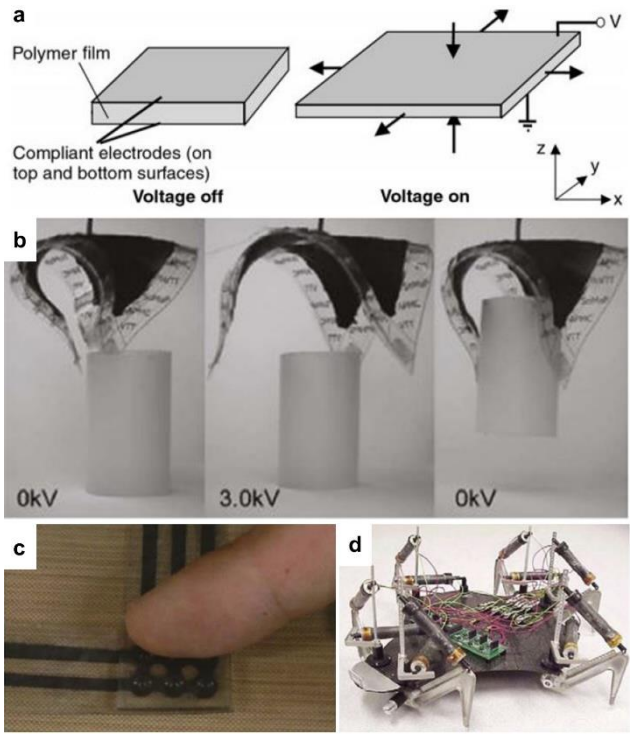

Figure 1.4: Dielectric elastomer actuators (DEAs). a) The basic operating principle of a DEA (*25*). b) A DEA coupled to a minimum energy structure was used as a soft end-effector (*38*). c) An array of DEAs acts as an active braille display (*39*). d) An untethered crawling robot based on rolled DEAs (*36*).

Recently developed thermally activated artificial muscle actuators made from inexpensive coiled polymer fibers (Figure 1.5) can provide large actuation forces and work density (*40*, *41*). Additionally, these twisted fibers can be made to achieve strain-programable linear and torsional deformations (*42*, *43*). Other thermally controlled soft actuators use a phase-transition of a fluid contained within an elastomer shell to generate a deformation (*44–46*). However, these examples of thermally controlled soft actuators suffer drawbacks in response speed since they rely on cooling the system to return to the initial state. Likewise, these devices suffer from low electromechanical efficiency (1.32%) when utilizing Joule-heating as the input energy source (*40*). Therefore, their applications favor those which offer a natural heating and cooling stimulus (such as gradients in ambient temperature from day to night, etc.).

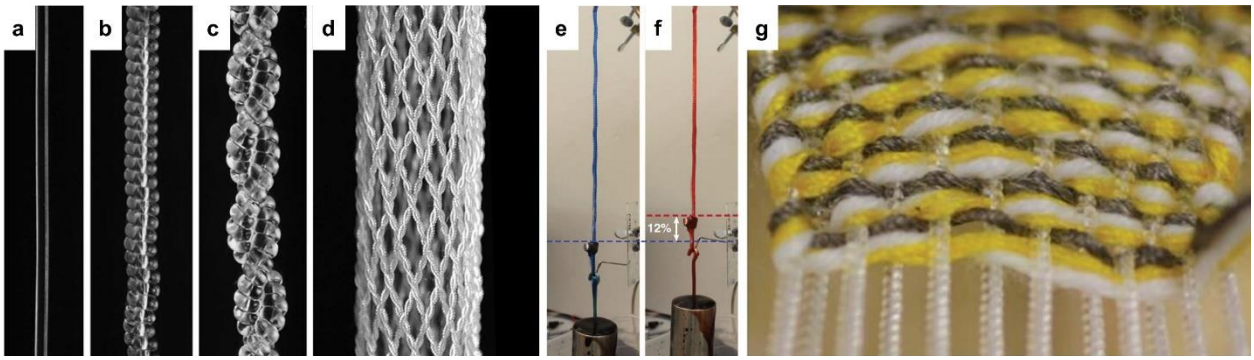

Figure 1.5: Twisted and coiled fibers as artificial muscles. a) An image of a non-twisted fiber having a diameter of 300 µm. b) The fiber shown in a) after twisting until it coiled. c) Two of the coils seen in b) are twisted together. d) A braid from 32 coils seen in c). e) A coiled fiber lengthens when cooled and f) contracts when heated. g) The coiled actuators can be woven into cloth. (*40*)

1.3 Scope of this dissertation

The work presented in this dissertation is focused on the invention and exploration of a new type of soft actuator called a Hydraulically Amplified Self-healing ELectrostatic (HASEL) actuator. The next chapter will highlight the fundamental operating principles of HASEL actuators and develop fabrication methods to create initial prototypes from two distinct sets of materials, silicone elastomers and thin film thermoplastics. Additionally, a soft robotic gripper made from HASEL actuators is presented and demonstrated to grasp a raspberry and raw egg.

Chapter 3 introduces a technique to rapidly design and prototype HASEL actuators by heat sealing thermoplastics in nearly arbitrary 2D geometries. The electromechanical performance of the actuators constructed from this technique is evaluated and shown to exceed that of previously described devices. Furthermore, a modular approach to creating actuators and their accompanying driving electronics is detailed. The driving electronics are battery-powered and used to power an untethered HASEL-based soft robotic continuum actuator capable of three-dimensional motion.

In the fourth chapter, a new design for a contracting HASEL actuator is developed and shown to achieve well-rounded muscle mimetic actuation, including contractile strains up to 23%.

The quasi-static load-strain behavior of this actuator is discussed from both an experimental and theoretical perspective. The fabrication techniques discussed in Chapter 3 are implemented to iterate the design of this new actuator, resulting in an improvement to the no-load actuation strain. Furthermore, the actuator is implemented as a soft tubular pump, resembling the biomimetic pumping motion of the primordial heart of an ascidian.

Chapter 5 showcases a state-of-the-art 10-channel pocket-sized high voltage power supply to drive HASEL actuators. This power supply is battery powered and nearly as compact as a smartphone, while capable of independently addressing 10 groups of HASEL actuators to voltages up to 10 kV. Importantly, independent control of these 10 channels is achieved through a charge-controlled driving scheme that requires only one high voltage amplifier. The capabilities of this power supply are highlighted through the independent control of actuators in a 2x5 array that simulates an active surface. Furthermore, we use the power supply to generate undulatory actuation signals that allow peristaltic locomotion of a soft robotic inchworm. The chapter ends with a theoretical discussion on the electrical safety of high voltage electrostatic actuators in the context of Underwriter Laboratories (UL) safety standards.

In Chapter 6, we discuss the development of Area-of-Effect Softbots (AoES) for the exploration and mining of asteroids in space. Electrostatic actuation and anchoring mechanisms for these robots are proposed and developed. Robot designs utilize spider inspired HASEL architectures that combine soft and rigid materials to enable fast, lightweight, and powerful articulations of the limbs. Furthermore, an electroadhesive anchoring systems is proposed for the robot to successfully traverse the peculiar and relatively unknown surface of an asteroid. Electroadhesive pads are designed, built, and their ability to resist shear force is tested while adhering to a plethora of different substrate materials and textures.

Finally, Chapter 7 reflects on the developments presented in this dissertation and offers guidelines for future work.

2 Hydraulically Amplified Self-healing ELectrostatic (HASEL) actuators

2.1 State of the art

For soft robotics to proliferate, there is a persistent need for an artificial muscle technology that replicates the versatility, performance, and reliability of biological muscle (*8*, *12*). As discussed in Chapter 1, the challenges surrounding existing soft actuators impede soft robots from achieving the multifunctionality seen in biological system.

2.2 Contributions to expand the state of the art

In Acome et al. (*47*), we described a class of soft actuators, termed Hydraulically Amplified Self-healing ELectrostatic (HASEL) actuators, which harness a mechanism that couples electrostatic and hydraulic forces to achieve a variety of actuation modes. This actuation mechanism combines the benefits of both soft fluidic and dielectric elastomer actuators, while simultaneously mitigating the drawbacks of each. In contrast to soft fluidic actuators where inefficiencies and losses arise from fluid transport through systems of tubes, HASEL actuators generate hydraulic pressure locally via electrostatic forces acting on liquid dielectrics distributed throughout a soft structure. On the other hand, HASELs possess a wide design freedom in terms of materials and architectures, which is similar to that of soft fluidic actuators. In contrast to dielectric elastomer actuators, which fail prematurely due to dielectric breakdown making them difficult to scale-up, HASEL actuators possess the ability to self-heal from dielectric breakdown due to the use of a liquid dielectric. In this first work, we introduced prototypical designs of HASEL actuators and characterized their strength, speed, and electromechanical efficiency.

Importantly, these prototypes used widely available materials and common fabrication techniques. To highlight their potential as robotic hardware, a HASEL-based soft gripper was created that could grasp delicate objects like a raspberry and an egg.

2.2.1 Basic operating principle of HASEL actuators

The basic operating principle of HASEL is shown in Figure 2.1. An elastomeric shell partially covered by a pair of opposing electrodes is filled with a liquid dielectric. Upon application of voltage, an electric field is generated between the opposing electrodes and an attractive electrostatic force develops. This electrostatic stress (called Maxwell stress) increases the pressure within the liquid dielectric driving shape-change of the soft elastomeric shell. The Maxwell stress (*48*) can be expressed as,

$$\sigma = \frac{1}{2}\varepsilon\varepsilon_0 E^2 \tag{2.1}$$

where σ is the Maxwell stress in the principal direction of the applied field, ε_0 is permittivity of free space (8.854 x 10^{-12} F m^{-1}), ε is the relative permittivity of the dielectric material, and E is the electric field acting through the composite of solid and liquid dielectric layers.

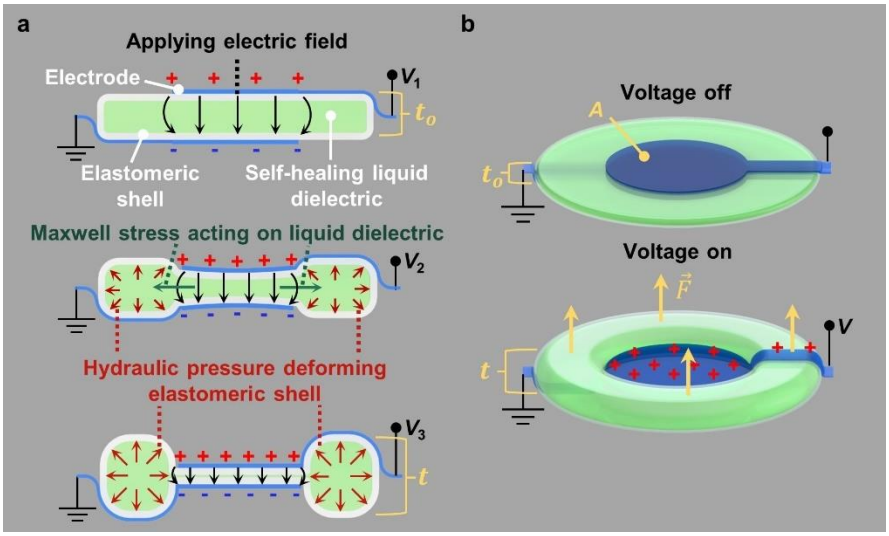

Figure 2.1: Basic operating principle of HASEL actuators. a) A cross-section of one specific design of a HASEL actuator. b) An isometric view of the actuator. (*47*)

2.2.2 Fabrication of donut HASEL actuators

The HASEL actuator seen in Figure 2.1 was termed a donut HASEL actuator since the actuated state resembles a toroidal or donut shape (Figure 2.1b). A key benefit of the basic structure of these devices is that they can be fabricated from commonly used materials in the field of soft robotics, including silicone-based elastomers and ionically conductive hydrogels. In this initial work, we built donut HASEL actuators using polydimethylsiloxane (PDMS; Sylgard 184, Dow Corning) as the elastomeric shell, a vegetable-based transformer oil (Envirotemp FR3, Cargill) as the liquid dielectric, and ionically conductive polyacrylamide (PAM) hydrogels as the electrodes. The fabrication procedure can be seen in Figure 2.2. PDMS was cast into 0.3 mm thick, 6 cm diameter circular sheets (Figure 2.2, step 1) and cured in an oven at 75 °C for 30 minutes. An acrylic ring with a 6 cm outer diameter and 5 cm inner diameter was placed on top of each PDMS sheet such that the ring and sheet were concentric. Uncured PDMS was then applied on the area of PDMS sheet which overlapped with the acrylic ring (Figure 2.2, step 2). Two PDMS sheets were aligned concentrically and clamped between the acrylic rings, with the uncured PDMS between the sheets to act as a bonding agent (Figure 2.2, step 2). A syringe with a needle was inserted between the clamped PDMS sheets, and air was used to inflate the shell to keep the middle from bonding together. The inflated shell was cured in an oven at 75 °C for 30 minutes (Figure 2.2, step 3). Once cured, the clamps and acrylic rings were removed from the shell. An Ecoflex 00-30 patch was applied to a region of the PDMS shell to act as a fill point, which self-sealed after being punctured with a needle (Figure 2.2, step 4). A syringe with a needle was inserted through the Ecoflex 00-30 patch, and then used to replace the air in the shell with 4 mL of liquid dielectric (EnviroTemp FR3) (Figure 2.2, step 5). After the PDMS shell was filled with liquid dielectric, ionic conductors for the electrodes were synthesized from polyacrylamide (PAM) hydrogels

containing lithium chloride (LiCl) (*49*). PAM-LiCl hydrogels consisted of aqueous lithium chloride (LiCl; The Science Company, NC-4851) as the ionic conductor, acrylamide (AAm; Sigma, A8887) as the monomer, N,N-methylenebisacrylamide (MBAA; Sigma, 146072) as the crosslinker, ammonium persulfate (AP; Sigma, 248614) as the photo-initiator, and N,N,N',N'-tetramethylethylenediamine (TEMED; Sigma, T9281) as the crosslinking accelerator. First, LiCl (8 M) was dissolved in deionized water and the solution was allowed to cool to room temperature. Then, AAm (2.2 M) was dissolved in the 8 M LiCl solution along with MBAA (0.06 wt% of AAm) and AP (0.17 wt% of AAm). The solution was mixed on a stir plate for 5 minutes then degassed for 10 minutes. To initiate polymerization, TEMED (0.05 wt% of AAm) was added to the solution immediately before casting the hydrogels. The PAM solution was cast onto a 25.4-μm-thick Kapton film (Dupont, 5-50-KHN-1), which acted as a protective backing and made the hydrogels easier to handle. The hydrogels were cured under 365-nm UV light (3UV-38, UVP) for 1 h and then laser cut to the desired circular shape and dimension using a laser cutter (Legend 36 EXT, Epilog). An electrode was placed on either side of the shell concentric to the outer diameter of the shell, with the Kapton film facing outward (Figure 2.2, step 6) and with the leads oriented 180° from each other. The electrodes were glued to the PDMS shell with cyanoacrylate glue (406, Loctite).

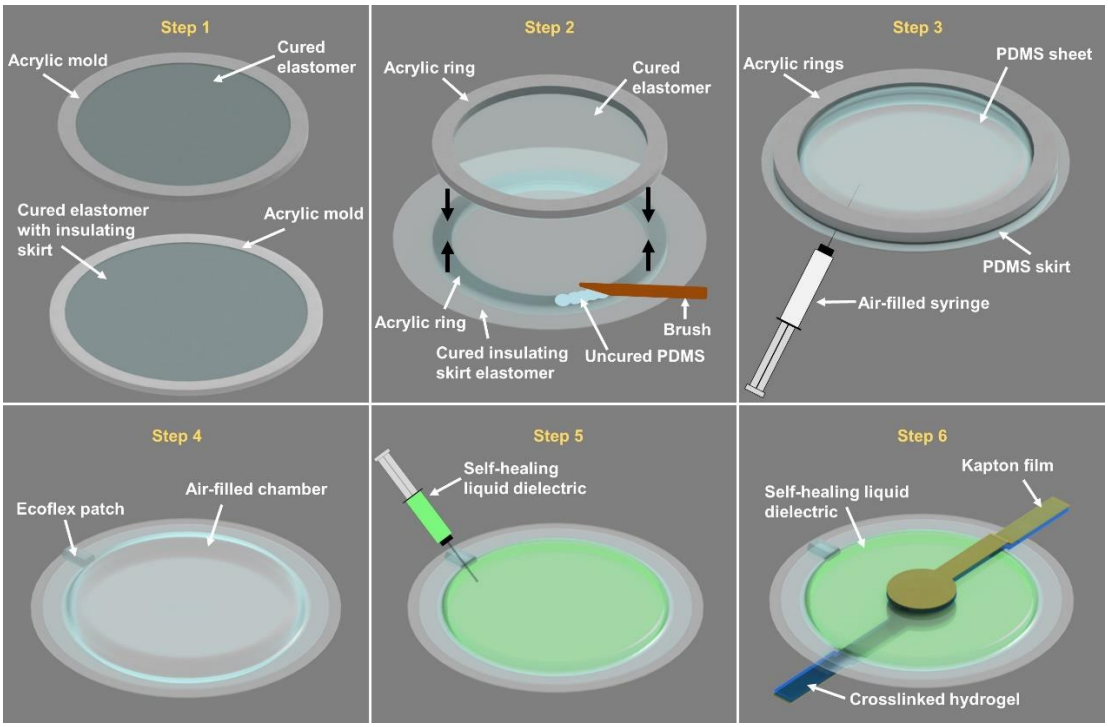

Figure 2.2: Fabrication steps for a donut HASEL actuator. (*47*)

2.2.3 Harnessing principles of hydraulic scaling

Since HASEL actuators are electrohydraulic structures, they follow Pascal's law of hydraulics, which states that the pressure of a fluid within a closed container is the same everywhere (a principle commonly used in everyday life, such a hydraulic car jack). Figure 2.3 details the principle of hydraulic scaling for donut HASEL actuators. Consider two donut HASEL actuators with identical architectures except for the diameter of their respective electrodes. One actuator has a smaller electrode diameter relative to the other. For a given activation voltage the actuator with the smaller electrode displaces less fluid and therefore achieves a smaller displacement (t_{small}), relative to the actuator with the larger electrodes (t_{large}).

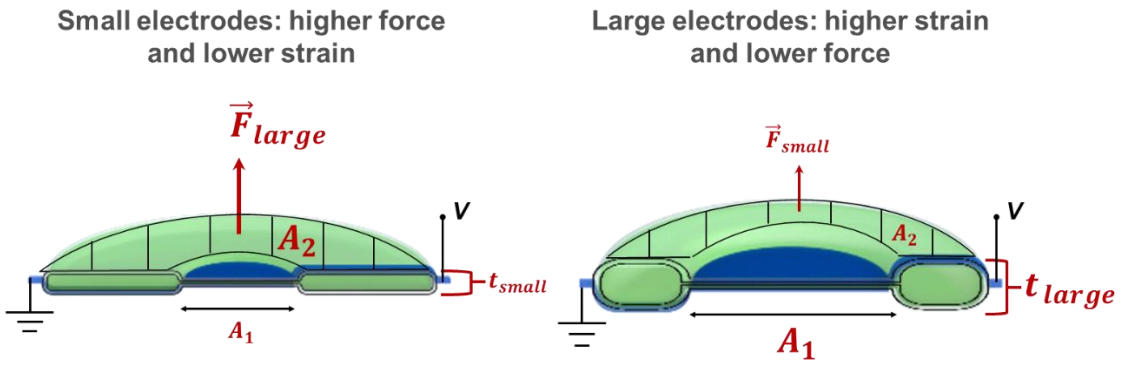

Figure 2.3: Pascal's hydraulic principle in HASEL actuators.

However, the actuator with the smaller electrode has a larger area that acts on the applied load as compared to the actuator with the larger electrode, and therefore yields a larger force (since the hydraulic pressure within both actuators is the same for a given activation voltage). Figure 2.4 shows the experimental results of the above thought experiment.

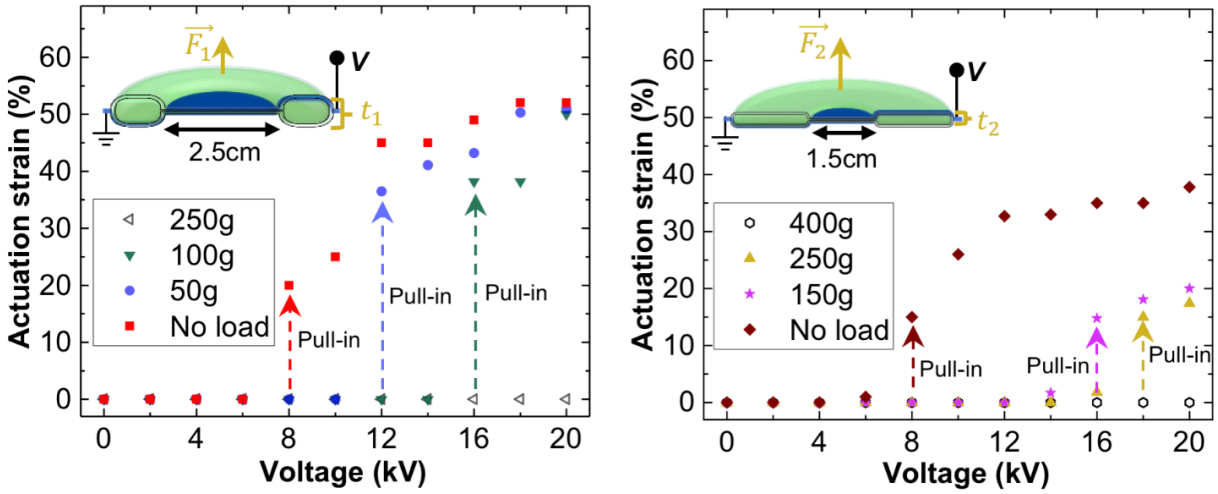

Figure 2.4: Experimental verification of Pascal's law for HASEL actuators. The actuator with a larger electrode achieves more displacement but less force than an identical actuator with a smaller electrode. Both actuators exhibit a pull-in instability, which occurs when the electrostatic force between the electrodes overcomes the mechanical restoring force of the load, and therefore cause the electrodes to abruptly pull together resulting in a dramatic change in actuation strain. (*47*)

2.2.4 Self-healing from dielectric breakdown

The use of a liquid dielectric also allows HASEL actuators to recover from dielectric breakdown. Figure 2.5 displays this principle and the experimental results. When a dielectric breakdown event occurs through the composite dielectric structure, the liquid dielectric can reflow and restore insulating conditions. For successful recovery from a breakdown event, it is imperative that the damage to the solid dielectric is not substantial as to allow the liquid dielectric to leak from the shell. Figure 2.5 demonstrates the ability of a donut HASEL actuator to recover from 50 consecutive dielectric breakdown events.

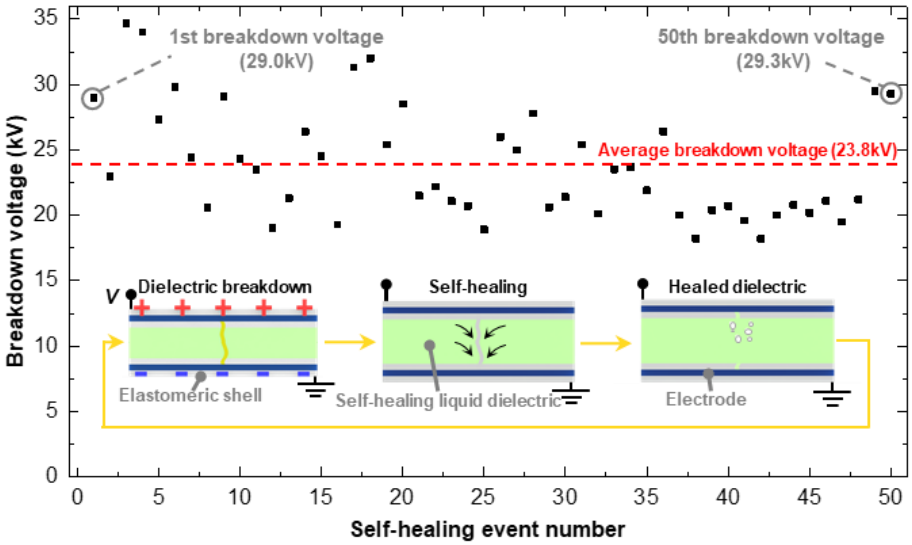

Figure 2.5: Recovery from dielectric breakdown. (*47*)

2.2.5 Lifetime and electromechanical efficiency of donut HASEL actuators

To truly realize soft actuators of the next generation of machines, it is vital that these actuators provide long lasting and efficient performance. We analyzed the cycle life of a donut HASEL actuator that was driven with an 18 kV, 5 Hz actuation signal that reversed the polarity of the applied voltage every cycle. Under an applied load of 150 g, the actuation strain of the device

was ~15% and did not noticeably diminish over the course of 1.08 million cycles, Figure 2.6. The lifetime test was stopped due to time constraints and not due to failure of the actuator.

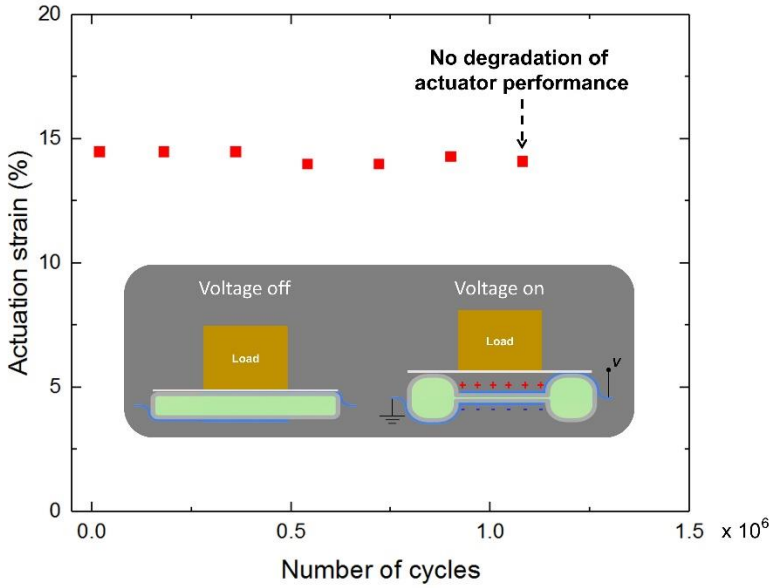

Figure 2.6: Cycle life of a donut HASEL actuator. (*47*)

Additionally, we measured the electromechanical efficiency of a donut HASEL actuator, which was based on the mechanical work done by the actuator (output energy) and the electrical energy expended (input energy) during one complete cycle of actuation. In order for the actuator to perform work, a four-step actuation cycle, Figure 2.7a, was conducted:

1 → **2**: The actuator started with a constant load of 100 g and at zero voltage. A linear voltage ramp was applied to charge the actuator with electrical energy. As voltage increased, the electrodes pulled together and caused the actuator to increase in thickness, thereby lifting the load.

2 → **3**: At the maximum values for voltage and displacement, the load was removed from the actuator.

3 → **4**: The actuator was discharged by linearly decreasing voltage. The donut HASEL actuator returned to the initial thickness at zero voltage. Since the load had been removed, no mechanical work was performed during this step.

4 → **1**: The load was placed onto the actuator with voltage off. Neither electrical nor mechanical work was performed in this step.

We used the experimental setup seen in Figure 2.7b to measure the electrical energy consumed and the mechanical work performed by the actuator during the cycle. A custom LabVIEW program (version 15.0.1f2, 64-bit) and a data acquisition board (DAQ) (Model USB6212, National Instruments) were used to provide a control signal to the high voltage amplifier (Model 50/12, Trek). HASEL actuators are electrically equivalent to a variable capacitor, C, with a resistor in series, $R_{\text{electrode}}$, to represent resistance of the electrodes. Leakage current through the HASEL actuator is represented by a parallel resistor, R_{leakage}. Some electrical energy will be lost to electrode resistance and leakage current. The efficiency of HASEL actuators could be increased by reducing the amount of leakage current during actuation.

Electrical energy was determined by controlling the voltage, $V(t)$, applied to the actuator and measuring the current, $I(t)$, flowing in and out of the actuator. Voltage applied to the actuator, $V(t)$, was prescribed by the custom LabVIEW program and generated via a HV amplifier (Trek, Model 50/12). Current, $I(t)$, was calculated using Ohm's law with measurement of voltage, $V_m(t)$, across a precision resistor, $R_m = 2\ k\Omega$. The precision resistor was placed on the ground side of the circuit and connected in parallel to a transient-voltage-suppression diode (Model 1.5KE56CA-TP, Micro Commercial Components) to protect the DAQ equipment in case dielectric breakdown occurred. Charge, $Q(t)$, was calculated by taking the cumulative integral of current, $I(t)$, over time,

t. Finally, electrical energy was calculated as the area enclosed by the path of the cycle within the voltage-charge work-conjugate plane (Figure 2.7e).

Mechanical energy was determined by measuring the displacement of the load as a function of time. A high-speed camera (Model Phantom v710, Vision Research) was used to record video of the actuator from state 1 to 2 of the cycle described in Figure 2.7a. Video analysis software (Tracker) was used to determine vertical displacement of the load, y(t). Tracker was also used to determine the force accelerating the load during actuation. Mechanical energy was calculated as the area enclosed by the path of the cycle within the force-displacement work-conjugate plane (Figure 2.7h).

The applied voltage signal, V(t), was a symmetric triangle with 1.5 s total period (0.75s charging and 0.75 s discharging) with an amplitude of 21 kV (Figure 2.7c). The electrodes of the actuator were covered with a thin layer of Ecoflex 00-30 to reduce the loss of charges to the surroundings. The time variation of parameters for electrical energy (Figure 2.7c-e) are plotted beside their corresponding mechanical parameters (Figure 2.7f-h). A pull-in transition occurs around 0.5 s, which is indicated by a sudden change in current and charge (Figure 2.7d) as well as a sudden change in displacement (Figure 2.7g). The area enclosed by the path of the actuator in the voltage-charge work-conjugate plane (Figure 2.7e) represents the electrical energy, W_{el}, which was 2.88 mJ. Likewise, the area enclosed by the path of the actuator in the force-displacement work-conjugate plane (Figure 2.7h) represents the mechanical energy of the cycle, W_{mech}, which was 0.59 mJ. The corresponding efficiency, W_{mech}/W_{el}, was 21%.

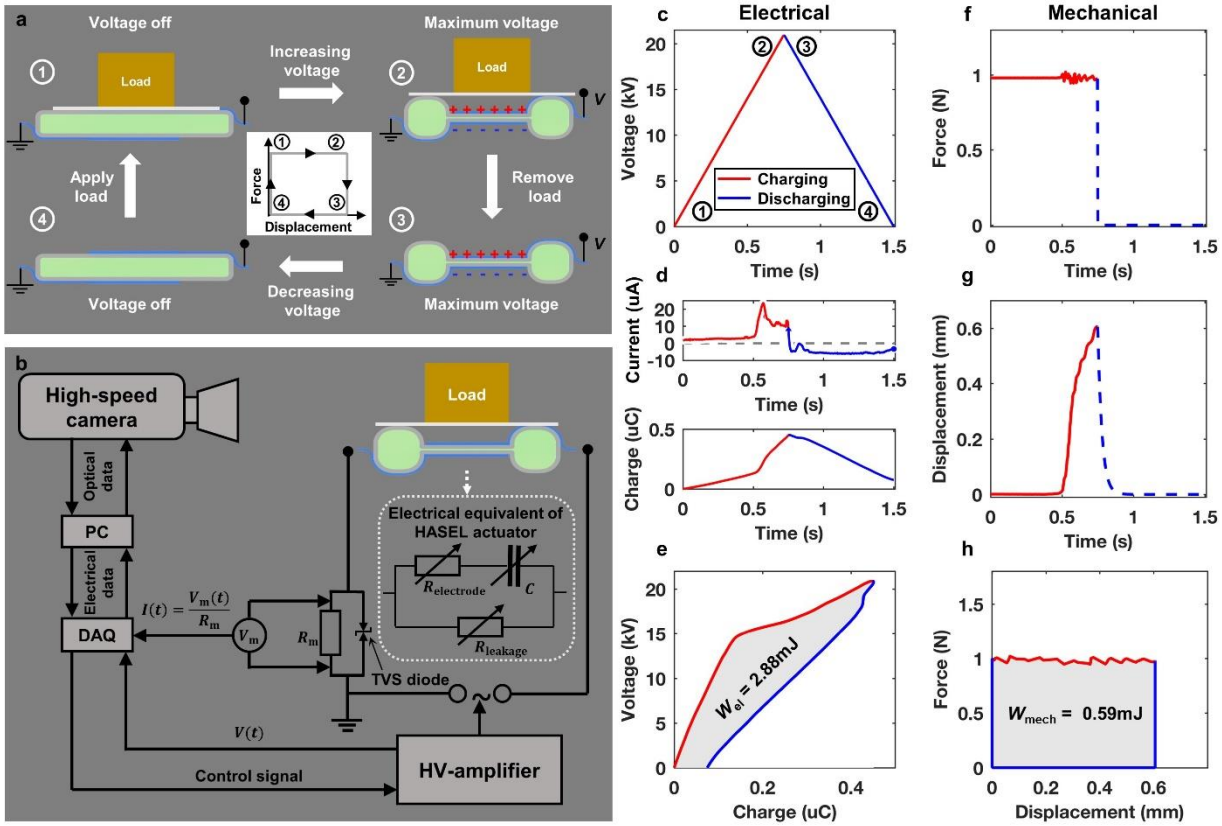

Figure 2.7: Measurement of the full-cycle electromechanical efficiency of a donut HASEL actuator. (*47*)

2.2.6 A soft gripper based on HASEL actuators

Donut HASEL actuators can be stacked to increase the stroke of the linear expansion during activation, Figure 2.8. The actuators were electrically connected in parallel and were stacked such that adjacent electrodes of neighboring actuators were connected to the same lead from the power supply. This design ensured that adjacent electrodes were at the same potential to avoid a short circuit between neighboring actuators.

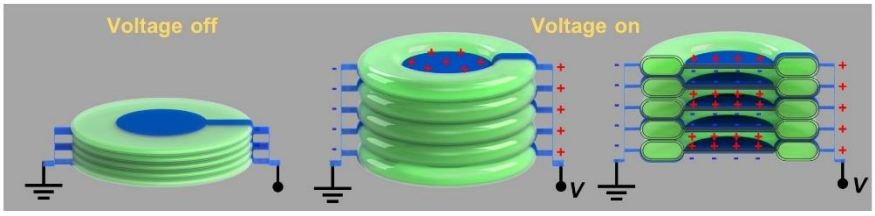

Figure 2.8: Stacked donut HASEL actuators to boost actuation stroke. (*47*)

Moving towards practical soft robotic devices, we created a soft gripper from two modified stacks of donut HASEL actuators. Actuators within the stacks were constrained on one side to produce a tilting motion (Figure 2.9a). Donut HASEL actuators were fabricated as described in the Section 2.2.2 with the exception that the PDMS sheets had a diameter of 8 cm. The 8-cm diameter PDMS sheets resulted in a 1.5 cm wide skirt surrounding a 5 cm diameter shell. Ten donut HASEL actuators were constructed in this way and the skirt was cut away from half of the circumference of each actuator. Stacks of five donut HASEL actuators were constructed by bonding the skirt of each actuator together using uncured PDMS. The stacks were mounted to opposing sides of an acrylic frame (Figure 2.9b) using double sided tape with the ground electrodes facing inwards. Upon application of a DC voltage, the actuators tilted towards each other due to the added constraint from bonding the donut HASEL actuators together on one side. This deformation was used to grasped delicate objects such as a raspberry (Figure 2.9c-e) and a raw egg (Figure 2.9f).

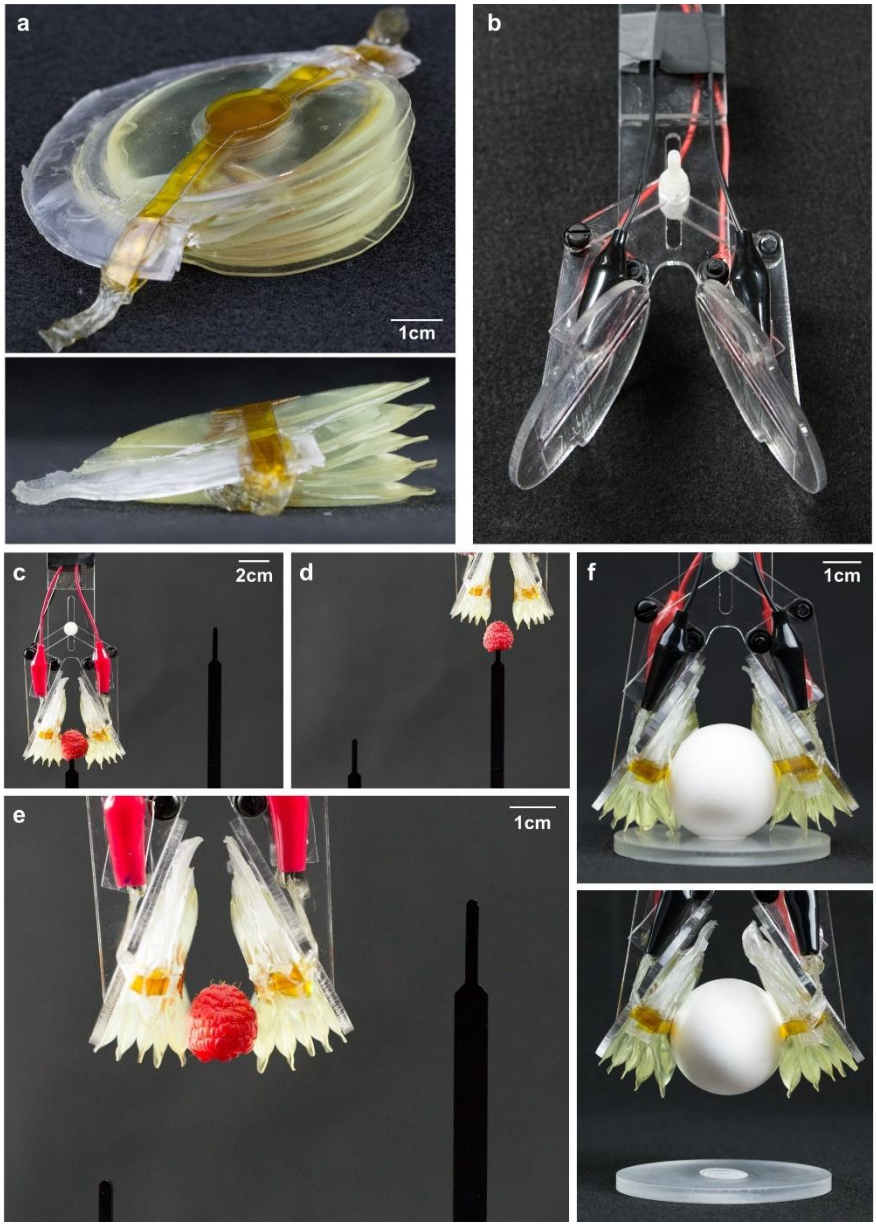

Figure 2.9: A soft gripper made from stacks of donut HASEL actuators. (a) Isometric view and side view of the donut HASEL stacks used for the soft gripper. (b) Side view of the acrylic component of the gripper used to hold the stacks in the proper orientation. (c) to (e) The gripper was capable of grasping and transporting a raspberry and (f) a raw egg. (*47*)

2.2.7 Peano-HASEL actuators with muscle-like linear contraction

The work presented by Acome et al. displayed a new electrohydraulic actuation mechanism, but only scratched the surface of the design freedom of HASEL actuators. The materials used in this first work focused primarily on stretchable materials; silicone elastomers

where used as the solid dielectric and ionically conductive hydrogels were used as the electrodes. However, it was evident that a plethora of flexible, yet inextensible materials could be utilized, opening a design freedom yet to be seen for soft electrostatic actuators.

In Kellaris et al. (*50*), we described a subclass of HASEL actuators, called Peano-HASEL actuators that featured muscle-mimetic linear contraction upon application of voltage. The basic structure and operating principle of Peano-HASEL can be seen in Figure 2.10. Opposing electrodes cover a portion of a rectangular-shaped flexible, yet inextensible polymer shell that is filled with a liquid dielectric. The electrodes are placed on either side of a tapered edge of the shell. When voltage is applied across the electrodes, the resulting electric field is concentrated at the tapered edge, and therefore, the electric field is greatest at this location. This field concentration causes the electrode 'zip' together at the tapered edge. As voltage is increased, the electrostatic force between the electrodes is increased causing the electrodes to zip progressively. The zipping process displaces the fluid to the region of the pouch not covered with electrodes causing this region to transition into a more cylindrical shape. Because the polymer shell can only flex, not stretch, the resulting shape change leads to an overall linear contraction of the actuator.

Peano-HASEL actuators achieved controllable linear contraction up to 10%, strain rates as high as 900% s^{-1}, a specific power exceeding 120 W kg^{-1}, and the ability to lift more than 200 times their own weight. This linear contraction is achieved without the need for a prestretched film, rigid frame, or complicated stacking method (*25*, *29*). Furthermore, these actuators were shown to sense their deformation through capacitive self-sensing. Importantly, these devices were made from a facile fabrication procedure using inexpensive thermoplastic polymers.

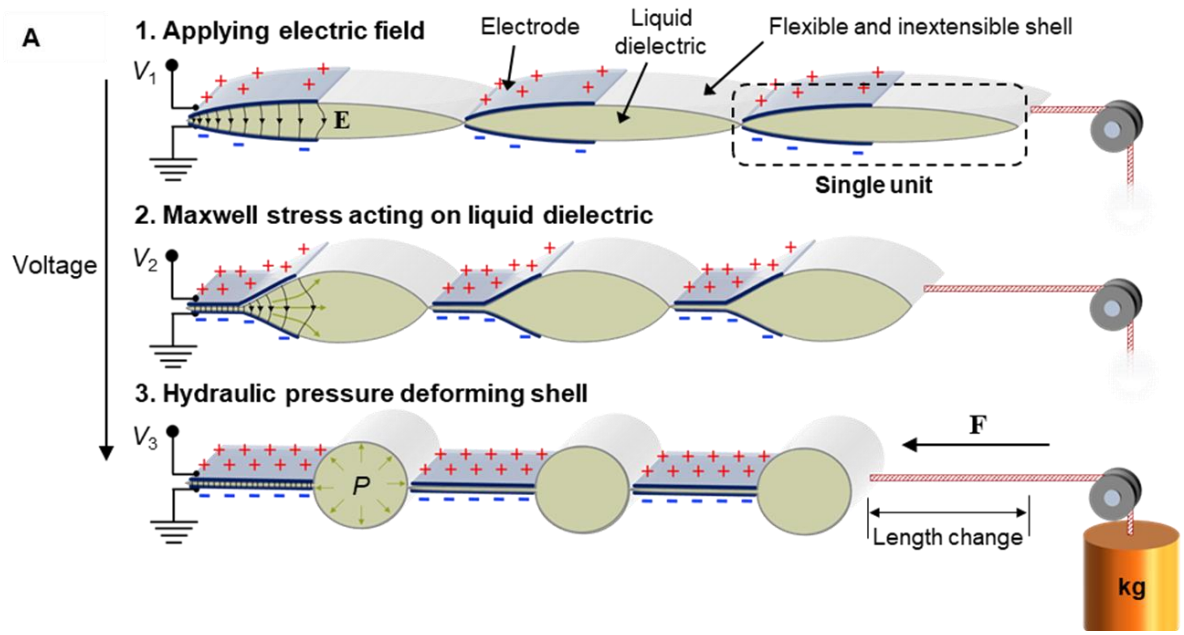

Figure 2.10: Structure and operating principle of Peano-HASEL actuators. (*50*)

2.2.8 An industrial amenable fabrication technique

A key advantage of Peano-HASEL actuators is that they can be fabricated from inexpensive materials (~10 cents per actuator) that are suitable for industrial manufacturing processes. Figure 2.11 shows an example fabrication process of a Peano-HASEL. This process utilizes metalized biaxially oriented polypropylene (BOPP) as the dielectric shell, which is heat sealed using a heat-sealing press. BOPP was chosen for its favorable dielectric properties such as high dielectric strength (~700 kV mm^{-1}). The metalized layer of the BOPP can be etched into the shape of the electrodes enabling extremely low resistance electrical conductors, thereby limiting resistive losses during high frequency operation.

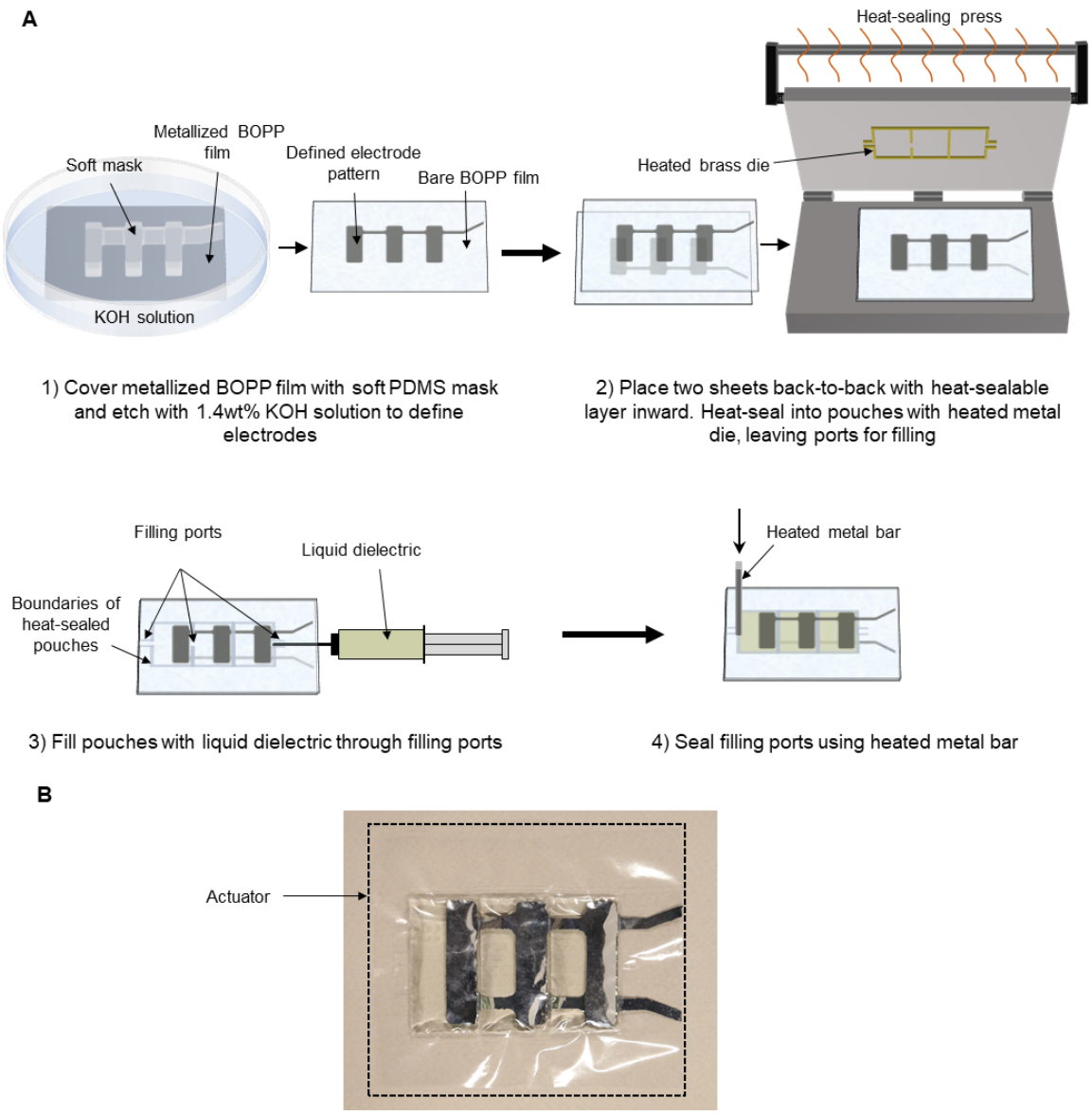

Figure 2.11: An example fabrication process for Peano-HASEL actuators. (*50*)

2.3 Outlook

HASEL actuators rely on all-soft-matter hydraulic architectures and local generation of hydraulic pressure via electrostatic forces acting on self-healing liquid dielectrics—a recipe that combines the strengths of soft fluidic and electrostatic actuators while addressing important problems of each. The use of hydraulic principles in HASEL actuators results in the capability to scale actuation force and strain—a feature also used in other device classes such as microhydraulic

systems, which are constructed from thin films and rigid substrates (*51*), and in hydrostatically coupled DE actuators (*52*), where electric fields are applied across elastomeric layers that do not self-heal after dielectric breakdown. The work detailed above demonstrated versatile, robust, muscle-like performance of HASEL actuators made from inexpensive, widely available materials and using basic fabrication techniques. With a plethora of geometries, materials, and advanced fabrication strategies still unexplored, HASEL actuators offer a new platform for research and development of muscle-mimetic actuators with wide-ranging applications.

3 An easy-to-implement toolkit to create versatile and high performance HASEL actuators for untethered soft robots

3.1 State of the art

The groundbreaking research presented by Acome et al. and Kellaris et al. laid the framework to create versatile and high-performance artificial muscles. However, the work was not without limitations. Specifically, the fabrication processes detailed by each paper required molds to cast elastomers or a metal die to act as a heat-sealing stamp, both of which were not easily adjusted to prototype the design of the actuator or create more complicated features. Moreover, achieving muscle-mimetic actuation required voltages on the order of 15-20 kV, which severely restricted the options for commercially available miniature high-voltage amplifiers and the associated driving electronics.

3.2 Contributions to expand the state-of-the-art

As the field of soft robotics continues to grow, open source initiatives such as the Soft Robotics Toolkit have given a wide audience of researchers, hobbyists, and even entrepreneurs an outlet to explore and create soft robotic technologies. Inspired by this ease-of-accessibility, we aimed to create a comprehensive framework for a broad audience to delve into and ultimately improve HASEL actuators (*53*).

This chapter introduces a method to rapidly prototype various designs of HASEL actuators with muscle-like performance that achieve all three basic modes of actuation (expansion, contraction, and rotation) and incorporate electrostatic zipping mechanisms to reduce driving voltages. This method requires only inexpensive off-the-shelf fabrication tools and commodity

materials, enabling access to HASEL technology for a wide audience. Remarkably, the actuators created from this easy-to-implement method achieved linear strains exceeding 100%, a specific power greater than 150 W kg^{-1}, and ~20% strain at frequencies above 100 Hz. This combination of large strain, extreme speed, and high specific power yielded soft actuators that could jump without power-amplifying mechanisms. Additionally, a modular design for robotic devices based on HASEL actuators was introduced, for which we developed portable driving electronics using off-the-shelf components. Inspired by the versatility of elephant trunks, the above capabilities were combined to create an untethered continuum robot for grasping and manipulating delicate objects, highlighting the wide potential of the introduced methods for soft robots with increasing sophistication.

3.2.1 A versatile fabrication technique

To prototype design for the dielectric shell of HASEL actuators, we used a three-axis CNC machine to heat seal thin layers of thermoplastics into pouches of various shapes and sizes (*54–56*). In this work, we repurposed an inexpensive 3D printer (RepRap3D, MagicD A2) into a three-axis CNC heat sealing machine (Figure 3.1a). Designs for the dielectric shell were initially drawn using computer-aided design (CAD) software (SolidWorks 2017–2018), exported as a 2D drawing in a .dxf file, and then converted to G-code using an open source software called "dxf2gcode." The G-code defined the path of the extruder tip of the CNC machine, which was heated to 195 °C and moved at a constant speed of 800 mm min^{-1}. A 0.32-cm-thick neoprene rubber sheet was placed on the base of the heat-sealing device to help evenly distributed the force of the heat-sealing tip. Two sheets of biaxially oriented polypropylene (BOPP) were sandwiched between two sheets of Kapton (TapeCase 1 mil, Dupont) and placed on the neoprene-covered base plate (Figure 3.1a).

Kapton was used to evenly distribute the heat during the sealing process and to avoid melting through the BOPP. Figure 3.1b shows two different designs for the shell (a quadrant donut and a contracting HASEL) after they have been heat-sealed. All heat seal designs included a small opening (2-mm-wide) to act as a fill port. While this work focused primarily on BOPP, the heat-sealing method presented enabled a wide design space for alternative thermoplastics as the dielectric shell, such as thermoplastic polyurethane (TPU) and polyethylene terephthalate (PET).

A biodegradable vegetable-based transformer oil (Envirotemp FR3, Cargill) was used as the liquid dielectric. FR3 was chosen as the liquid dielectric because of its favorable dielectric properties, nontoxicity, and low viscosity. Similar to the dielectric shell, many other types of liquid dielectrics (such as silicone or mineral oil) with specific desired properties are compatible with this fabrication technique. A syringe with a needle was used to fill the chamber(s) of the heat-sealed dielectric shell with the liquid dielectric through the fill port, Figure 3.1c. Air bubbles from the filling process were carefully removed. Then, a Kapton sheet was placed on top of the filled shell, and the fill port was sealed with a soldering iron heated to 195 °C, Figure 3.1d. Once sealed, the excess BOPP was cut away with scissors, leaving a 1-cm-wide ‘skirt’ around the electrode region to prevent electrical arching through the air.

Electrodes were constructed from both ionically conductive LiCl-PAM hydrogels (as described in Section 2.2.2) as well as off-the-shelf, carbon-based conductive paint (Figure 3.1e).

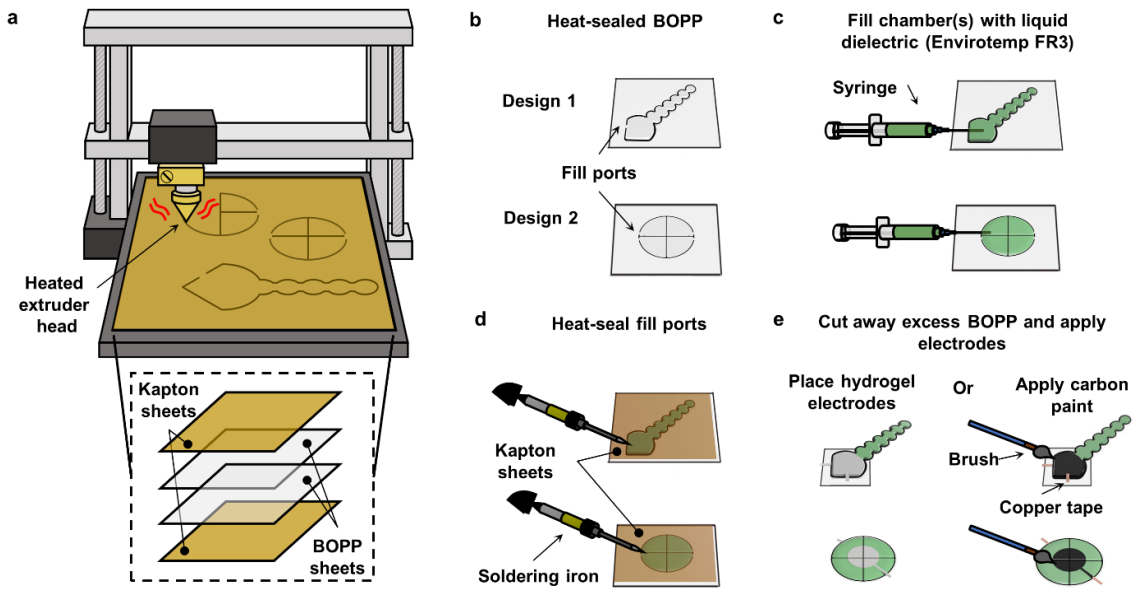

Figure 3.1: Fabrication process to rapidly prototype various types of HASEL actuators. a) An illustration of the three-axis CNC heat sealing machine used to bond thermoplastics for the dielectric shell. b) Two exemplary patterns of heat seals. Small gaps in the seal were incorporated to c) fill the shell with liquid dielectric using a needle and syringe. d) Once the shell was filled with liquid dielectric, the fill ports were sealed with a soldering iron. e) The excess BOPP was cut away and electrodes were applied to either side of the actuator. (*53*)

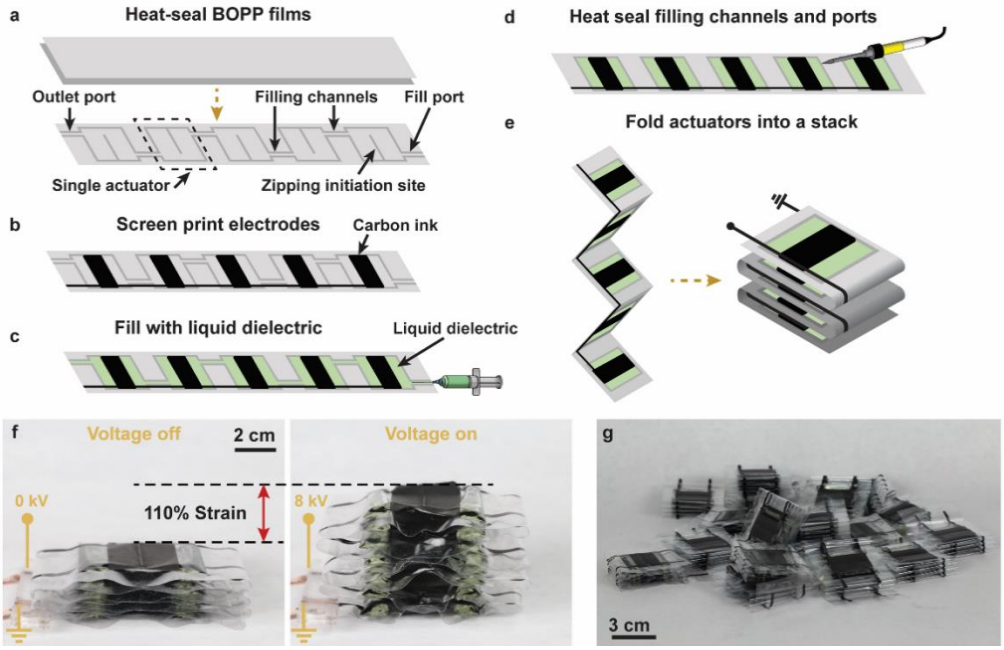

Figure 3.2: Fabrication technique to create modular units of stacked HASEL actuators through a folding process. (*53*)

Figure 3.2 details a method to rapidly manufacture modular units of HASEL actuators through a folding technique. In this method, the dielectric shell for each actuator in the unit is heat sealed in a single step using the CNC machine, and then the electrodes for each actuator are screen-printed onto the dielectric shell as one continuous strip. Next, all the actuators in the modular unit were filled with liquid dielectric simultaneously through one fill port, and the liquid is evenly distributed throughout all the actuators. Then, the filling channels between actuators are heat sealed using a soldering iron to create independent chambers of liquid dielectric. Finally, stacking the actuators into a modular unit is accomplished by folding the actuators in a zigzag pattern; similar techniques have been employed to fold stacks of DEAs (*57*). The mechanical connections between adjacent actuators are provided by double-sided tape (3M, 924 Transfer Tape). The number of actuators in a single stack is limited by the size of the heat-sealing equipment and screen for depositing the electrodes.

3.2.2 Bioinspired design: curling and twisting HASEL actuators

The easy-to-implement fabrication process can be utilized to create bioinspired actuators that can contract, curl, or twist. Figure 3.3 details the basic operating principles of these actuators. The contracting actuators feature electrodes that cover a reservoir of liquid dielectric that leads into a corrugated pathway, Figure 3.3a. Upon activation the electrodes zip together forcing the liquid dielectric into the corrugated pathway. Since the dielectric shell is inextensible, the increased pressure within the corrugations causes the radius of curvature of each corrugation to decrease, resulting in an overall contraction of the hydraulic structure, Figure 3.3b. Strain limiting layers can be used to force directionality of the actuators when activated. Specifically, if a strain limiting layer is added to one side of the contracting actuators seen in Figure 3.3c, the resulting actuation

results in a bending or curling mode. The rapid actuation of these curling HASELs resembled the high-speed strike of a scorpion tail, Figure 3.3d. Figure 3.4 shows that the peak velocity of the tip of the curling actuator is 1.26 m s^{-1}, which is nearly identical to the maximum velocity of a tail strike from the scorpion species Leiurus quinquestriatus (*58*). Additionally, the curling actuator achieved a maximum angular velocity of 1987° s^{-1} and a blocked tip force of 550 mN. Moreover, the design of the corrugated structure can be altered to change the mode of actuation. Figure 3.3e demonstrates a corrugated structure which follows the shape of a Fibonacci spiral. A strain limiting layer was used to force the spiral shape to bend and twist upon application of voltage.

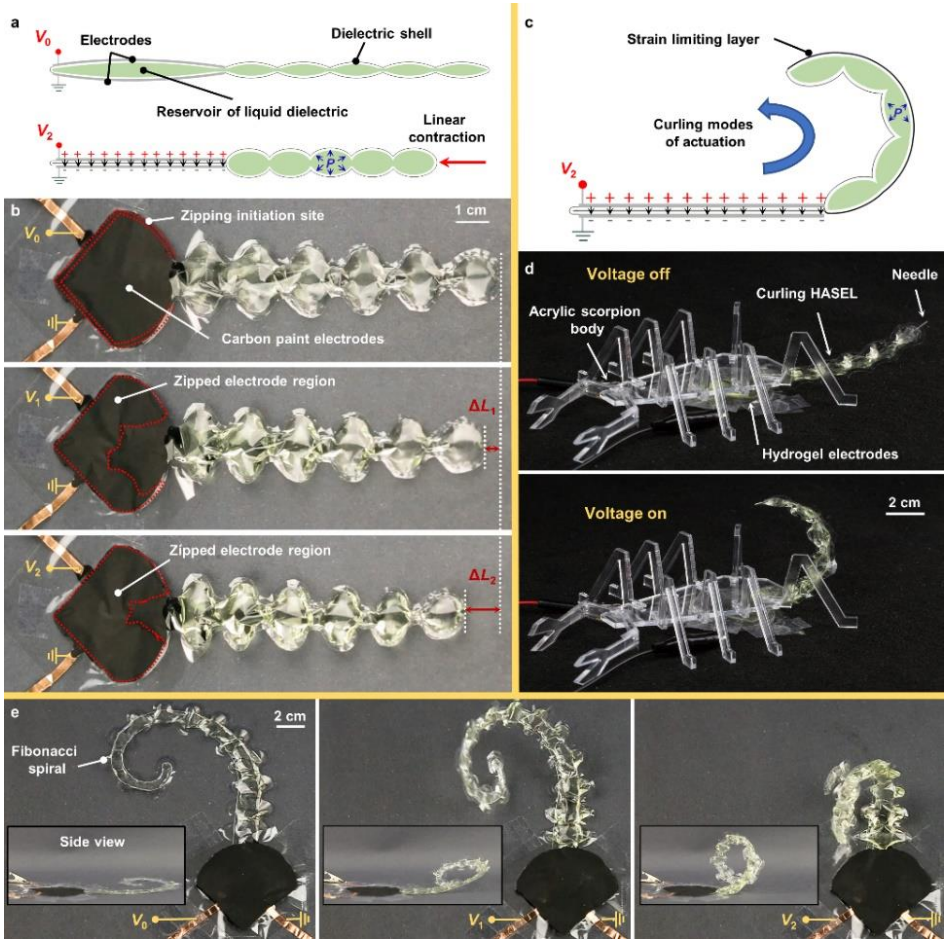

Figure 3.3: Bioinspired HASEL actuators that contract, bend, or twist. (*53*)

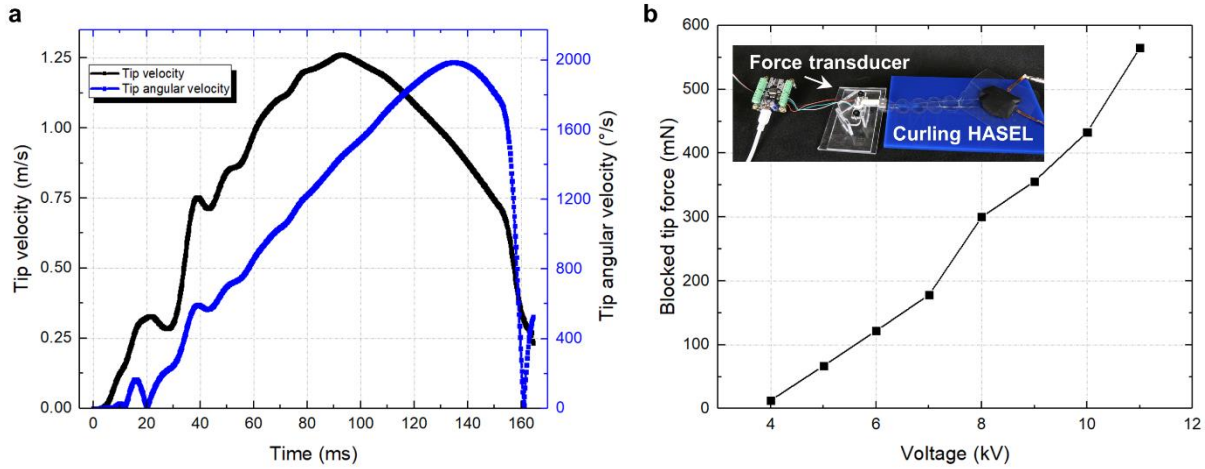

Figure 3.4: Performance metrics of curling HASEL actuators. a) The tip velocity in m s^{-1} and tip angular velocity in ° s^{-1} was plotted against time. b) The blocked tip force in mN was plotted as a function of voltage. (*53*)

3.2.3 Donut HASEL actuators that harness electrostatic zipping mechanisms

Donut HASEL actuators detailed in Section 2.2 showed promise as high speed and efficient linear actuators with tailorable stress-strain curves through electrohydraulic coupling. However, these actuators required voltages above 15 kV to achieve strains of about 40% under loads of ~1 N. These voltages were necessary to produce high electric fields across the relatively thick (~1 mm) silicone elastomers used as the dielectric shell.

Using the CNC heat sealing machine and thin-film BOPP (18-μm-thick) as the dielectric shell, we prototyped donut HASEL actuators which featured electrostatic zipping mechanisms. To better visualize the zipping mechanisms, transparent ionic conductors were used for electrodes; Figure 3.5a shows a basic design for a zipping donut actuator wherein electrodes were placed concentric to a small circular heat seal that was also concentric with the outer circumference of the actuator. The central heat seal resembled a dimple and acted as a zipping initiation site; when voltage was applied, the electrodes began to zip radially outward from this dimple.

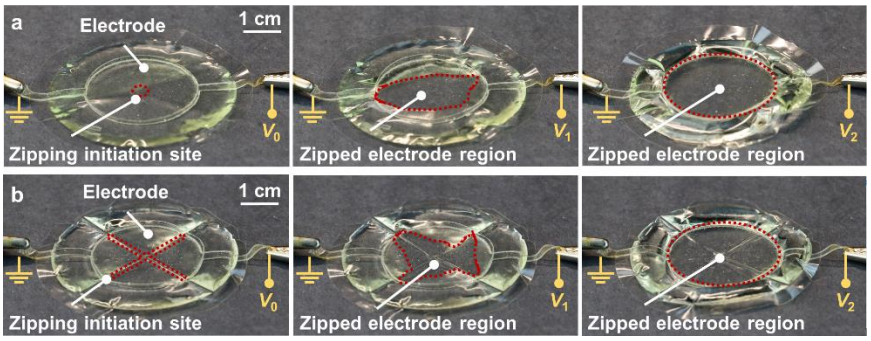

Figure 3.5: Design variations of donut HASEL actuators that feature electrostatic zipping mechanisms. a) A design that used a central circular heat seal ("dimple") to initiate zipping-mode actuation. As voltage was gradually increased from V_0 = 0 kV to V_1 = 2 kV to V_2 = 5 kV, the electrodes progressively zipped together without pull-in instabilities. b) To ensure a more homogeneous distribution of liquid dielectric during actuation, the shell of a donut HASEL actuator was divided into four equal quadrants using an "X"-shaped heat seal. This "X" acts as the zipping initiation site, and the electrodes progressively zip together as voltage is increased from V_0 to V_2. (*53*)

Dimpled donut HASELs showed a continuous response to input voltage and began to actuate at voltages as low as 2 kV. However, it was observed that when a few of these actuators were stacked on top of each other and placed under a mechanical load, the liquid dielectric in adjacent actuators was distributed unevenly in the outer regions of the shells, inhibiting each actuator in the stack from taking a toroidal shape. This uneven distribution limited the linear expansion of the stack to values lower than expected from extrapolation of the stroke achieved by a single actuator. Figure 3.5b shows a donut HASEL actuator with a dielectric shell that was segmented into quadrants, each filled with the same volume of liquid dielectric. This segmentation resulted in a more homogenous distribution of the liquid dielectric during actuation under load, while also providing a larger zipping initiation site compared to the dimpled donut actuators.

Figure 3.6 compares dimpled donuts to quadrant donut HASELs under a 500 g load. Figure 3.6a shows that one dimpled donut achieved a larger actuation strain (11% at 4 kV and 56% at 10 kV) as compared to one quadrant donut (2% at 4 kV and 41% at 10 kV). However, a stack of three

dimpled donuts generated an actuation strain of only 20% at 10 kV, whereas a stack of three quadrant donuts achieved 72% at 10 kV, Figure 3.6b.

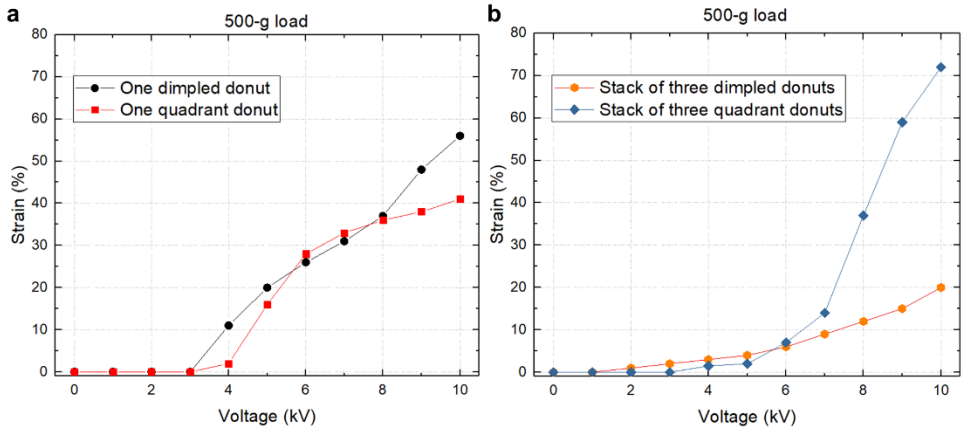

Figure 3.6: Comparison of dimpled donut and quadrant donut HASELs. a) Strain-voltage plot of one dimpled donut HASEL and one quadrant donut HASEL each under a 500-g load. b) Strain voltage plot of a stack of three dimpled donut HASELs and a stack of three quadrant donut HASELs each under a 500-g load. (*53*)

3.2.4 Quasi-static performance of quadrant donut HASEL actuators

The quasi-static actuation characteristics of a stack of three quadrant donut HASELs are shown in Figure 3.7. Under a 1 N load, the stack of actuators achieved a linear strain of 15% at 4 kV and a maximum strain of 118% at 12 kV, Figure 3.7a. The blocked force for this stack of actuators was above 60 N and was ultimately limited by the strength of the heat seals, Figure 3.7b.

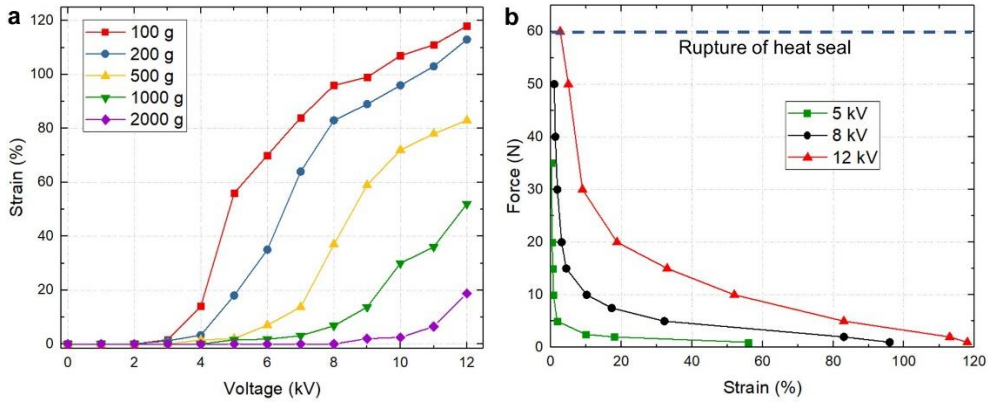

Figure 3.7: Quasi-static performance of a stack of three quadrant donut HASELs. a) Strain as a function of voltage for various mechanical loads. The curves do not highlight a noticeable pull-in instability due to the zipping initiation site created by the 'X'-shaped heat seal. b) Force-strain

curves at three different voltages. The curve at 12 kV corresponds to a specific energy of 12 J kg^{-1}. (*53*)

The full-cycle electromechanical efficiency of the actuators was also measured using the same experimental setup as seen in Figure 2.7 in Section 2.2.5. We measured an efficiency of 19.4%. 15.6%, and 13.6% for one actuator, a stack of three, and a stack of 11, respectively (Figure 3.8a). Figure 3.8b shows that the input electrical energy increases disproportionally to the output mechanical work as the number of actuators in the stack is increased. We hypothesize this trend is due to mechanical losses between adjacent actuators during expansion.

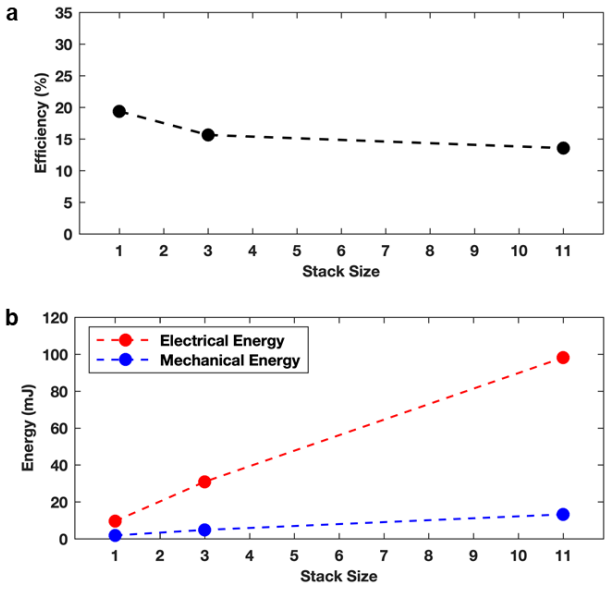

Figure 3.8: Full-cycle electromechanical efficiency of quadrant donut HASEL actuators as a function of the number of actuators in a stack. a) The efficiency of a single actuator, a stack of three actuators, and a stack of 11 actuators. b) Electrical energy consumed and the mechanical energy output by the actuator(s) as the number of actuators in a stack was increased. (*53*)

3.2.5 Dynamic performance of quadrant donut HASEL actuators

The relatively large zipping initiation site of quadrant donut HASELs promoted high-speed actuation; Figure 3.9a shows a stack three actuators achieved a strain rate of 4800% s^{-1} at 12 kV under a 1 N load, and nearly 300% s^{-1} under a 20 N load. Furthermore, the stack of three actuators

demonstrated a peak specific power of 121 W kg^{-1} (Figure 3.9b). Specific power was measured by optically tracking the displacement of the actuator under load (Figure 3.10a), and then taking the first and second derivative of the displacement data over time to yield the velocity and acceleration of the load, respectively. The mechanical power of the actuator was determined using the equation

$$P(t) = \frac{d(KE)}{dt} + \frac{d(PE)}{dt} = \frac{d(\frac{1}{2}mv(t)^2)}{dt} + \frac{d(mgy(t))}{dt} = mv(t)[a(t) + g] \quad (3.1)$$

where *KE* is the kinetic energy of the load, *PE* is the potential energy of the load, *m* is the mass of the load, *y(t)* is the vertical position of the load, *v(t)* is the velocity of the load as a function of time, *a(t)* is the acceleration of the load as a function of time, and g is the acceleration due to gravity. We normalized the power output by the mass of the actuators to determine the specific power. Average power was determined from the time, t_1, when the actuator began to expand, to the time, t_2, when the actuator was no longer providing positive power to lift the load (Figure 3.10b-e).

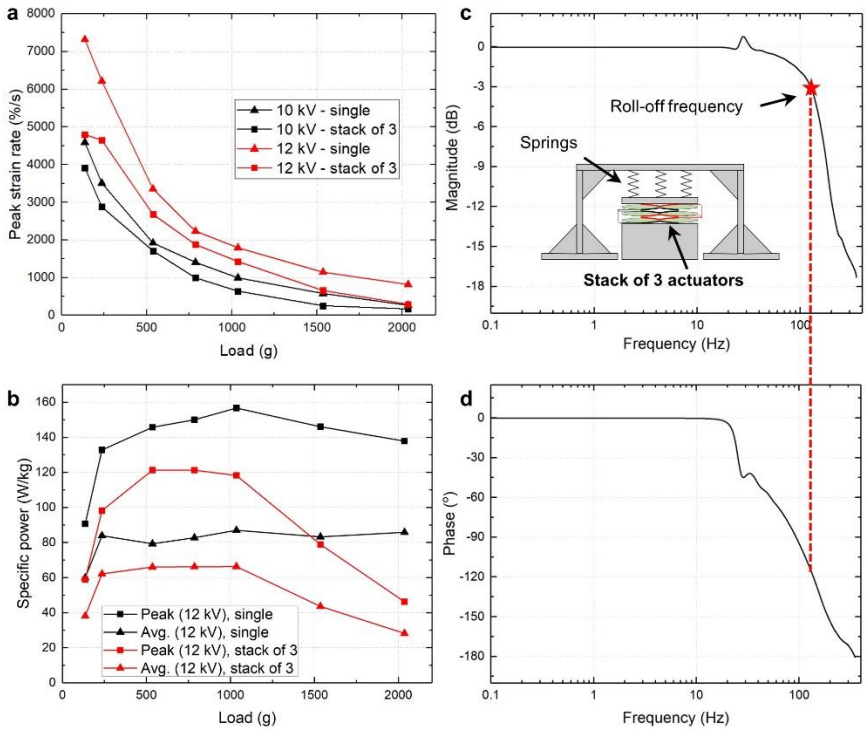

Figure 3.9: Dynamic performance of quadrant donut HASELs. a) Peak strain rate as a function of load for one actuator and a stack of three actuators driven to 10 kV and 12 kV. b) Peak and average

specific power as a function of load for one actuator and a stack of three actuators driven to 12 kV. c,d) A Bode plot for the stack of three actuators, where 0 dB corresponds to 25% strain. The actuators achieved muscle-like strains (~20%) beyond 100 Hz. The inset schematic in (c) depicts a spring platform that was used to provide a restoring force during characterization of frequency response. (*53*)

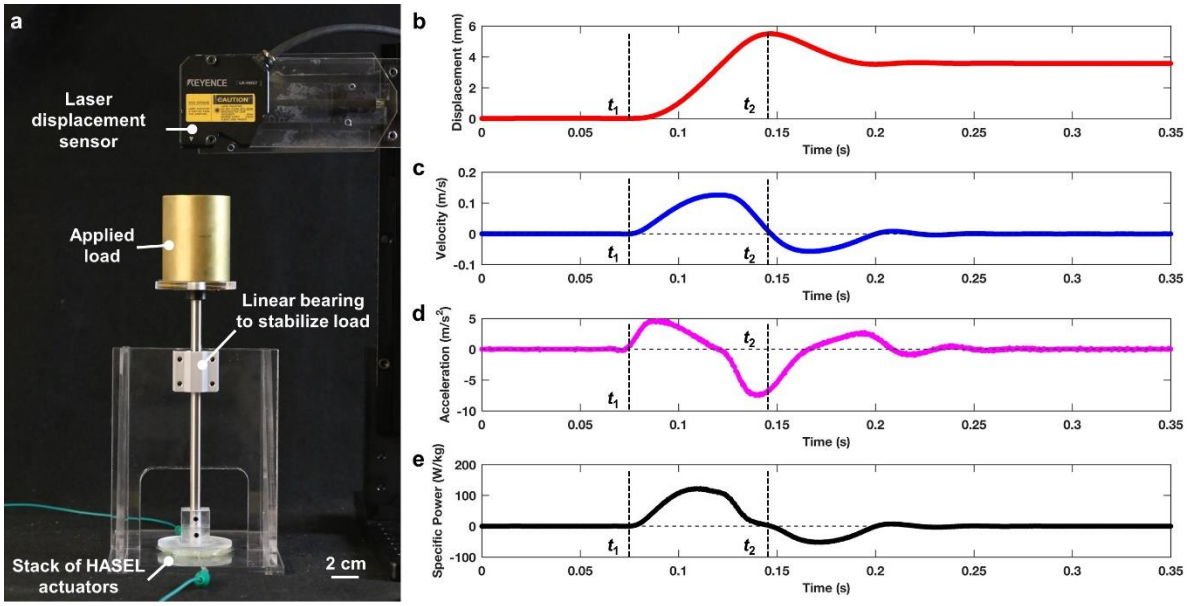

Figure 3.10: Measuring the specific power output of quadrant donut HASELs. a) The experimental setup. b) Vertical displacement, c) velocity, d) acceleration, and e) Specific power as a function of time. This specific data set shows the response of a quadrant donut HASEL under a 536-g-load driven by a 12 kV voltage step. (*53*)

Using the specific test setup shown in the inset of Figure 3.9c, which consisted of three springs and a rigid acrylic platform to provide a restoring force, we measured a flat frequency response at 25% strain until roll-off at 126 Hz (Figure 3.9c,d). The small peak seen in the frequency response (~30 Hz) was attributed to a resonance in the test setup. Using a test setup with a different restoring force would affect these results; a lower restoring force would allow the actuators to achieve a larger stroke and generate more inertia, and therefore the roll-off frequency would decrease. Conversely, if a larger restoring force was used, the actuators would achieve less strain, but would roll-off at higher frequencies.

3.2.6 A modular approach to stacks of HASEL actuators

After the mechanical performance of quadrant donut HASELs was understood, a modular design approach for stacks of donuts HASEL actuators was developed. The construction procedure was as follows (Figure 3.11):

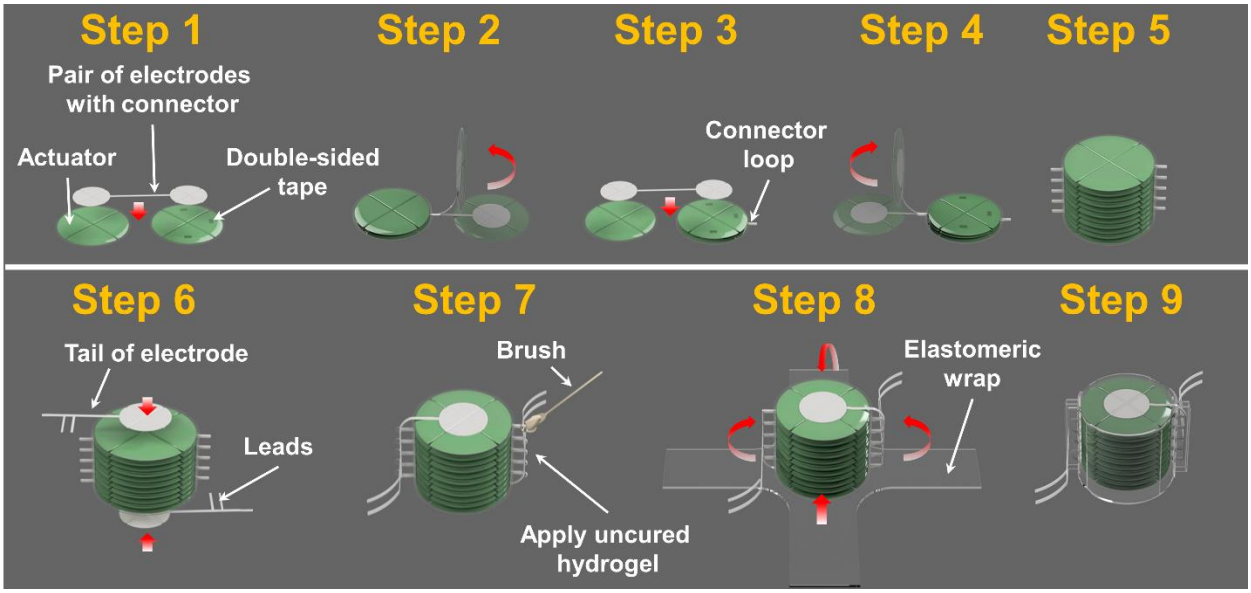

Figure 3.11: Stacking process to create modular units of quadrant donut HASELs. (*53*)

Step 1 – Hydrogel electrodes were laser cut in pairs with a connector. One electrode of the first pair was applied to the first actuator and the other electrode of the first pair was applied to the second actuator. Three strips (each 1 mm x 3 mm) of permanent double-sided tape (Scotch, 3M) were placed on the shell of the second actuator in locations that remained in contact with the first actuator during operation.

Step 2 – The second actuator was folded on top of the first actuator with their heat seals aligned forming a stack of two actuators. This process created a loop of hydrogel electrode (from the connector between the pair of electrodes) which protruded from one side of the actuators.

Step 3 – One electrode of a second pair of electrodes was applied to the exposed side of the second actuator and the other electrode was applied to a third actuator. Three strips of double side tape were placed on the exposed side of the second actuator.

Step 4 – The third actuator was folded on top of the second actuator, thereby creating a stack of three actuators. The loop of hydrogel created from this process protruded from the other side of the stack relative to the first loop. Double-sided tape was placed on the exposed side of the third actuator.

Step 5 –The previous steps were repeated for subsequent actuators added to the stack, until the desired number of actuators was achieved (11 actuators for modular units described in section).

Step 6 – Once 11 actuators were stacked, electrodes were placed on the top and bottom of the stack. Each of these electrodes had tails which were long enough to contact all the loops of hydrogel protruding from a side of the stack. Additionally, the tails had two perpendicular leads which allowed electrical connection to a HV power supply, as well as electrical connection to adjacent modular units.

Step 7 – Several drops of uncured hydrogel were applied between the electrode loops and the tails of the top and bottom electrodes, and the stack was exposed to 365-nm UV light for 1 hour or until the drops of hydrogel had polymerized. This process ensured that the electrodes of adjacent actuators were electrically connected.

Step 8 – A 100-μm-thick elastomeric wrap made from Ecoflex 00-10 was placed under the stack. The wrap had four tabs which were folded up and wrapped around the stack of actuators.

Step 9 – The completed modular unit of actuators.

Figure 3.12a shows an aerial view of a modular unit actuating at 8 kV, while Figure 3.12b shows a side view of the unit at three different voltages. Additionally, large actuation strains (~40%) were observed at driving frequencies of 15 Hz, Figure 3.12c. The segmented shell of each actuator in the modular unit confines the liquid dielectric to discrete regions of each actuator and the elastomeric wrap provides a restoring force to the module, enabling the unit to effectively operate in various orientations regardless of the effects of gravity. The strain as a function of voltage for a modular unit of quadrant donut HASELs was measured at three different orientations (upright, sideways, and upside-down), and showed that the strain of one modular unit is largely unaffected by the orientation of the actuator.

The low weight of the modular units (~26 g) combined with their high-speed actuation characteristics and large strokes allowed them to jump without relying on external power amplifying mechanisms (Figure 3.12d). When a 7.8 kV, 3.9 Hz driving signal was applied, the stack jumped off the ground repeatedly with its center of gravity reaching a maximum height of ~5 cm. The elastomeric skin was removed from the modular unit in this case as it adhered to surfaces preventing the actuator from fully lifting off the ground.

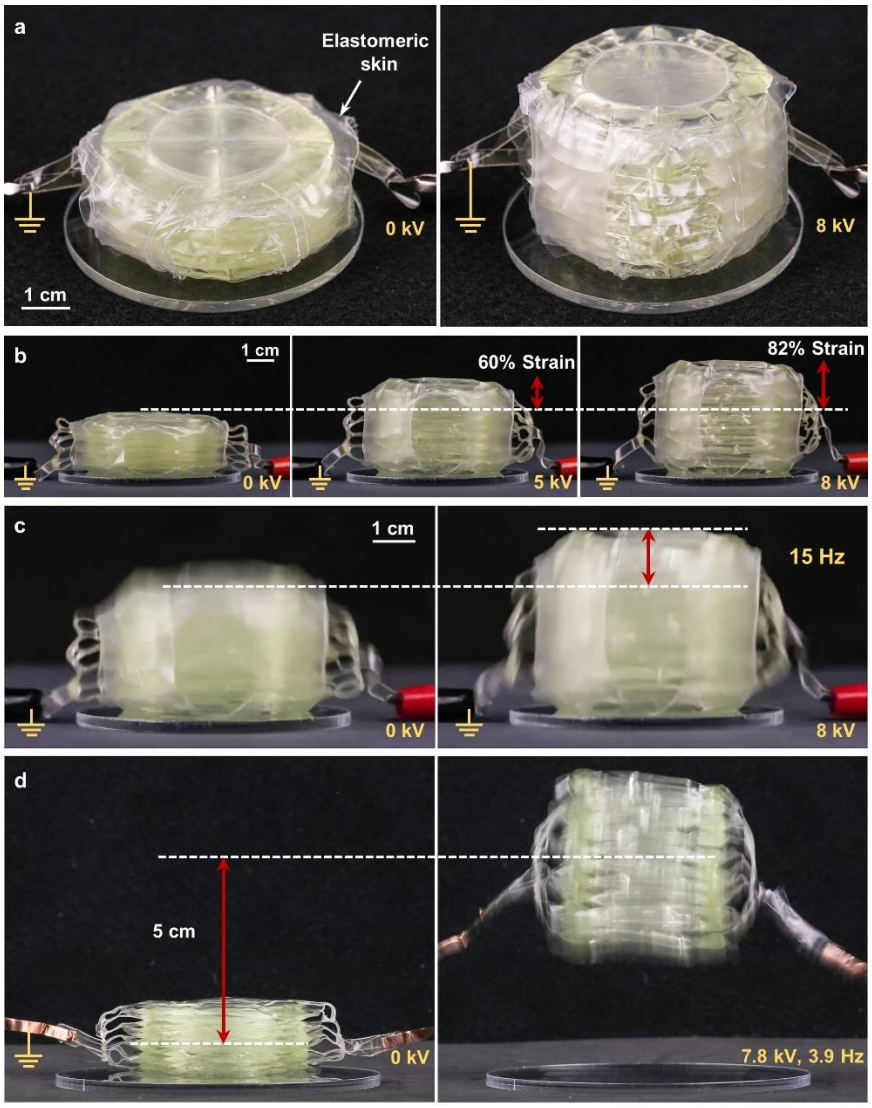

Figure 3.12: Performance demonstration of stacked quadrant donut HASELs. a) An aerial view of a modular unit of actuators, defined as a stack of 11 quadrant donut HASELs. b) These modular units demonstrate a smooth actuation response to input voltage, with strains of 60% at 5 kV and 82% at 8 kV. c) The stacked actuators maintain large strains (>40%) at high frequencies (15 Hz). d) High specific power enables actuators that jump without additional power-amplifying mechanisms. (*53*)

3.2.7 Portable high voltage electronics to drive HASEL actuators

The work presented thus far has demonstrated HASELs as muscle-mimetic electrohydraulic actuators. The driving stimulus for these actuators requires high voltage (on the order of kilovolts) but relatively little current (on the order of microamps to milliamps). Therefore,

this electrical power requirement is generally only single digit Watts and can be generated by altering the output power of a standard lithium polymer battery.

We built the first battery powered HVPS to drive HASEL actuators, with the electrical schematic for the circuit shown in Figure 3.13. This circuit was based on the open source power supply developed by PetaPicoVoltron (*59*) which has been utilized to drive DEAs for applications in soft robotic grippers and active substrates (*60*, *61*). The circuit developed here was modified for higher voltage and power output; a 5 W high voltage amplifier was used to generate a proportional output voltage of 0–10 kV from a 0–5 V input. Optocouplers were used as high-speed, HV switches to charge and discharge the actuators, allowing a maximum charging and discharging current of 0.3 mA. Therefore, the maximum continuous power draw by the actuators was restricted to 3 W. The optocouplers were oriented in an H-bridge configuration to reverse the polarity of the voltage applied to the actuators. A 3.7 V, 500 mAh lithium polymer battery with a 5 V power booster were used to power the circuit, while a microcontroller was used to switch the optocouplers and modulate the voltage and frequency input to the actuator. This proof-of-concept electronics package fit in the palm of a hand and weighed ~100 g. Figure 3.14 shows a stack of donut HASEL actuators powered by a portable HV electronics package could easily lift its entire driving electronics and battery, operating completely untethered from any additional energy source.

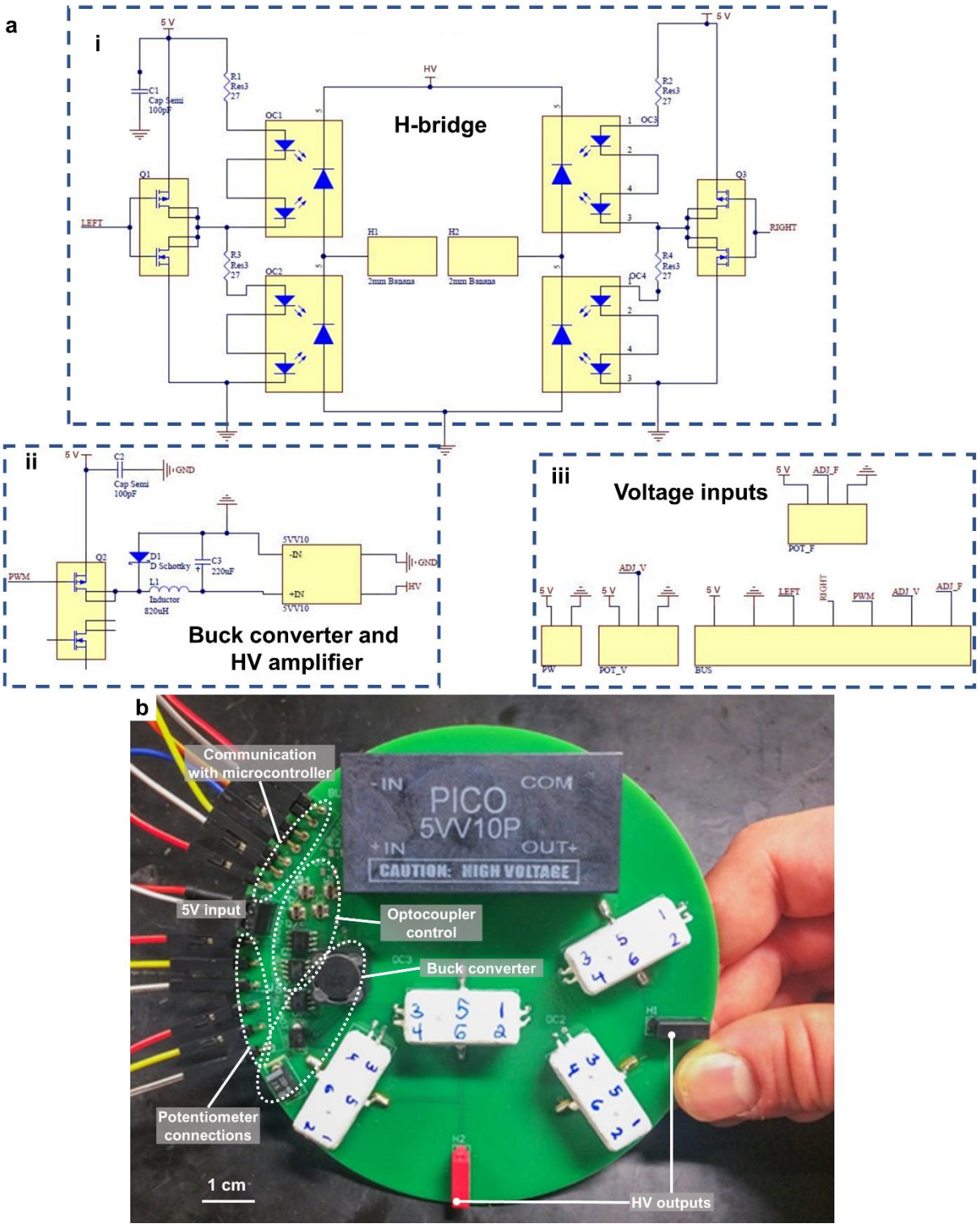

Figure 3.13: Initial prototype of a portable high voltage power supply. a) The electrical schematic for the power supply which includes (i) an H-bridge constructed from optocouplers for HV switching, (ii) a buck converter to modulate the input voltage to the HV amplifier, and (iii) buses for voltage inputs. b) The completed power supply. (*53*)

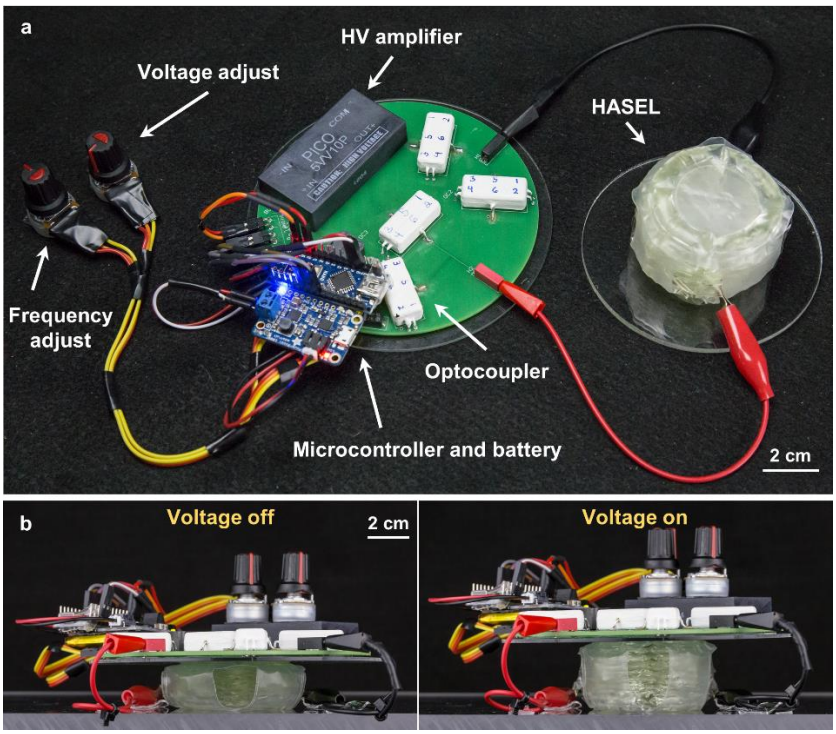

Figure 3.14: Compact high-voltage electronics for untethered operation of HASEL actuators. a) A proof-of-concept power supply was constructed using only off-the-shelf components and was shown to operate a modular unit of actuators. b) The modular unit was operated at 8 kV and could easily lift its entire power supply including the battery. (*53*)

3.2.8 Enhancing functionality with a multi-channel high voltage power supply

Moving toward untethered soft robots with increasing complexity, we developed a three-channel HV power supply for independent control of multiple modular units of HASEL actuators. Three of the HV power supplies shown in Figure 3.13 shared a common ground and interfaced with a microcontroller (Elegoo, EL-CB-001 UNO) which mapped analog input signals from a modified video game controller to the input of each HV amplifier, Figure 3.15a. This mapping was developed by representing all possible locations of the joystick within the area of a unit circle, whose origin coincided with the origin of the Cartesian coordinate system, Figure 3.15b. The three actuators were represented as unit vectors $\overrightarrow{v_1}$, $\overrightarrow{v_2}$, and $\overrightarrow{v_3}$, on the unit circle, where each actuator was 120º apart, and $\overrightarrow{v_1}$ coincided with the positive x-axis. Similarly, the physical location of the

joystick was represented as a vector, $\vec{u}$, (highlighted in red) with a length that varied from 0 to 1. When the joystick was at its origin, magnitude of the vector, $|\vec{u}|$, was zero. When the joystick was fully tilted, the magnitude of the vector $|\vec{u}|$ was 1. The magnitude of the voltage which was applied to any of the actuators depended on the location of the joystick in the unit circle. This voltage regulation was based on the projection of $\vec{u}$ onto the unit vectors of each actuator, where $\overrightarrow{p_1}$, $\overrightarrow{p_2}$, and $\overrightarrow{p_3}$ are the projections onto $\overrightarrow{v_1}$, $\overrightarrow{v_2}$, and $\overrightarrow{v_3}$, respectively. Voltage applied to the actuator was non-zero and scaled linearly by the magnitude of the projected vector if and only if the projected vector was pointing in the opposite direction of the unit vector of the actuator. An example is given in Figure 3.15b – when the joystick is moved to the first quadrant of the unit circle, the projected vectors $\overrightarrow{p_1}$ and $\overrightarrow{p_3}$ are in the same direction as $\overrightarrow{v_1}$ and $\overrightarrow{v_3}$, respectively, so the actuators associated with $\overrightarrow{v_1}$ and $\overrightarrow{v_3}$ do not activate. However, the projected vector $\overrightarrow{p_2}$ is in the opposite direction of $\overrightarrow{v_2}$, so the actuator described by the vector $\overrightarrow{v_2}$ activates, and the magnitude of the voltage applied to this actuator is proportional to $|\overrightarrow{p_2}|$. The magnitude of the voltage applied to each actuator was limited to 8 kV to prevent accidental electrostatic discharge across the PCB. It was observed that when the joystick was at rest at its origin (x = 0 and y = 0), the actuators would not always discharge appropriately. This issue was attributed to imperfections of the joystick, which prevented it from perfectly returning to its origin. To circumvent this issue, a smaller circle concentric to the unit circle was constructed. Projected vectors with magnitude less than the radius of this second circle would cause the actuator(s) to discharge. Due to the need to reverse polarity between actuation cycles, this algorithm was designed so that the same polarity was never applied to the same actuator more than one time in a row. Additionally, the algorithm included a command which would activate all actuators simultaneously when the built-in switch of the joystick was pressed.

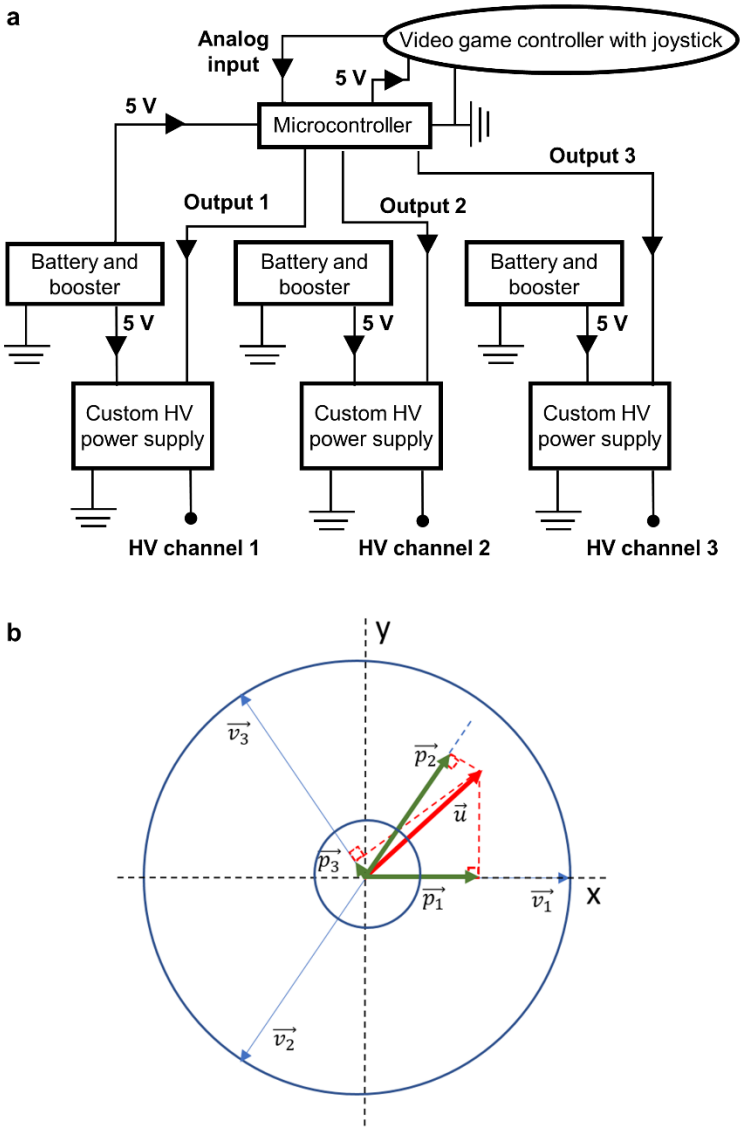

Figure 3.15: Three-channel high voltage power supply with joystick control. a) A block diagram of the three-channel power supply. The microcontroller supplied 5 V to the joystick controller. In turn, the controller sent analog signals to the microcontroller that mapped those signals to each HV power supply. Outputs of the microcontroller sent a PWM signal to the buck converter of each power supply and a digital signal to the H-bridge of each power supply to control the optocouplers. Each power supply has its own battery and 5 V regulator, while one of these batteries also supplied power to the microcontroller. b) A unit circle which describes how the Arduino algorithm maps the position of the joystick to the outputs of the three-channel HV power supply. (*53*)

The output of each channel was connected to a modular unit of HASELs, and the three units were oriented in a triad configuration as seen in Figure 3.16a. The modular units could be stacked on top of each other and electrically connected in parallel to further scale up the actuation

stroke. We used three columns each consisting of four modular units to construct an untethered continuum robot capable of three-dimensional mobility, Figure 3.16b,c. Each layer of modular units was separated by a thin acrylic spacer to provide mechanical stability to the system, and each spacer was anchored to the plate above and below it with either elastic bands made from Ecoflex 00–30 or fishing line which was used to limit the strain of each unit to 100%. These anchors prevented the robot from toppling over as it bent in various directions. This soft robot could bend following the movement of the joystick or linearly expand by activating all modular units simultaneously via the press of a button embedded in the controller, Figure 3.16c.

With a maximum power output of 3 W from each channel, actuation speed was limited when scaling up the number of modular units in each column as the overall value of the capacitive load increased with more modular units. If high speed operation of stacks consisting of many modular units is desired, a high-voltage amplifier with a higher power output would yield a proportional increase in the response speed of the device. To demonstrate high-speed operation of HASEL actuators using the portable three-channel power supply developed here, we reduced the total capacitive load of each channel to only one modular unit and used the resulting device to precisely control the position of a marble moving through an acrylic maze, Figure 3.16d. Additionally, three columns each consisting of two modular units were shown to achieve linear strains of 70% under no load and were strong enough to achieve 40% strain under a 1 kg weight, Figure 3.16e.

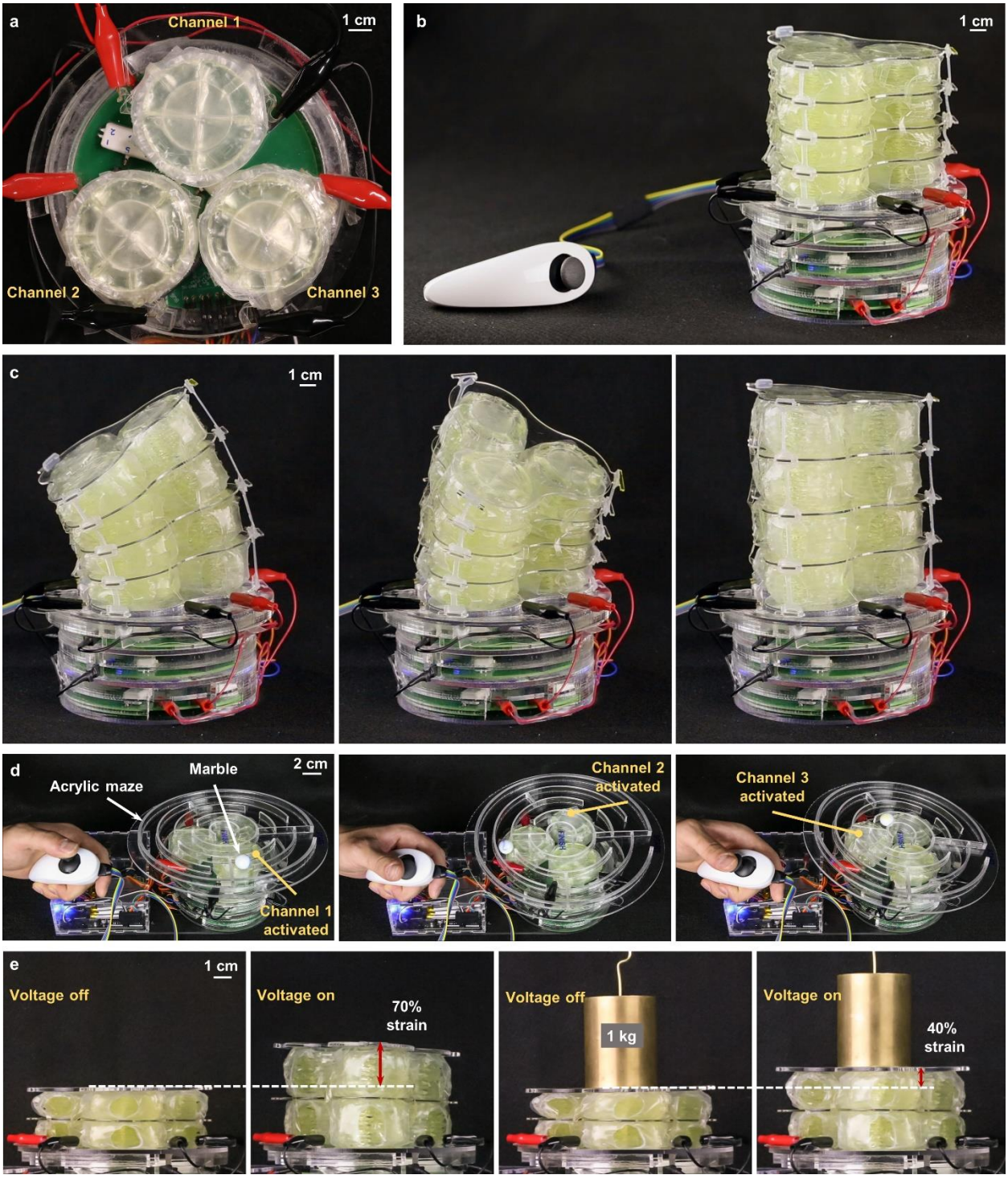

Figure 3.16: Untethered continuum robot based on modular units of HASEL actuators. a) Three modular units of HASEL actuators were oriented in a triad configuration. Each unit was connected to one channel of the custom power supply and activated with a voltage ranging from 0 to 8 kV. b) The continuum robot consisted of three columns each comprised of four modular units electrically connected in parallel. Each column was independently controlled by a joystick. c) Independent control of each column caused the robot to bend in various directions following the movement of the joystick, while activating all columns simultaneously caused the robot to linearly

expand. d) An interactive game was created by placing an acrylic maze on top of three modular units of HASELs. A player navigated a marble through the maze using the joystick. e) Three columns each consisting of two modular units demonstrated 70% linear strain under no load and 40% under 1 kg. (*53*)

Aiming to create an untethered, electrically powered soft robot based on HASEL actuators for grasping and manipulation, we combined several capabilities in this work, Figure 3.17. We used three columns each consisting of five modular units of donut HASELs as a continuum actuator, while our fabrication technique allowed us to prototype a soft gripper based on curling HASEL actuators for the end effector. A four-channel power supply based on the portable HV electronics described above enabled three-dimensional motion of the end effector as well as opening and closing of the gripper. The HV transmission lines for the gripper were routed through the gap in the middle of the three columns, and the gripper was activated via a push button embedded in the joystick controller. This soft robot, named Terry the trunk, was adept at grasping and repositioning objects handed to it by a person such as a flower, a balloon, or a bag of chips.

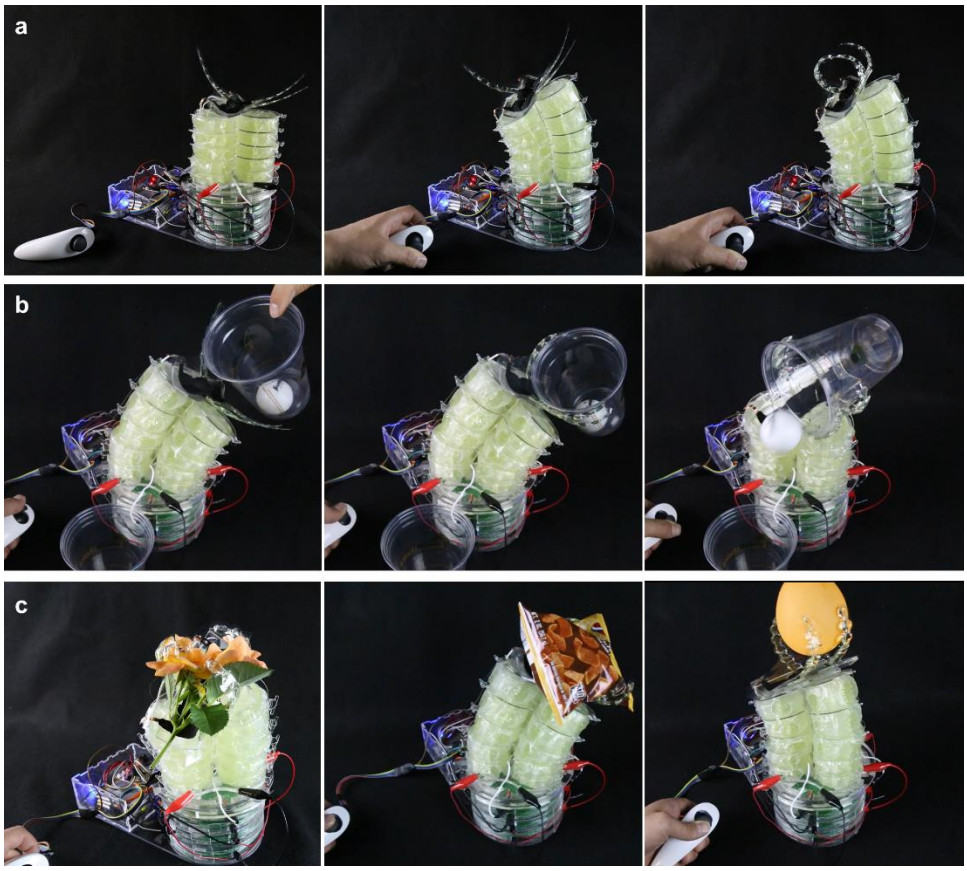

Figure 3.17: Towards an untethered continuum robot: Terry the trunk. (*53*)

3.3 Outlook

The high-performance actuators created from the easy-to-implement fabrication technique presented in this work offered tunable actuation modes; they could be designed to expand, contract, rotate, or any combination of the three. These characteristics are achieved using only commodity materials (~$0.10 in materials per actuator). However, electrical self-healing was unreliable using the discussed material system, as dielectric breakdown events would melt small holes in the thin thermoplastic sheets of BOPP allowing the liquid dielectric to leak from the actuator (*50*). Nevertheless, the largest electric field used to achieve the reported actuation performance is ~333 V μm^{-1}, which is well below the maximum dielectric strength of BOPP (~700 V μm^{-1}) allowing for reliable actuation without dielectric breakdown.

As a new actuator technology, HASELs require fundamental studies to guide material selection (*62*), elucidate scaling laws, and determine methods to circumvent charge retention in the actuator. Currently, charge retention within the BOPP-based HASEL actuators necessitates reversing the polarity of voltage during subsequent actuation cycles which increases the complexity and size of the driving electronics.

Although the voltage used for actuation in this work is substantially lower than reported values by Acome *et al*. (*47*), it still is in the kilovolts range; thus, electrical safety needs to be considered when operating HASELs in close proximity to humans. However, it is important to note that the actuators and high voltage power supply developed here do not present a safety concern, because the maximum capacitance of the actuators and the charging/discharging currents are low (on the order of 10 nF and <1 mA, respectively), while the equivalent series resistance of the electrodes is high ($>10^3$ Ω) (*63*). To further reduce the risk of accidental electrostatic discharge, the operating voltages of HASEL actuators can be decreased by using thinner solid and liquid dielectric layers and by increasing the electrical permittivity of these layers.

Untethered operation of soft robots is critical for applications like wearable and field robotics (*64*) where these machines must operate without being constrained by their power sources (*65*). While the power supply developed in this work was shown to effectively drive untethered modular units of HASEL actuators through a user input, a closed-loop controller is necessary for autonomous operation of these devices. This controller could rely on the self-sensing mechanism inherent to HASEL actuators (*47*, *50*, *66*). Additionally, the use of high voltage power supplies, switches, and soft logic developed for DEAs (*67–69*) could enable further miniaturization of the driving electronics for integrated actuation, sensing, and control of arrays of modular HASELs.

The introduced fabrication technique was effective for prototyping different designs of HASEL actuators, but the throughput of this method was limited. Nevertheless, the discussed technique provides a wide audience of roboticists, researchers from neighboring fields, and even hobbyists with a simple and inexpensive tool to explore and create HASEL actuators with muscle-like performance.

4 High strain Peano-HASEL actuators

4.1 State of the art

Peano-HASEL actuators linearly contract upon application of voltage, closely mimicking the fast and precise actuation behavior of muscle. They are predicted to exceed the energy density of muscle (*70*); therefore, Peano-HASELs are well suited as actuators in bioinspired and biomimetic systems. However, the maximum theoretical strain of these devices is 24%, and only ~15% strain has been demonstrated experimentally (*70*), while natural muscle typically operates at 20% strain and achieves maximum strain of up to 40%.

4.2 Contributions to expand the state of the art

This work (*71*) focused on designing a variation of Peano-HASEL actuators, termed high-strain (HS) Peano-HASELs, that achieves linear contraction up to ~24%. Additionally, these actuators present well-rounded actuation performance including specific power of 120 W kg^{-1} and strain rates greater than 2,000% s^{-1}. Moreover, the maximum strain of multiunit HS-Peano-HASEL actuators is optimized by varying materials and geometry. An artificial circular muscle (ACM) based on the HS-Peano-HASEL acted as a tubular pump, resembling the primordial heart of an ascidian. The muscle-like maximum actuation strain and excellent all-around performance of HS-Peano-HASEL actuators make them promising candidates for use in artificial organs, life-like robotic faces, and a variety of other robotic systems.

4.2.1 Design of high-strain Peano-HASEL actuators

This design is different from previously reported Peano-HASEL actuators, because the electrodes covers the top half of the shell across the entire width of Peano-HASELs. The zipping region and the contraction region are therefore aligned in the direction of contraction. Thus, the zipping region contributes to the initial length of the actuator but does not contract during actuation, and consequently the maximum theoretical actuation strain of Peano-HASEL actuators with electrodes that cover half of each unit is limited to 18% (while only ~15% has been demonstrated experimentally (*70*)). In HS-Peano-HASEL actuators, the zipping region and the contracting region are aligned orthogonally to the direction of contraction (Figure 4.1). Therefore, HS-Peano-HASEL actuators can achieve a maximum theoretical actuation strain of 36%.

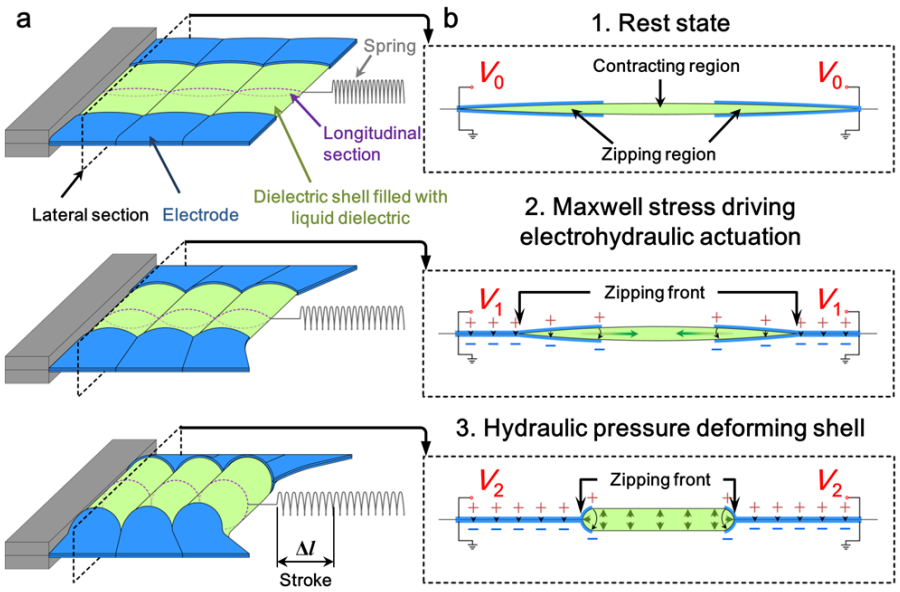

Figure 4.1: Design and operating principle of high-strain Peano-HASEL actuators. (*71*)

4.2.2 Quasi-static performance

We measured the quasi-static load-strain characteristics of a single unit HS-Peano-HASEL actuator. For comparison, we also measured the load-strain curve of a single-unit Peano-HASEL actuator with the same mass, materials, shell length, and maximum capacitance when electrodes

are fully zipped (Figure 4.2a). With these design choices, the specific energy of both actuators should be the same, theoretically. At small loads (<6 N), the HS-Peano-HASEL actuator showed larger strains than the Peano-HASEL actuator (Figure 4.2b). The maximum strain of the HS-Peano-HASEL actuator was 23.58% whereas the maximum strain of the Peano-HASEL actuator was 8.96% under a load of 0.2 N. At large loads (>6 N), the actuation strain of the Peano-HASEL actuator exceeded the actuation strain of the HS-Peano-HASEL actuator. The blocking force of the Peano-HASEL actuator (65 N) was larger than the blocking force of the HS-Peano-HASEL actuator (18 N). The decrease of the blocking force can be explained with energetic considerations. Because both actuators were designed to have the same maximum capacitance (when the electrodes are fully zipped together), shell length, and mass, they ideally have not only the same specific energy but also the same area under the load–strain curve. Thus, increasing the strain of the actuator leads to a decrease of the maximum load. The experimentally measured specific energy of the Peano-HASEL actuator was 4.93 J kg^{-1} and of the HS-Peano- HASEL actuator was 4.03 J kg^{-1}. We hypothesize that the difference in specific energy stems from the mechanical constraints due to buckling at the transition zones between the zipping and contracting regions in the HS-Peano-HASEL actuator.

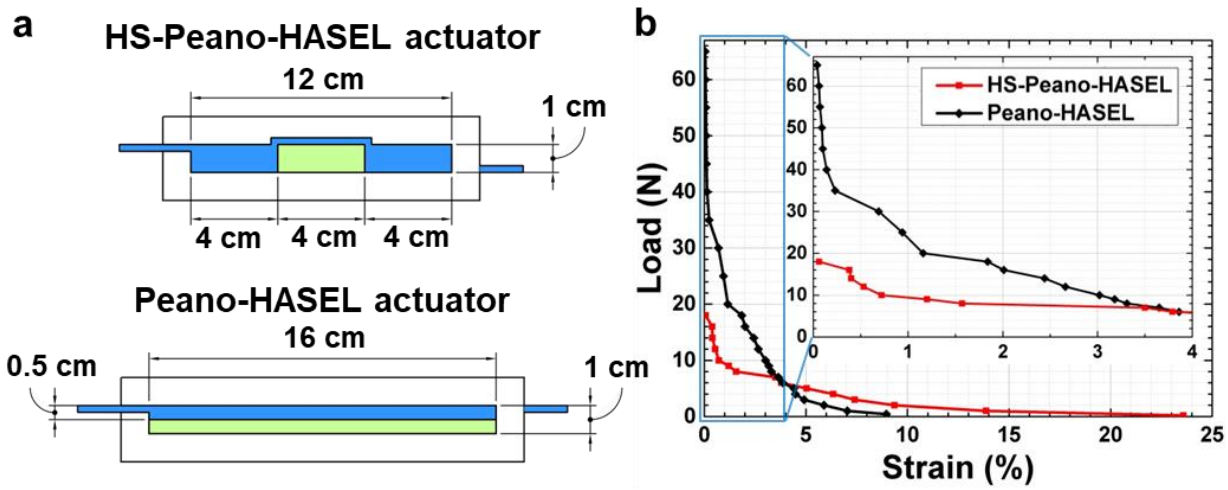

Figure 4.2: Comparison of the quasi-static performance of a Peano-HASEL and a HS-Peano-HASEL. (*71*)

Furthermore, we derived a simple analytic model that describes the quasi-static load-strain behavior of the HS-Peano-HASEL actuator, Figure 4.3. The shell of the actuators consists of two flexible but inextensible, rectangular sheets of width W and length L that are bonded at the edges to form a rectangular shell. We assumed the thickness t of the sheets to be sufficiently thin to be able to neglect their bending stiffness. We also neglect edge effects at the ends of the actuator.

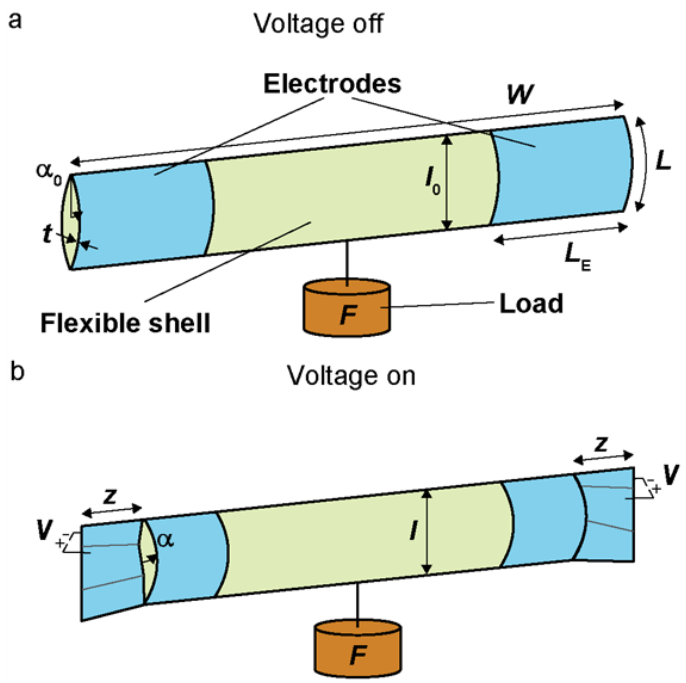

Figure 4.3: Parameterization of the pouch of a HS-Peano-HASEL actuator. (*71*)

With these assumptions, the shell takes the shape of two intersecting cylindrical sections with central angle $2\alpha_0$, when it is filled with an incompressible liquid dielectric of volume υ and loaded with a weight, F. The angle α_0 can be calculated from

$$v = W * L^2 * \frac{2\alpha_0 - sin\,(2\alpha_0)}{4{\alpha_0}^2} \tag{4.1}$$

so that the initial length l_0 of the actuator becomes

$$l_0 = \frac{L * sin(\alpha_0)}{\alpha_0} \tag{4.2}$$

At each end, electrodes of length L_E cover the shell on both sides. When a voltage is applied to the electrodes, they zip together from the ends of the actuator over a length z, displacing the liquid dielectric toward the center, which leads to shortening of the center of actuator to a length l (Figure 4.3b). We neglect the transition zone between the zipping region of the electrodes and the contracting region of the actuator (we assume that the transition occurs in a discrete step). The

cross-section in the center of the actuator therefore retains the shape of cylinder section. The central angle 2α of this region can be calculated from

$$v = (W - 2z) * L^2 * \frac{2\alpha - sin\,(2\alpha)}{4\alpha^2} \tag{4.3}$$

The length of the actuator reduces to

$$l = \frac{L * sin(\alpha)}{\alpha} \tag{4.4}$$

so that the strain e of the actuator becomes

$$e = 1 - \frac{l}{l_0} = 1 - \frac{\alpha_0 * sin\,(\alpha)}{\alpha * sin\,(\alpha_0)} \tag{4.5}$$

The free energy of the system is

$$H = -QV + \frac{1}{2}\frac{Q^2}{C} - (l - l_0)F \tag{4.6}$$

which can be rewritten as

$$H = -QV + \frac{1}{2}\frac{tQ^2}{\varepsilon Lz} - (l - l_0)F. \tag{4.7}$$

In equation 4.7, Q is the charge on the electrodes of the actuator; V is the voltage applied across the electrodes; ε is the dielectric constant of the material of the shell; F is the load applied to the actuator. The first term describes the amount by which the free energy of the voltage source decreases when the charge Q flows from it to the electrodes. The second term describes the energy stored in the electric field in the zipped region, which we modeled as a plate capacitor (we neglect all contributions of the electric energy in the non-zipped region of the pouch). The third term describes the change of the free energy of the load when the actuator contracts. Because the bending stiffness of the films that form the shell is neglected and it is assumed to be inextensible, there is no contribution of mechanical energy of the film to the free energy. Minimization of equation 9 with respect to Q, z and l under the constraint of equation 4.3 (incompressibility of the dielectric liquid) leads to the equations of state (parameterized by α):

$$F = \varepsilon E^2 t(W - 2z)\frac{\alpha\, cos(\alpha)[2\alpha - sin(2\alpha)]}{(\alpha - sin(\alpha)\, cos(\alpha))^2} \quad (4.8)$$

$$Q = \varepsilon V \frac{L}{t}\left(\frac{W}{2} - \frac{v\alpha^2}{L^2(\alpha - sin(\alpha)\, cos(\alpha))}\right). \quad (4.9)$$

Similar to the model presented by Kellaris et. al for Peano-HASEL actuators (*70*), equation 4.8 is independent of the pouch length L, and thus, HS-Peano-HASELs should follow similar scaling laws as Peano-HASELs.

Figure 4.4 compares the experimental and the calculated load-strain curves. All calculated curves follow the experimental curves, but the experimentally measured strains are, on average, 40% smaller than the strains predicted by the model. We attribute the differences between the theoretical strain and the experimental strain to the side constraints of the actuator and the constraints at the transition zone between the zipping and contracting regions. During actuation, the cross section of the zipping region flattens, while the cross section of the contracting region takes a more circular shape; this mismatch in shape change leads to buckling of the shell and ultimately constrains the contracting region, which further leads to a loss in the experimentally achieved actuation strain. The model neglects the transition zone between the zipping region and the contracting region, and thus overestimates the actuation strain.

The model indicates how the force output of the actuator can be improved. The first factor on the right-hand side of equation 4.8 ($\varepsilon E^2 t(W - 2z)$) is a measure for the electrostatic force inside the zipped region of the electrodes. The strength of the actuator may be increased by increasing the applied voltage, making the actuator wider, or using shell materials with higher permittivity and/or thickness. Decreasing the fill volume also increases the strength of the actuator as it not only influences equation 4.8 but also leads to a decrease of α_0 (*70, 72*).

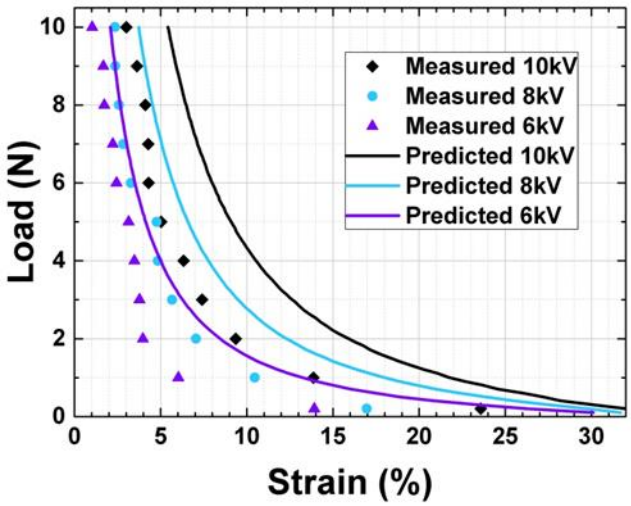

Figure 4.4: Comparison of measured and predicted quasi-static load-strain behavior of a HS-Peano-HASEL actuator. (*71*)

4.2.3 Notched electrodes

A method to reduce the mechanical constraints due to buckling at the transition zones between the zipping and contracting regions is to alter the geometry of the electrodes. We developed a notched geometry for the electrodes that leads to controlled buckling at this region when the electrodes are fully zipped. Compared to the rectangular screen-printed electrodes (Figure 4.5a), notched screen-printed electrodes (Figure 4.5b) reduced the decline of the actuation strain when increasing the number of actuator units for a BOPP-based HS-Peano-HASEL (Figure 4.5c). A four-unit HS-Peano-HASEL actuator under a 20-g-load and operated at 10 kV achieved 17.20% strain with notched electrodes but only 13.26% strain with rectangular electrodes. When the actuator was scaled to 12 units, it maintained a strain of 17.05% with notched electrodes. The load–strain curves of four-unit actuators based on rectangular and notched electrodes show that notched electrodes are advantageous compared to rectangular electrodes in the low-load region (Figure 4.5d).

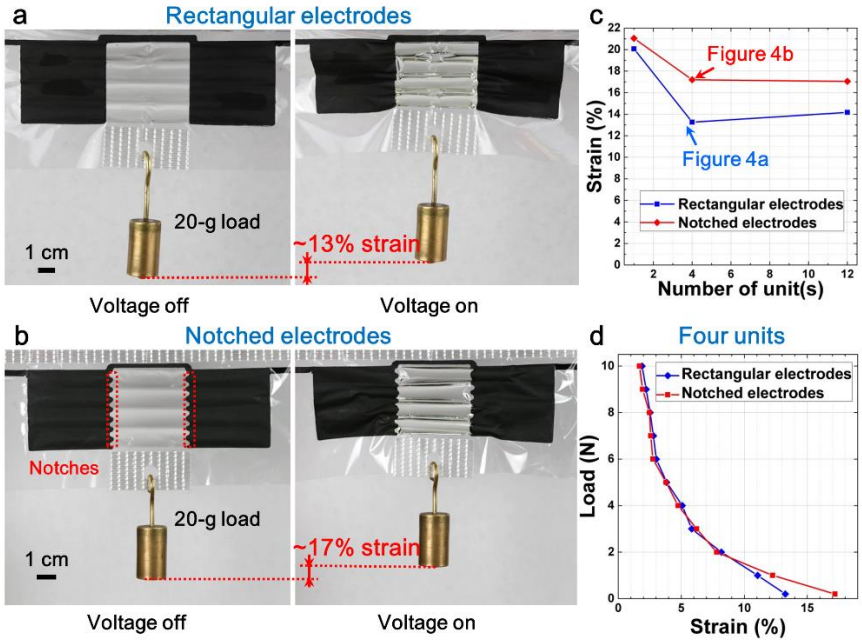

Figure 4.5: Notched electrodes to promote buckling at the transition region between the zipping and contracting regions. (*71*)

4.2.4 HS-Peano-HASEL as an artificial circular muscle (ACM)

Circular muscles play an important role in biological systems. They enable the primordial heart in ascidians to pump; they generate peristalsis in earthworms and digestive tracts, and regulate flow as sphincters (*73–76*). We demonstrated an ACM using a 12-unit HS-Peano-HASEL actuator that was rolled around a silicone rubber tube. Figure 4.6a shows the idealized actuation mechanism, where the length change of the actuator corresponds to a change of the cross-sectional area. At the maximum actuation strain, the area theoretically decreases to ~41% of the initial area. When considering the radial expansion of each of the individual shells, the area of the inscribed circle decreases further. Figure 4.6b shows the actuation behavior of the device. To force the ACM to return to its initial state after an actuation cycle, the silicone rubber tube was pre-pressurized through a check valve with air. The ACM system performed biomimetic pulsed pumping; we demonstrated the pumping behavior by inflating a thin elastic diaphragm made from silicone

(Figure 4.6c). We measured the pressure increase within the chamber when different voltages were applied to the ACM (Figure 4.6d). The chamber was initially pressurized to 1.30 kPa to provide a restoring force and adequate contact between the internal silicone tube and the ACM. The pressure within the chamber increased proportionally to the applied voltage and reached a maximum of 2.73 kPa at 10 kV. Additionally, the ACM was driven by a sinusoidal waveform at various frequencies with an initial pressure of 1.00 kPa (Figure 4.6e). The ACM generated a blocking pressure differential of 0.94 kPa at 1 Hz and 0.84 kPa at 4 Hz. We measured the flow rate of the ACM and found that the peak and average flow rates during contraction were 2.30 L min^{-1} and 1.47 L min^{-1}, when driven by a 4 Hz sinusoidal voltage signal with a 10-kV amplitude, respectively. For these flow rates, the system pressure oscillated between 1.5 and 1.8 kPa above atmosphere.

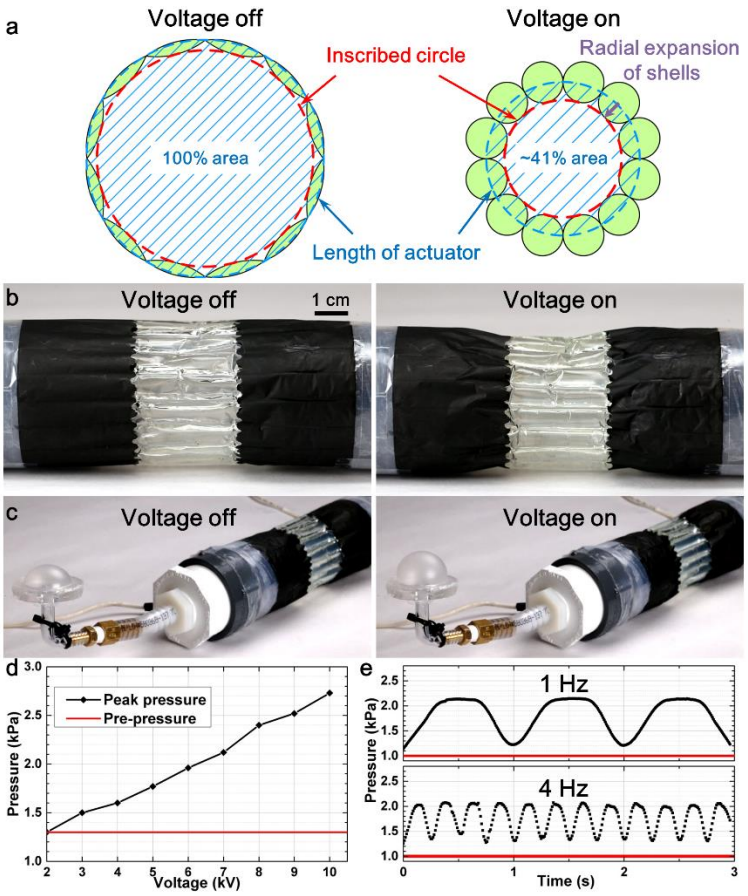

Figure 4.6: An artificial circular muscle based on a HS-Peano-HASEL. (*71*)

4.3 Outlook

In this work, we introduced an electrohydraulically driven, linearly contractile soft actuator which achieved linear strain exceeding 20% (the typical value for skeletal muscle). Specifically, the HS-Peano-HASEL actuator introduced in this paper achieved maximum linear strains of ~24%, exceeding the maximum strain of ~15% of Peano-HASEL actuators. Material and design variations were utilized to improve the stroke of multiunit HS-Peano-HASEL actuators. The demonstration of the ACM highlights potential applications in artificial organs (*77*) and soft pumps. The experimental results for the load-strain behavior follow the trend predicted by the analytical model we developed. The deviation between experimental results and theoretical

predictions is attributed to the constraints at the intersection of the contracting region and the zipping regions, which are neglected in the model and lead to an overestimation of strain.

The actuation mechanism of HS-Peano-HASELs necessitates actuation units with relatively large widths, which will be a drawback for certain applications. On the other hand, when compared to multiunit Peano-HASELs, multiunit HS-Peano- HASELs do not have gaps between electrodes of single units, which simplifies the manufacturing process of the electrodes of multiunit HS-Peano-HASEL actuators. Overall, the ability to achieve muscle-like linear contraction and all-around performance highlights the potential of HS-Peano-HASEL actuators for wide use in future bioinspired robotic systems.

5 A pocket sized 10-channel high voltage power supply

5.1 State of the art

The driving electronics for actuation, computation, and control are an integral aspect of any soft robotic system built using electrostatic devices. This circuitry is particularly important for wearable devices and autonomous soft robots, wherein these machines must carry or support their driving electronics in order to maintain functionality. Towards this endeavor, many examples of driving electronics for electrostatic devices have been established, which vary in architecture, functionality, and cost (*59*, *67*, *78*). Lenz et al. (*78*) built a custom high voltage source to drive DEAs that was capable of outputting voltages up to 3.5 kV in a relatively compact package, while having a bill of materials less than $12. Moreover, custom miniaturized high voltage (HV) driving electronics were developed for remote control of an untethered soft swimming robot driven by DEAs (*35*). Furthermore, an open source high voltage power supply (HVPS) developed by Schlatter et al. (*59*) utilized only off-the-shelf components and has been demonstrated to control soft electrostatic grippers and an active cell stretcher (*60*, *61*). This open source architecture was also the inspiration for the battery-powered circuitry detailed in Chapter 3.

A common strategy to reduce the size and complexity of the driving electronics for soft electrostatic devices is to reduce the driving voltage. Lower voltage operation can be advantageous since there are a plethora of commercially available miniature electronic components operating at a few hundred volts. Operation at a few hundred voltage also enables the use of circuitry developed for the well-established field of piezoelectric devices, and lower voltage operation can placate engineering precautions required to prevent electrical arching to control circuitry and the user.

Recently, Ji et al. (*79*) developed an autonomous soft robotic insect driven by DEAs that operated using voltages below 450 V at frequencies as high as 1 kHz.

However, reducing the operating voltage is not always desirable, specifically for electrohydraulic transducers, such as HASEL actuators and electro-origami (*80*), that have been shown to require voltages in the range of 5-20 kV. Reducing the excitation voltage for HASEL actuators by decreasing the effective thickness of the composite dielectric between the electrodes (i.e. using thinner films for the dielectric shell material) results in less actuation force for a given electric field, dielectric constant of the shell material, and fill volume (*70*, *72*). Furthermore, decreasing the operating voltage of HASEL actuators while maintaining a desired specific energy density requires an increase of the capacitance of the device. Larger capacitance necessitates more charge that can lead to higher charge and discharge currents during high speed operation; in this case, lowering the operating voltage does not inherently make the driving circuitry or the actuator itself safer for the user (*63*).

More complex soft robots require multiple degrees-of-freedom that can be independently addressed for enhance functionality and aptitude. Thus, these machines require power supplies with multiple output channels. Recent advancements in flexible high-voltage thin-film transistors by Marette et al. (*67*) have enabled compliant and embedded high voltage electronics capable of driving an array of 16 DEAs operating at 1 kV. When higher operating voltages ranging from 5-10 kV are desired, the modular multi-channel HVPS demonstrated in Chapter 3 could be utilized. While effective, this modular approach to adding channels to the HVPS necessitated a HV amplifier for each channel, which greatly increases the size and cost of the power supply since the amplifiers are typically the largest and most expensive components on the bill of materials (*53*).

The high voltage power supplies discussed thus far are voltage-controlled; that is, the output voltage of an amplifier is adjusted to a desired level to control the state of the device at its output. If a single power supply is used, independently addressing multiple channels requires a highly dynamic power supply capable of rapidly adjusting its output voltage in real time. Furthermore, voltage-controlled actuation of DEAs can result in undesirable pull-in instabilities leading to dielectric breakdown and catastrophic failure of the dielectric membrane (*48*, *81*, *82*).

A charge-controlled driving scheme was first proposed by Gisby et al. (*83*), wherein a pulse-width modulated (PWM) optocoupler was used as an analog HV switch to control the amount of charge that was supplied to a DEA from a HV source. In this example, the actuator was discharged passively through a voltage divider, which was monitored with the discharging current to infer the capacitance of the actuator; thereby integrating actuation and self-sensing (*83–85*). This technique can be extrapolated to many PWM-controlled optocouplers that distribute power to an equal number of outputs from a single HV amplifier (*86*, *87*). Furthermore, alternative switching elements, such as MOSFETS and IGBTs, have been shown to achieve the desired PWM high voltage signal to drive electrostatic actuators (*87*, *88*), though optocouplers remain the most compact solution for switching voltages higher than 5 kV. However, off-the-shelf optocouplers (such as the commonly used OC100HG from Voltage Multipliers Inc.) have limitations; namely, the maximum HV current that can pass through the optical diode is restricted to around 300 µA (from the datasheet provided by the company), which limits the dynamic performance of electrostatic devices having a relatively large capacitive load (on the order of 10s of nF and greater).

While the charge-controlled driving scheme described above laid the framework for independent control of many electrostatic actuators, there are drawbacks to the described method.

A passive resistor as a constant discharge path for the actuators limits the dynamic response of the actuators by fixing the RC time to discharge. Therefore, maximum and minimum rate of discharge and the bandwidth of the actuators is restricted. Moreover, a fixed resistor in parallel with the actuator establishes a load dependent discharge response; actuators having different capacitances will discharged at different rates across the resistor. Importantly, a continuous discharge path negates the inherent advantages of catch states attributed to electrostatic actuators (*89*). In this case, the actuator must continuously draw current from the HV amplifier to hold a position, resulting in a parasitic load on the amplifier that is particularly inefficient when scaling up to many output channels (which is a key benefit of the charge-controlled technique).

5.2 Contributions to expand the state of the art

This work aims to fill the gap in literature pertaining to portable high voltage driving electronics that can address many (10s) of channels to voltages up to 10 kV, while preserving the inherent low-energy consumption of the electrostatic actuators. We created a battery powered, pocket-sized HVPS that can independently and simultaneously address 10 outputs to voltages ranging from 2-10 kV. Each channel of the HVPS consists of two custom-made PWM-controlled optocouplers oriented in a half bridge configuration, such that one optocoupler charges the output and the other discharges the output. This architecture enables active control over both the charging and discharging portions of an actuation cycle, thereby accessing the inherently large dynamic range of the actuators as well as their catch states.

The power supply measures only 8.4 cm long, 13.3 cm wide, and 2 cm thick, and weighs 250 g including the batteries. These specifications are nearly identical to those of a standard smart phone, which allows the power supply to fit in a men's jean pocket. This low profile is attributed

to the custom optocouplers that weight only 1.2 g and have a total volume of 240 mm^3, which is nearly 10 times smaller than commonly used off-the-shelf optocouplers (such as OC100HG from Voltage Multipliers Inc). Additionally, these optocouplers were shown to switch voltages as high as 10 kV while conducting current in the milliamp range. We characterized the charge-control capabilities of the power supply when driving HASEL actuators and measured key performance metrics of the actuators when activated by the supply. Finally, we develop a soft robotic inchworm to highlight the ability of the HVPS to independently address organized groups of actuators with undulatory action sequences.

5.2.1 A pocket-sized 10-channel HVPS

The pocket-sized 10-channel HVPS can be seen in Figure 5.1a. Starting from the bottom right-hand corner of Figure 5.1a and moving clockwise, the labeled components are as follows:

- A Teensy 4.0 (PJRC) microcontroller was used to control the circuit board.
- Two 3.7 V LiPo batteries (YDL2018032941, YDL) in series provided input power to the circuit when the primary power switch was engaged.
- The 7.4 V from the batteries was stepped down to 5 V using a Pololu 5 V, 2.5 A regulator (D24V50F5, Pololu), which provided the necessary voltage and current to drive the circuit under any operating conditions.
- A buck converter provided controllable input power to the HV amplifier (5VV10P, Pico Electronics). For safety, a HV kill switch was utilized to cut power from the buck converter and therefore the HV amplifier.

- A voltage divider was utilized to generate a low voltage replica of the HV output, which was monitored to load regulate the output of the HV amplifier using a PID controller (Arduino PID Library).
- The output of the HV amplifier was connected to a HV rail that distributed power to each of 10 discrete channels.

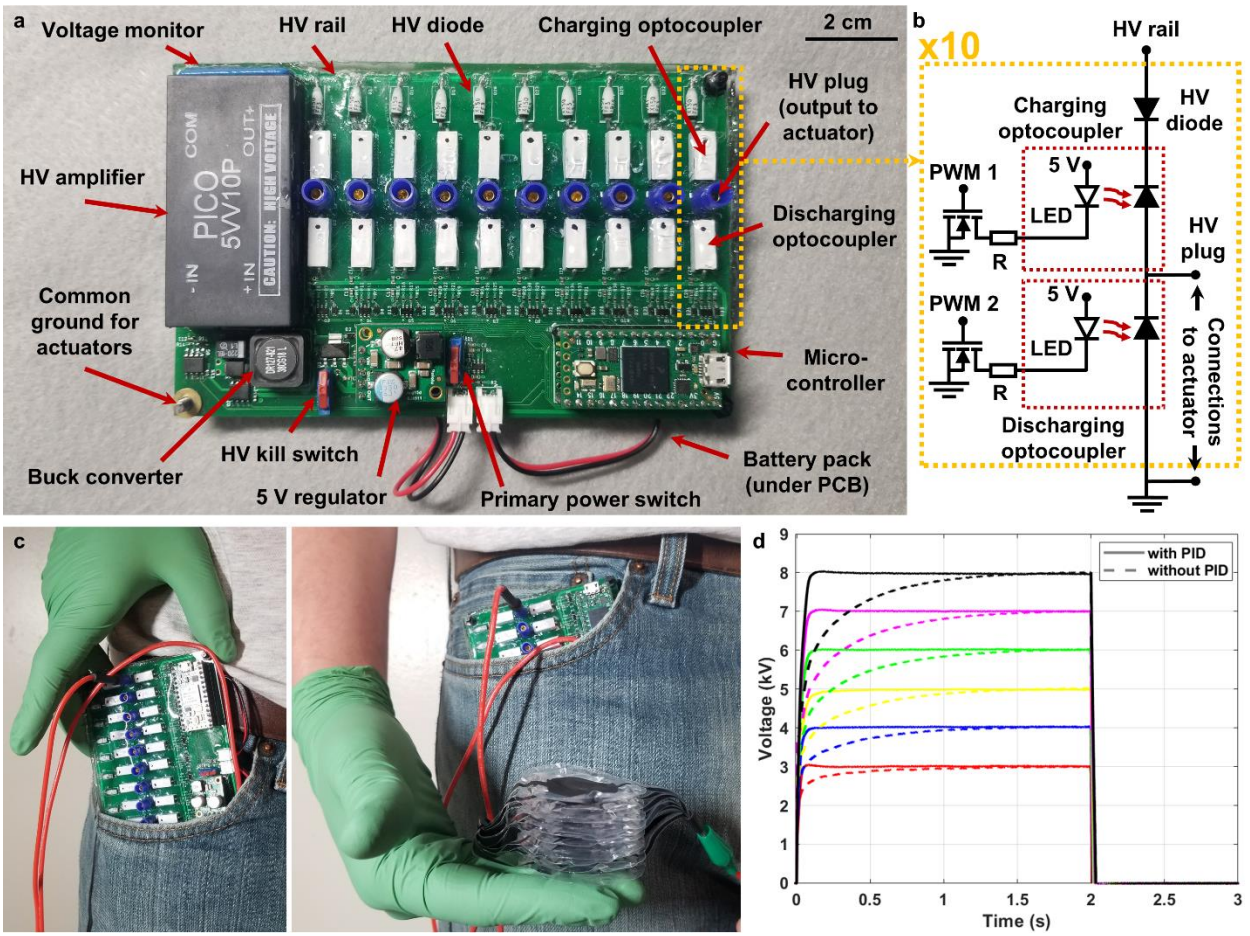

Figure 5.1: A pocket-sized 10-channel HVPS. a) A top view of the power supply, which measures 8.4 cm long, 13.3 cm wide, and 2 cm tall, and weighs only 250 g including the batteries. b) An electrical schematic of one channel. c) The compact power supply is about the size of a smart phone and can be used to power a HASEL actuator while stored within a jean pocket. d) The voltage as a function of time across a HASEL actuator connected to one channel of the power supply.

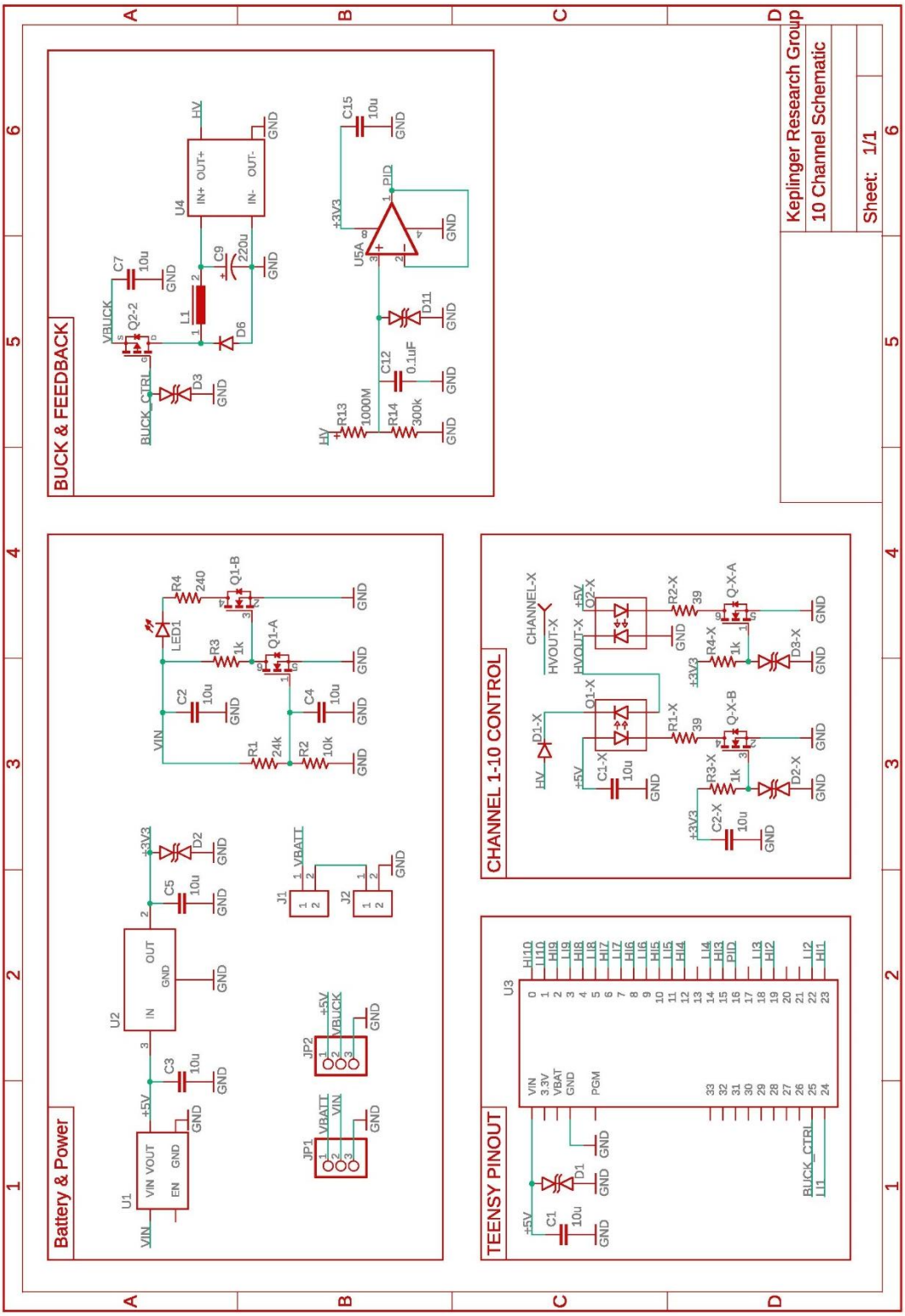

Figure 5.2: The complete electrical schematic for the 10-channel HVPS.

Qty	Parts	Description	Device Part Number
1	C9	220 µF capacitor	TR3E227K016C0150
1	D4	diode for buck converter	STPS2L40U
1	LED1	Red LED	SML-512UWT86
1	C12	0.1 µF capacitor	C0402C104Z4VAC7867
27	C1-C11, C13-C29	10 µF capacitor	C0402C106M9PAC7867
1	R13	1 GΩ resistor for voltage feedback	OHMITE104E
1	R4	240 kΩ resistor	ERJ-PA2F2400X
21	R3, R5, R6, R9, R10, R15, R16, R19, R20, R23, R24, R27, R28, R31, R32, R35, R36, R39, R40, R43, R44	1 kΩ resistor	ERJ-PA2F1001X
1	R2	10 kΩ resistor	ERJ-PA2F1002X
1	R1	24 kΩ resistor	ERJ-PA2F2402X
1	R14	300 kΩ resistor	ERJ-PA2F3003X
20	R7, R8, R11, R12, R17, R18, R21, R22, R25, R26, R29, R30, R33, R34, R37, R38, R41, R42, R45, R46	39 Ω resistor	ERJ-PA2F3900X
1	U1	5 V regulator	D24V50F5
1	L1	10 µH inductor	DR127-100-R
1	Q2	N/P dual MOSFET	FDS8858CZ
1	U2	3.3 V regulator	LD1117S33TR
1	U4	HV amplifier	PICO-5VV10
1	U3	Teensy 4.0	TEENSY40
1	IC1	OPAMP for voltage feedback	TLC272BCDR
2	J1, J2	JST connector - female	S2B-PH-K-S(LF)(SN)
10	CHANNEL1 - CHANNEL10	3 mm circular pad for HV plugs	3MM_PAD
10	D5, D8, D11, D14, D17, D20, D23, D26, D29, D32	HV diodes	X150FF3
11	Q1, Q3-Q12	Dual N-channel MOSFET	NDC7002N
20	D2, D3, D6, D7, D9, D10, D12, D13, D15, D16, D18, D19, D21, D22, D24, D25, D27, D28, D30, D31	3.3 V TVS diode	SP4020-01FTG-C
20	O1 O20	Optical diode	OZ100SG
20	O1-O20	IR LED	L1IZ-0940000000000
1	D1	TVS DIODE 5V 12V	GG040205100N2P

Table 5.1: A list of the electrical components used for the 10-channel HVPS.

Figure 5.2 shows the complete electrical schematic and the corresponding components are listed in Table 5.1. Figure 5.1b shows an electrical schematic of one channel, which was replicated 10 times on the circuit board. Each channel consisted of a HV diode, a charging optocoupler, a HV plug for quick connections to the outputs, a discharging optocoupler, and the associated MOSFET switching elements to control the optocouplers. The HV diode prevented current from flowing between the outputs of channels at different electrical potentials. The optocouplers were custom built using an optical diode (OZ100SG, Voltage Multipliers Inc.) and a miniature IR LED (L1IZ-0940000000000, Lumileds), Figure 5.3a. The anode of each LED was connected to the 5 V output of the Pololu regulator while the cathodes were each connected to the drain pin of separate N-channel enhancement mode MOSFETs (NDC7002N, ON Semiconductor) through a current limiting resistor, *R*. The source of each MOSFET was connected to ground, while the gate pins were each connected to a separate PWM output of the microcontroller. Custom HV plugs were designed to allow easy plug-and-play connections to the HV outputs of each channel, and each actuator at the outputs shared a common ground. Figure 5.3 details the construction and encapsulation of the circuit. The completed circuit board including the battery pack is compact enough to fit in a jean pocket while still powering an actuator, Figure 5.1c. This demonstration was conducted without concern of electrostatic discharge due to the HV insulation that encapsulates the PCB, and the fact that the actuator has a fixed low potential (i.e. ground) electrode which shielded the HV electrode from the user.

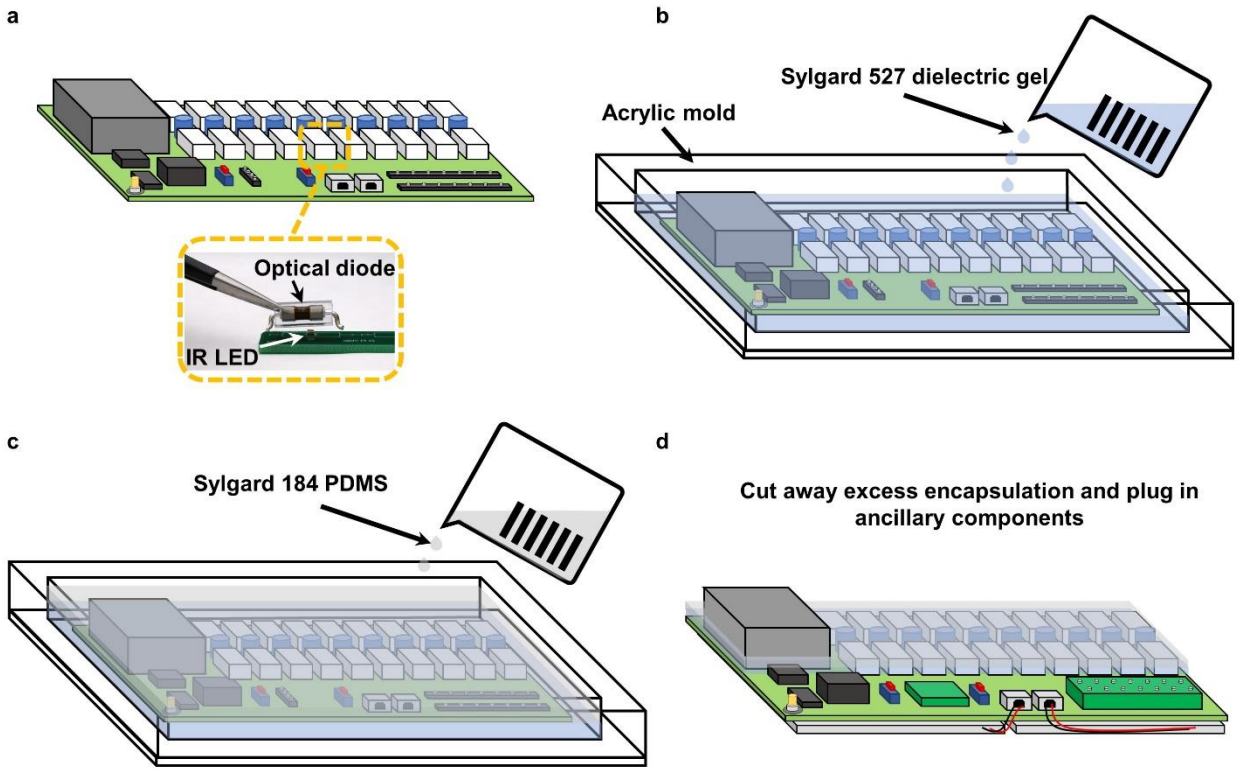

Figure 5.3: Construction of the 10-channel HVPS. a) Components were soldered onto the PCB. The custom optocouplers were constructed by placing the optical diode directly on top of the IR LED and soldering in place. b) An acrylic mold was used to encapsulate the PCB with dielectric gel (Sylgard 527, Dow Corning). c) The gel is extremely tacky in its cured state, so a polydimethylsiloxane (PDMS) silicone elastomer was used to coat the gel to prevent the PCB from sticking surfaces. d) The excess encapsulation was cut away and the ancillary components (microcontroller, 5 V regulator, and batteries) were plugged into the PCB.

Figure 5.1d shows the characteristic voltage profiles at the output of one channel when driving a stack of 10 donut HASEL actuators (maximum capacitance of ~5 nF) to discrete voltage steps ranging from 3-8 kV at 1 kV increments. These voltage steps were achieved by adjusting the input to the HV amplifier using the buck converter as demonstrated in Chapter 3. Figure 5.1d shows that the PID controller greatly improves the voltage rise. Specifically, the rise time to 8 kV was ~100 ms with the PID controller as opposed to nearly 1.5 s without the controller. Ultimately, however, the rise time of the voltage at an output is dependent on the load and the driving

frequency. Figure 5.4 shows the voltage response at an output under various capacitive loads (i.e. number of HASEL actuators) and actuation frequencies.

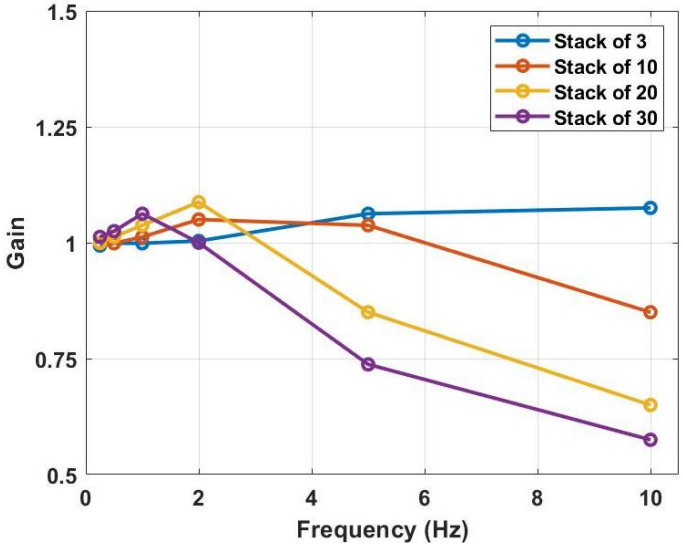

Figure 5.4: Frequency response of one channel of the HVPS when driving different capacitive loads. A gain of 1 corresponds to a voltage of 8 kV.

5.2.2 Basic principles of the charge-controlled driving scheme

Each of the 10-channels can provide a controllable high voltage output by adjusting the HV output of the amplifier (as seen in Figure 5.1d) or by controlling the conductance of the optocouplers using PWM-controlled IR LEDs. This latter technique provides a method of controlling the amount of charge stored by the electrostatic device in any point in time; that is, the slew rate and amplitude of the HV output to the electrostatic device can be modified by controlling the duty cycle and duration of the low-voltage PWM signal to the optocoupler. This technique was implemented on both the charging and discharging optocouplers for analog control of the overall charge stored by the HASEL actuator, and thus, its physical state. Furthermore, this technique enables simultaneous and distributed control over multiple outputs while utilizing only one centralized HV amplifier.

The electrical power to a HASEL actuator was analyzed when driven by the charge control scheme described above. The experimental setup can be seen in Figure 5.5a, which details one channel of the HVPS driving a stack of 10 donut HASEL actuators with a maximum capacitance of ~5 nF. A contactless electrostatic voltmeter (Model 341B, Trek) was used to monitor the voltage at the output of the channel, while a measurement resistor on the ground side of the actuator provided information about current to and from the actuator. Peak current through the optocouplers as a function of the duty cycle of the PWM signal to LEDs is displayed in Figure 5.5b. This data shows an approximate linear relationship for both charging and discharging, with higher duty cycle corresponding to higher peak current and vice versa. At duty cycles higher than 10%, the magnitude of peak current is higher for discharging than charging. This effect is due to the fact that the charging path has a higher impedance than the discharging path; that is, the charging current depends on the impedance of the HV amplifier, the charging optocoupler, the load at the output (i.e. actuator), as well as leakage current through the discharging optocoupler, while the discharging current is determined only by the impedance of the discharging optocoupler and the load.

Characteristic voltage and current profiles at different PWM duty cycles is shown in Figure 5.5c,d. At 100% duty cycle, a voltage rise to 8 kV took only 100 ms and corresponded to a peak charging current of over 1.1 mA. While a duty cycle of only 2% extended the rise time to 1.7 s and capped the peak charging current to only 30 µA. A similar response can be seen during the discharging portion of the cycle. At 100% duty cycle, the discharging optocoupler enabled a fast discharge from 8 kV to 0 kV in less than 50 ms, which corresponded to 1.5 mA. At 2% duty cycle, the discharge time was slightly less than 1.5 s, with the peak discharging current limited to 30 µA.

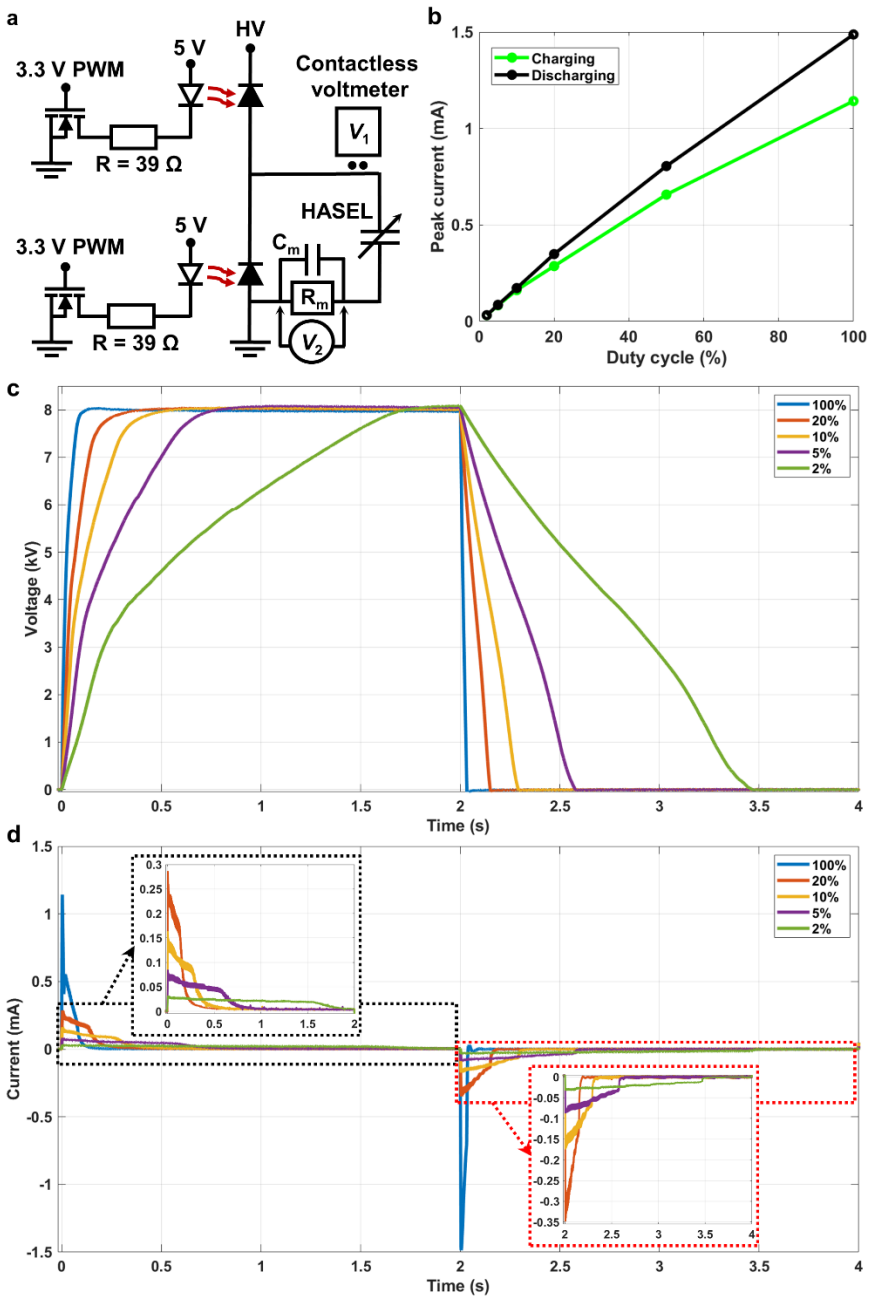

Figure 5.5: Basic principles of the charge-controlled driving scheme. a) The experimental setup used to measure the electrical characteristics of a HASEL actuator connected to one channel of the HVPS. b). The peak HV current through the charging and discharging optocouplers as a function of the duty cycle of the PWM signal applied to the low voltage IR LED of each optocoupler. c) The charging and discharging voltage and d) current profiles of a HASEL actuator at different PWM duty cycles applied to the LEDs.

The custom optocouplers developed in this work shift the current limitations from the switching elements to the HV amplifier. The Pico HV amplifier is limited to about 5 W, which is evident in Figure 5.5c,d where the ~1.1 mA peak charging current is achieved as the actuator reaches ~5 kV. If the HV amplifier can deliver higher power, the maximum HV current through optocouplers at 100% duty cycle can be increased by lowering the resistor value in series with the LED. To analyze the current limitations of the custom optocouplers, a test PCB was designed to easily adjust the HV source and the resistor (on the back side of the PCB schematic in Figure 5.6a) in series with the LED, Figure 5.6.

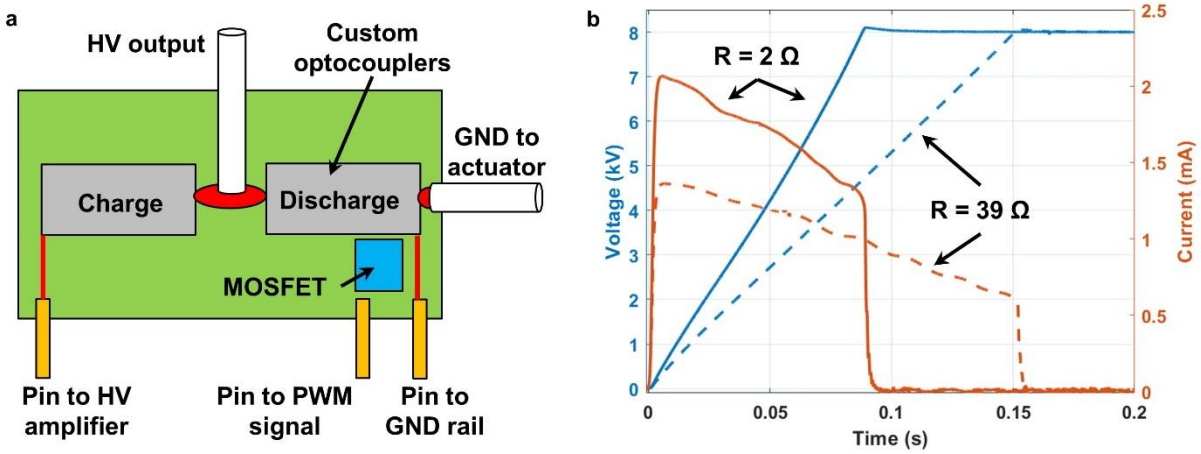

Figure 5.6: Testing the current limitations of the custom optocouplers. a) An illustration of a PCB that was designed to adjust the HV input and current limiting resistor in series with the IR LED. b) Charging voltage and current as a function of time for a 16.5 nF ceramic capacitor.

To standardize these tests, a ceramic capacitor with a fixed capacitance of 16.5 nF was used as the output load. A Trek HV amplifier (Model 5012) was used as the HV source and the PWM signals to the LEDs were generated by a function generator (33500B, Keysight), set to a frequency of 5 kHz and a duty cycle of 99.99%. The charging current and voltage profiles for the capacitor are shown in Figure 5.6b. The solid curves show the profiles when a 2 Ω resistor was in series with the LEDs and the dashed curves show the profiles with a 39 Ω resistor. A peak charging

current of 2.1 mA was achieved with the 2 Ω resistor as compared to only 1.4 mA with the 39 Ω resistor. Even smaller resistors can be used in series with the LEDS to further increase the peak current through the optocouplers, though heat dissipation will need to be considered for the LEDs to ensure long term functionality.

5.2.3 Independent control of HASEL actuators using the 10-channel HVPS

To highlight the capability of the 10-channel HVPS to independently drive capacitive loads such as HASEL actuators, Figure 5.7a shows three stacks of 10 donut HASEL actuators each driven by unique waveforms generated by the HVPS. The left-most actuator operated at 0.25 Hz by gradually charging to 8 kV and then discharging to 0 kV using a PWM signal with a duty cycle of 10%. The center actuator operated at 1 Hz and demonstrated an asymmetric charging and discharging rate when driven abruptly to 8 kV with a 100% duty cycle but then discharged more slowly with a 20% duty cycle. Finally, the right-most actuator operated at 10 Hz with 100% duty cycle to charge and discharge. The right image in Figure 5.7a shows a snapshot of the actuators operating at the above specifications, wherein the left actuator was partially charged to ~5 kV, the middle actuator was fully charged at 8 kV, and the right actuator was blurred as it rapidly actuated at 10 Hz.

Furthermore, the output of each channel can be programmed to achieve nearly arbitrary charging and discharging voltage profiles. An 2x5 array of actuators was used to showcase the multitude of actuation profiles that can be achieved, Figure 5.7b. Each stack in the array consisted of four donut HASEL actuators electrically connected in parallel. The stacks were designed with an even number of actuators to ensured that the exposed electrodes on the top and bottom of the stack were connected to the low potential, therefore mitigating the risk of electrostatic discharge

to objects above or below the array. The array was used to create a myriad of patterns, as exemplified in Figure 5.7b. The array also exhibited fast cyclic actuation as well as independent control over the actuation frequency of each stack.

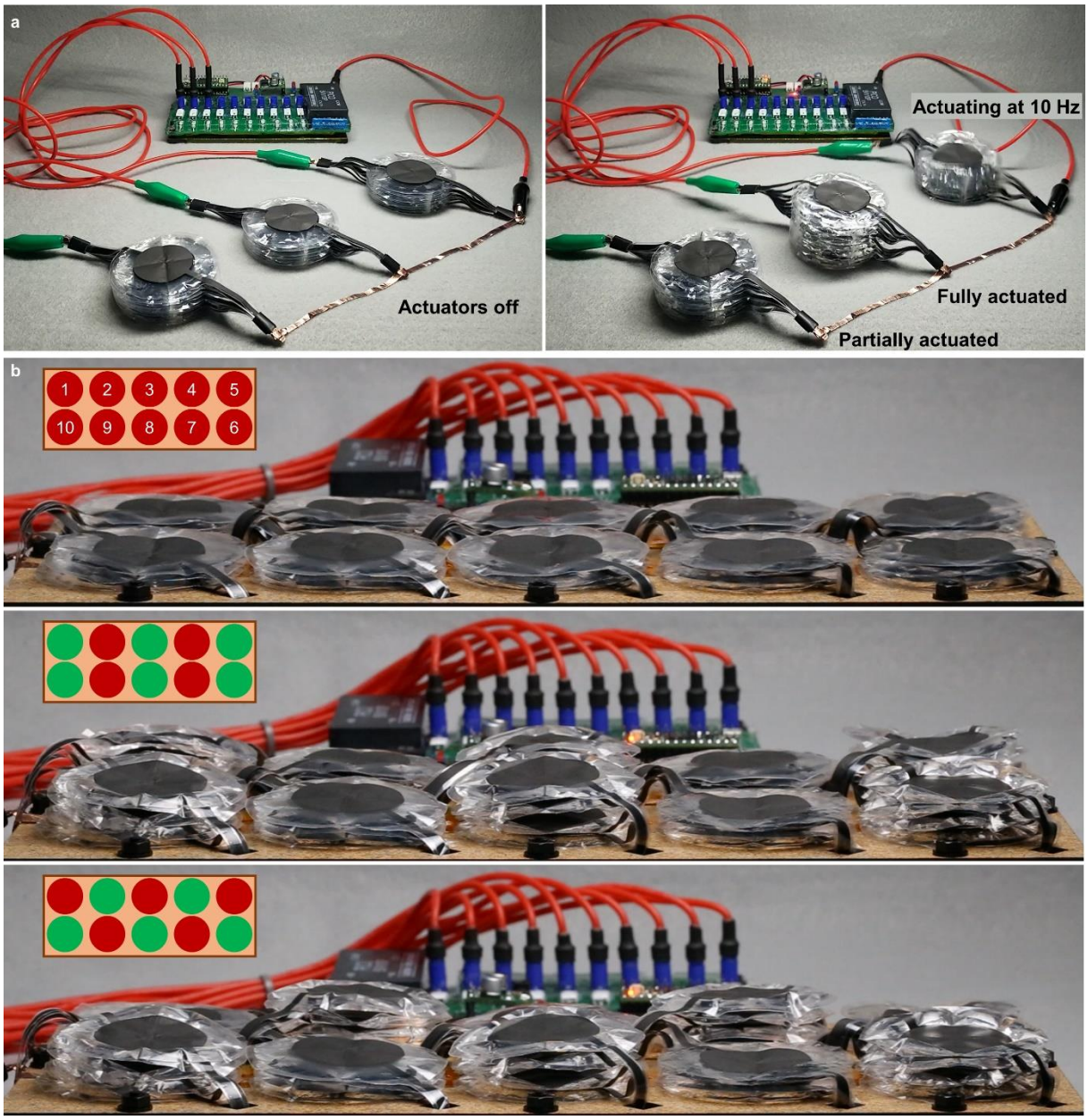

Figure 5.7: Independent control of systems of HASEL actuators using the 10-channel HVPS. a) Demonstration of three stacks of 10 actuators operating at different driving conditions. b) A 2x5 array of HASEL actuators driven by the 10-channel HVPS. Each actuator in the array was independently addressed to achieve a multitude of patterns.

5.2.4 Baseline performance of HASEL actuators when driven by the HVPS

To better understand the influence of the driving electronics on the mechanical output of HASEL actuators, we analyzed the performance of the donut HASEL actuators seen in the previous section. These specific actuators were tested since similar devices have demonstrated the ability to lift their driving electronics (Figure 3.14 in Section 3.2.7). It is important to note that the dynamic performance of the actuators when driven by the HVPS is ultimately limited by the power output of the HV amplifier (5 W), and so the maximum capacitance of the actuators tested will influence the results. Therefore, the results shown here do not represent the pinnacle of actuator performance, but rather a baseline performance for these actuators when driven by the HVPS.

The actuators were constructed using the techniques established in the first half of Chapter 3. They consisted of a 20-µm-thick polyethylene terephthalate (PEL0WS, Multi-Plastics) thin film as the dielectric shell, a low viscosity silicone oil (5 cSt, 317667-1L MKCG6784 Sigma Aldrich) for the liquid dielectric, and screen-printed carbon ink (CI-2051, Engineered Materials Systems) as the electrodes. Each actuator had a maximum capacitance of ~500 pF, which was measured with an LCR meter (BK 886, BK Precision) by manually pressing the electrodes together using an insulating acrylic disc to simulate the fully activated state of the actuator.

Figure 5.8a depicts the experimental setup to test the performance of the HASEL actuators when driven by the power supply. An artificial muscle tester (310-LR, Aurora Scientific 3000) was controlled using a DAQ and a custom LabVIEW program. The lever arm of the muscle tester was attached to an acrylic platform that exerted a compressive load on the actuators, which were driven by one channel of the HVPS. The HV rail of the power supply was set to 8 kV and the optocouplers were operated at 100% duty cycle to charge and discharge the actuators.

The stack of three and stack of 10 actuators demonstrate similar load-strain behavior, Figure 5.8b, with a no-load strain of 120% and blocked force around 20 N. Figure 5.8c,d show that a stack of three actuators has a peak strain rate of nearly 4000% s^{-1} and a peak specific power of almost 50 W kg^{-1}. While the stack of 10 actuators only achieved 1,750% s^{-1} and ~15 W kg^{-1}. The calculation for specific power was based on the weight of the actuator only. The deviation in dynamic performance from a stack of three actuators to a stack of 10 is attributed to the limited power output from the HVPS, since both stacks have similar load-strain characteristics.

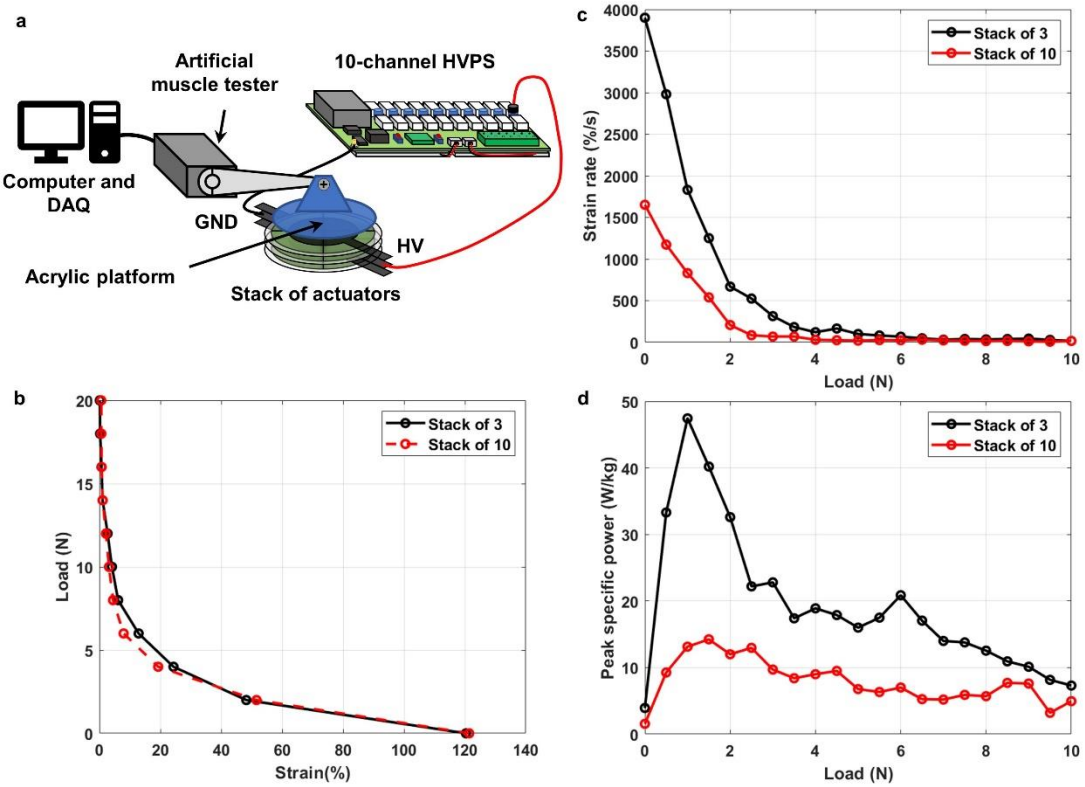

Figure 5.8: Baseline performance of HASEL actuators when driven by the HVPS. All experiments were conducted at 8 kV with the optocouplers operating at 100% duty cycle. a) The experimental setup. b) Load vs strain curves, c) strain rate vs load, and d) peak specific power for a stack of three and a stack of 10 actuators.

5.2.5 A soft robotic inchworm powered by the 10-channel HVPS

Many species of animals, both terrestrial and aquatic, locomote through coordinated undulations within their bodies or extremities. For example, earthworms generate peristaltic

locomotion through coordinated extension, anchoring, and relaxation of sections of their bodies (*74*), while black ghost knifefish generate wave-like propagations in their highly flexible ribbon-like anal fin to achieve omnidirectionally swimming (*90*, *91*). In either case, independent control and coordination of groups of muscles is critical.

We constructed a soft robotic inchworm to demonstrate organized and distributed actuation of independent groups of HASEL actuators using the 10-channel HVPS, Figure 5.9. This inchworm consisted of 10 stacks of 8 actuators, with adjacent stacks separated by a thin acrylic spacer for structural support. Each acrylic spacer had slots to feed the HV transmission lines of the power supply to each stack. One lead of each stack was connected to an independent channel of the HVPS, while the other lead of each stack was connected to a common ground. The entire robot was wrapped in a sheet of 300-μm-thick silicone elastomer (Ecoflex 00-10, Reynolds Advanced Materials), which was stretched uniaxially to two times its original width. This elastomer provided an elastic restoring force to assist the actuators to their initial state when discharged. Each acrylic divider had two ‘feet’ that protruded from the silicone membrane and were covered with anisotropic friction in the form of ski-skins (Nordica). The ski-skins consisted of directional fibers that ensured the deformation of the actuators would propel the robot forward, Figure 5.9a.

An undulatory actuation sequence was generated by the HVPS and propagated through the body of the robot to drive locomotion, Figure 5.9b. At t_0 = 0 s, stacks 1 and 6 activated simultaneously (while stacks 5 and 10 are discharged from the previous actuation sequence). Next, at $t_1 = t_0 + \Delta t$, stacks 1 and 6 are discharged while simultaneously stacks 2 and 7 are charged. Then, at $t_2 = t_1 + \Delta t$, stacks 2 and 7 are discharged while simultaneously stacks 3 and 8 are charged. Subsequently, at $t_3 = t_2 + \Delta t$, stacks 3 and 8 are discharged while simultaneously stacks 4 and 9 are charged. Finally, at $t_4 = t_3 + \Delta t$, stacks 4 and 9 are discharged while simultaneously stacks 5 and 10

are charged. After t_4, the actuation sequence repeats starting with t_0. This undulating actuation pattern enable the robot to crawl on a flat paper substrate, Figure 5.9c. The actuation voltage for each stack was 8 kV and the charging optocouplers were excited with a PWM signal at 100% duty cycle. Each stack was discharged more slowly by exciting the discharge optocoupler with a PWM signal at 10% duty cycle. A slower discharge time was preferred since it was observed that an abrupt discharge would increase the likelihood of slippage between the anisotropic friction and the paper substrate. With a time step of Δt = 100 ms between the sequences shown in Figure 5.9b, the robot traversed 29.5 cm in 20 s, which corresponded to a movement speed of 4.6 body lengths per minute. Figure 5.9d displays the robot traveling up a 10˚ incline. In this case, the actuation sequence varied from Figure 5.9b in that only one stack of actuators was activated during each time step (and thus twice as many time steps as the sequence shown in Figure 5.9b were used). In this case, the robot traveled 17.6 cm up the incline in 20 s.

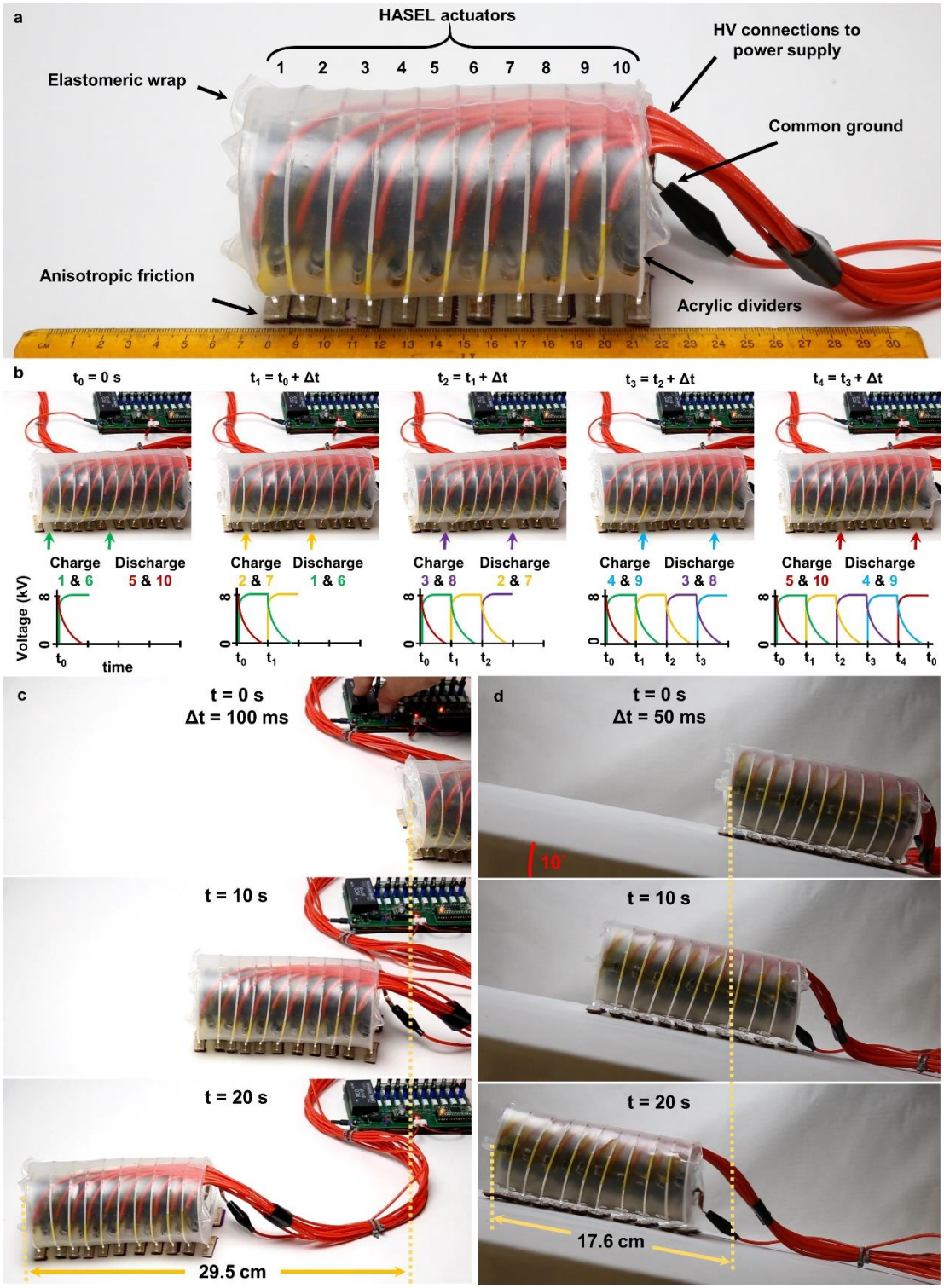

Figure 5.9: A soft robotic inchworm driven by undulatory actuation sequences generated by the 10-channel HVPS. a) The inchworm consisted of 10 stacks of 8 quadrant donut HASEL actuators, each separated by an acrylic divider. The device was wrapped in a silicone elastomer to provide an elastic restoring force. Ski skins were used as anisotropic friction on the feet of the robot to ensure directional locomotion. b) An example of an undulatory actuation sequence wherein two stacks were simultaneously charged while two stacks were discharged during each time step.

Stacks 1 and 6 are represented by green, 2 and 7 are yellow, 3 and 8 are purple, 4 and 9 are blue, and 5 and 10 are red. c) Using an activation voltage of 8 kV and a time step of 100 ms, the inchworm traveled 29.5 cm on a flat paper substrate in 20 s. d) When the paper substrate was tilted at a 10˚ incline, the robot could travel 17.6 cm up the paper substrate in 20 s.

5.3 Outlook

The 10-channel HVPS developed here lays the foundation for compact driving electronics that power HASEL-driven soft robots with many degrees of freedom. The charge-controlled activation scheme provides a straightforward method of independently addressing groups of actuators while utilizing only one HV amplifier. Thus, the electrical power output to the actuators is primarily limited by the amplifier and applications that require higher bandwidth actuators will need to balance tradeoffs between the power output and size of the amplifier. Although, a larger and higher power amplifier may be ideal if its power is distributed to hundreds or thousands of actuators using the charge-control scheme developed here or an alternative control method such as matrix addressing (*92*).

The HVPS presented here provides only open-loop control of HASEL actuators. The realization of functional and untethered HASEL-based robots will require driving electronics that also sense the deformation of the actuators to enable closed-loop position or force control. HASELs may offer intrinsic advantages in this regard as circuitry that monitors the capacitance of the actuators can be implemented for closed-loop control (*28, 93, 94*). Furthermore, these untethered robots will require a mechatronic structure that integrates the rigid electronics with the compliant actuators (a clear limitation of the soft robotic inchworm, which was only intended to convey the ability of the 10-channel HVPS to stimulate undulatory locomotion).

5.3.1 HV safety

High voltage safety must be considered for HASEL actuators and their driving electronics. Important metrics to consider are the capacitance of the actuators, the driving voltage, the charging and discharging currents, the duration of exposure during discharge, as well as the equivalent series resistance of the system (actuators, power supply, and the human body) (*63*).

As an example, consider the case where an actuator is charged, disconnected from the power supply, and then accidentally discharged through contact with a human hand. This example was presented by Pourazadi et al. (*63*) regarding DEAs, but the analysis can be extended to HASEL actuators without loss of generality because the two actuator technologies can be modeled as identical equivalent circuits. The equivalent electrical circuit for a HASEL actuator can be seen in Figure 5.10, where C_{HASEL} is the variable capacitance of the actuator, R_{ESR} is the equivalent series resistance of the electrodes of the actuator, R_{p} is the resistance due to leakage current through the composite dielectric, and R_{human} is the resistance of the human body during the discharge event. For this example, C_{HASEL}, R_{ESR}, R_{p}, and R_{human} are constant during the discharge event, and C_{HASEL} is at its maximum value. Then the time constant for the discharge can be written as

$$\tau_1 = R_{\mathrm{EQV}} * C_{\mathrm{HASEL}}, \tag{5.1}$$

where R_{EQV} is the equivalent resistance of R_{ESR}, R_{p}, and R_{human}. Since the series combination of R_{ESR} and R_{human} is in parallel with R_{p}, R_{EQV} can be written as

$$R_{\mathrm{EQV}} = \frac{R_{\mathrm{p}}(R_{\mathrm{ESR}}+R_{\mathrm{human}})}{R_{\mathrm{ESR}}+R_{\mathrm{human}}+R_{\mathrm{p}}}. \tag{5.2}$$

Then Equation 5.1 becomes

$$\tau_1 = \frac{R_{\mathrm{p}}(R_{\mathrm{ESR}}+R_{\mathrm{human}})}{R_{\mathrm{ESR}}+R_{\mathrm{human}}+R_{\mathrm{p}}} * C_{\mathrm{HASEL}}. \tag{5.3}$$

Furthermore, the discharge current to the human from the HASEL as a function of time, *t*, can be written as

$$I_{\text{human}}(t) = I_{\text{HASEL}}(t) - I_{\text{p}}(t), \tag{5.4}$$

where $I_{\text{p}}(t)$ is the leakage current through the composite dielectric and $I_{\text{human}}(t)$ is the current flowing through the human. The voltage profile for the discharging actuator as a function of time is,

$$V(t) = V_0 \text{e}^{\frac{-t}{\tau}}, \tag{5.5}$$

where V_0 is the magnitude of the voltage at the initial time of discharge. Invoking Ohm's Law and substituting Equation 5.5 into Equation 5.4 yields

$$I_{\text{human}}(t) = I_{\text{HASEL}}(t) - I_{\text{p}}(t) \tag{5.6}$$

$$I_{\text{human}}(t) = \frac{V_{\text{HASEL}}(t)}{R_{\text{EQV}}} - \frac{V_{\text{HASEL}}(t)}{\text{R}_{\text{p}}} \tag{5.7}$$

$$I_{\text{human}}(t) = \frac{V_0 \text{e}^{\frac{-t}{\tau_1}}}{R_{\text{EQV}}} - \frac{V_0 \text{e}^{\frac{-t}{\tau_1}}}{R_{\text{p}}}. \tag{5.8}$$

Substituting Equation 5.2 into 5.8 and simplifying the expression yields

$$I_{\text{human}}(t) = \frac{V_0 \text{e}^{\frac{-t}{\tau_1}}}{R_{\text{ESR}} + R_{\text{human}}}. \tag{5.9}$$

Generally, the leakage current through the HASEL is small. If this current is neglected, then Equation 5.3 simplifies to

$$\tau_2 = (R_{\text{ESR}} + R_{\text{human}}) * C_{\text{HASEL}}, \tag{5.10}$$

and the discharge current to the human body is

$$I_{\text{human}}(t) = I_{\text{HASEL}}(t) = \frac{V_0 \text{e}^{\frac{-t}{\tau_2}}}{R_{\text{ESR}} + R_{\text{human}}}. \tag{5.11}$$

While equations 5.9 and 5.11 look similar, note that $\tau_1 < \tau_2$ since the addition of the parallel resistance in the form of leakage current provides another discharge path for the actuator. Therefore, the current across the human body in Equation 5.11 decays more quickly than in

Equation 5.9. So, the scenario where the leakage current is ignored presents a more hazardous condition and will be considered throughout the remainder of this example.

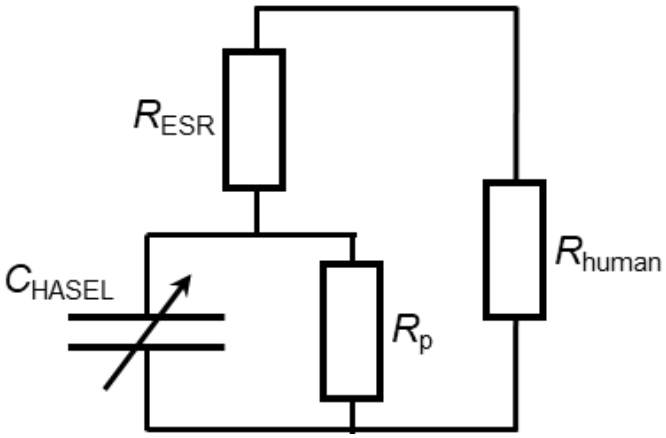

Figure 5.10: The equivalent electrical circuit of a HASEL actuator when discharged by human contact.

To gauge the safety of the actuators, consider the UL (Underwriters Laboratory) and IEC (International Electrotechnical Commission) safety rating for current and duration of exposure (Figure 5.11). The area underneath the curves represents a conservative estimate for safe exposures to DC and AC, assuming the frequency of the current is less than 100 Hz (*95–97*). The rest of the calculations strive to meet the UL criteria, because they are more stringent.

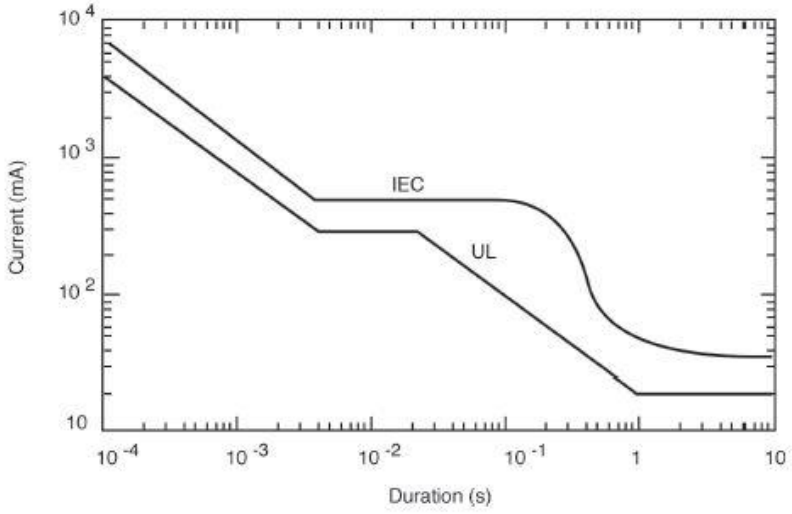

Figure 5.11: The UL and IEC safety standards of current magnitude and duration of exposure. The region below the curves is deemed non-life threatening. Reproduces from (*63*).

The UL standards curve in Figure 5.11 can be broken into a piecewise function described by Pourazadi et al. (*63*):

$$I_{\mathrm{UL}}(t) = \begin{cases} 52 * 10^{-4} * t^{-0.72} \text{ for } 10^{-6} \leq t < 4 * 10^{-3} \\ 28 * 10^{-2} \text{ for } 4 * 10^{-3} \leq t \leq 2 * 10^{-2} \\ 2 * 10^{-2} * t^{-0.67} \text{ for } 2 * 10^{-2} < t < 1 \\ 2 * 10^{-2} \text{ for } 1 \leq t \end{cases} . \tag{5.12}$$

Based on Equations 5.10 and 5.11, if V_0, R_{human}, and R_{ESR} are defined, then the discharge current is governed by the capacitance of the HASEL actuator. Therefore, there is a critical capacitance value below which ensures $I_{\mathrm{human}}(t) \leq I_{\mathrm{UL}}(t)$ for any exposure duration.

From Equations 5.10, 5.11, and 5.12, the capacitance of the HASEL can be written as

$$C_{\mathrm{HASEL}} = \frac{\tau_2}{R_{\mathrm{ESR}}+R_{\mathrm{human}}} = \frac{-t}{\ln\left(\frac{R_{\mathrm{ESR}}+R_{\mathrm{human}}}{V_0} * I_{\mathrm{human}}(t)\right) * (R_{\mathrm{ESR}}+R_{\mathrm{human}})} . \tag{5.13}$$

Then, to meet the UL safety standards,

$$C_{\mathrm{HASEL}} \leq \frac{-t}{\ln\left(\frac{R_{\mathrm{ESR}}+R_{\mathrm{human}}}{V_0} * I_{\mathrm{UL}}(t)\right) * (R_{\mathrm{ESR}}+R_{\mathrm{human}})}, \tag{5.14}$$

when $t \geq 10^{-6}$ s. The minimum of equation 5.14 guarantees a capacitance value of the actuator that meets the UL criteria for discharge current and duration of exposure:

$$C_{\mathrm{critical}} = \min\left(\frac{-t}{\ln\left(\frac{R_{\mathrm{ESR}}+R_{\mathrm{human}}}{V_0} * I_{\mathrm{UL}}(t)\right) * (R_{\mathrm{ESR}}+R_{\mathrm{human}})}\right). \tag{5.15}$$

Using the above derivation for DEAs, Pourazadi et al. (*63*) compared simulated discharge currents of DEAs with the UL safety standard, Figure 5.12a. The blue curves represent results when the DEA was charged to V_0 = 10 kV, while the red curves are for a voltage of V_0 = 1 kV. The solid curves represent a total resistive load ($R_{\mathrm{ESR}} + R_{\mathrm{human}}$) of 10 kΩ, the light dashed curves represent 5 kΩ, and the dark dashed curves represent 15 kΩ. For each resistive load and starting

voltage, the critical capacitance was calculated using equation 5.15, and found to be 258 nF for the blue curves and 37.1 µF for the red curves. Importantly, the total resistive load substantially effects the critical capacitance; that is, if the resistive load is increased, so is the critical capacitance and vice versa. This effect can be seen in Figure 5.12b, which plots the critical capacitance as a function of voltage for various resistive loads. Values below these curves are deemed nonhazardous.

To put these results into perspective, consider HASEL actuators operating at 8 kV as shown in Section 5.2 for the 10-channel HVPS. At this voltage and a very conservative estimate of 500 Ω (a calloused, dry human hand can have a resistance of >100,000 Ω (*98*) and the series resistance of the carbon-based electrodes is on the order of kilohms) for the equivalent series resistance of the electrodes and the human skin, accidental contact with a HASEL actuator is safe if its capacitance is below a critical value of 100 nF, which equates to the capacitance of 200 donut actuators shown in Section 5.2 connected in parallel.

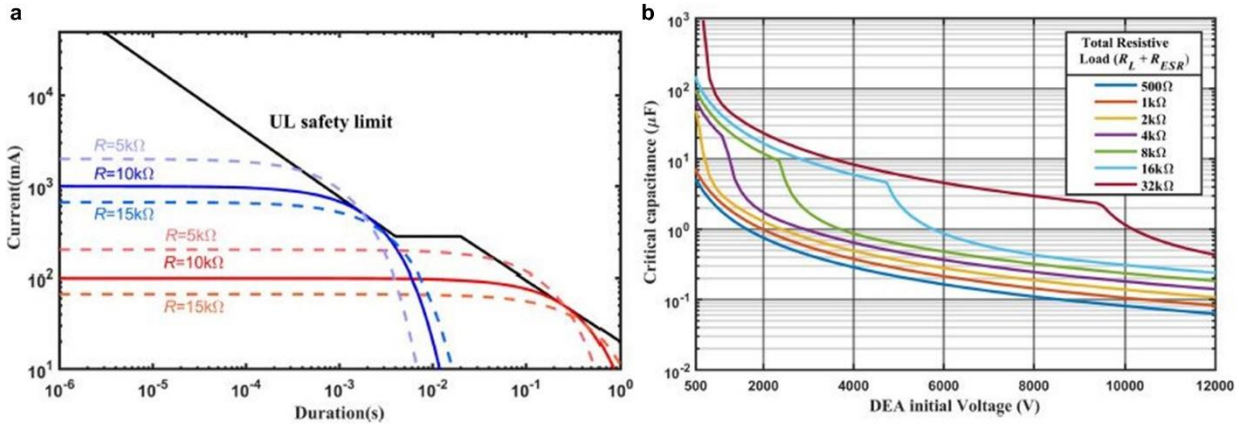

Figure 5.12: Safety predictions adhering to the UL standards for the discharge of electrostatic actuators in contact with the human body. a) Discharge current as a function of exposure duration. Curves below the UL safety limit are deemed nonhazardous. The blue curves signify a 10 kV discharge using a critical capacitance of 258 nF and the red curves signify a 1 kV discharge using a critical capacitance of 37.1 µF. b) Critical capacitance as a function of discharge voltage. The different colored curves represent various resistive loads, $R_{ESR} + R_{human}$. For a given resistive load, critical capacitance values below the curve are deemed nonhazardous. Reproduced from (*63*).

When the actuator is connected to an activated power supply and then accidentally discharged to a human, the maximum output current of the HVPS must also be considered for the safety of the system. According to the UL safety standards currents under 20 mA pose no threat of ventricular fibrillation for any extent of exposure (*97*). Therefore, limiting the output current of the amplifier to 20 mA ensure safe operation for the user, but it is important to note that limiting the current can restrict the dynamic response of the actuator. The speed of actuation and safety requirements need to be carefully weighed when designing systems of HASEL actuators. Moreover, to safely operate large robotic systems with high-speed HASEL actuators, one can design such systems with electrically independent subsystems, where each subsystem achieves the desired actuation speed while adhering to the safety considerations discussed above.

6 Applications: Mining asteroids with soft robots

6.1 Background

This work is an introduction and overview of Area-of-Effect Softbots (AoES), which are currently in development under a Phase 2 NASA Innovative Advanced Concepts (NIAC) project (*99*). The motivation for this work is to explore and mine near Earth asteroids (NEAs) to extract various minerals, precious metals, and most importantly, water. The mission, Figure 6.1, utilizes a mothership that maintains orbit around the asteroid while a number of AoES use solar radiation pressure (SRP) to navigate to the surface of the asteroid and safely land. Once landed, the AoES will be required to traverse the rocky and dusty terrain by crawling and hopping. Then, the AoES will extract material from the surface of the asteroid using a digging mechanism which launches the debris into space for collection by the mothership.

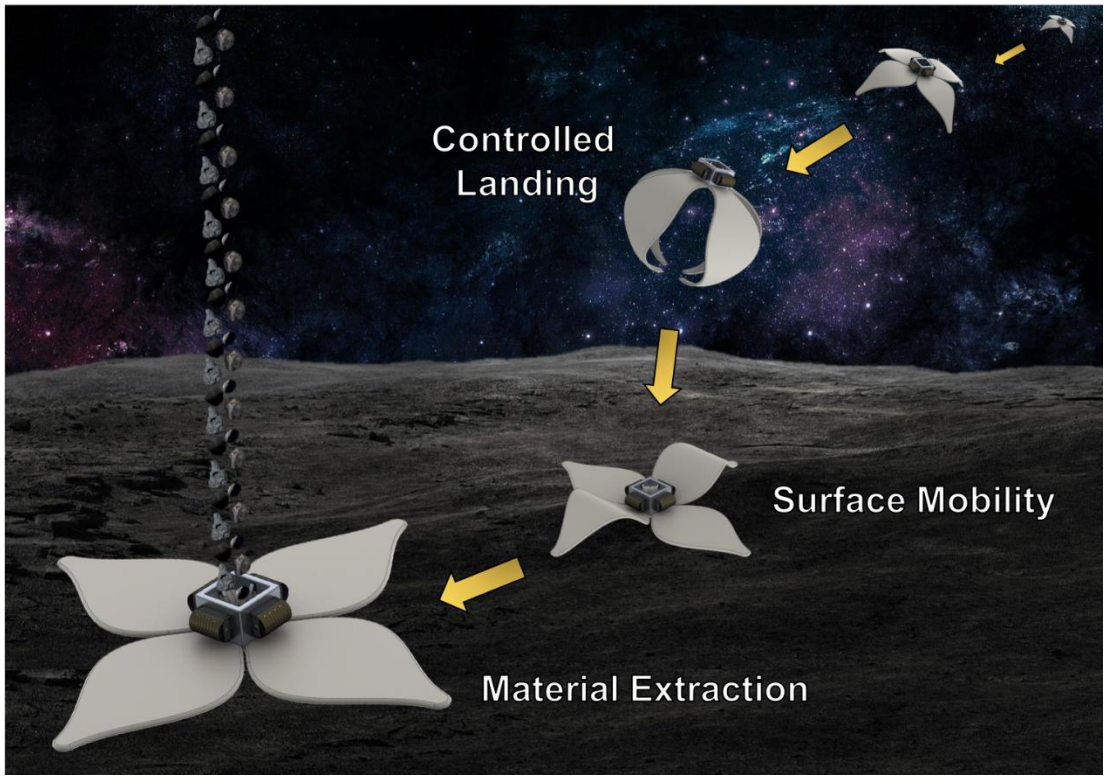

Figure 6.1: Mining asteroids with Area-of-Effect Softbots (AoES). *(99)*

6.2 Proposed concept

This chapter will focus primarily on the design requirements and basic architecture of the robot that will enable surface mobility on the peculiar surface of the asteroid. The fundamental design of AoES will harnesses a large area-to-mass ratio to take advantage of the peculiarities inherent to the environment of small asteroids. Figure 6.2 shows a schematic the AoES concept. The robot features two main components, the limbs and the central bus. The large limbs of the robot enable a number of functionalities. First, the large surface area of the limbs enables the robot to utilize SRP to sail to the surface of the asteroid, without the need for a propulsion system. Secondly, the soft and compliant limbs provide a means for a safe landing on the surface of the asteroid, which is largely unknown but may contain rocky and dusty regolith. The limbs also enable locomotion across this hard-to-predict terrain. And finally, because the asteroids are held loosely together by microgravity, with an escape velocity on the order of 10 cm s^{-1}, the large limbs provide stability for the robot on the surface, preventing the robot from sinking while simultaneously providing adhesion through van der Waals forces and electroadhesion. The central bus of the robot contains the electronics for actuation and electroadhesion, the digging and launching mechanisms, and a radioisotope thermoelectric generator (RTG) as the energy source (since the robot will need to function primarily in a dusty environment, solar panels cannot be used as the primary energy source). (*99*)

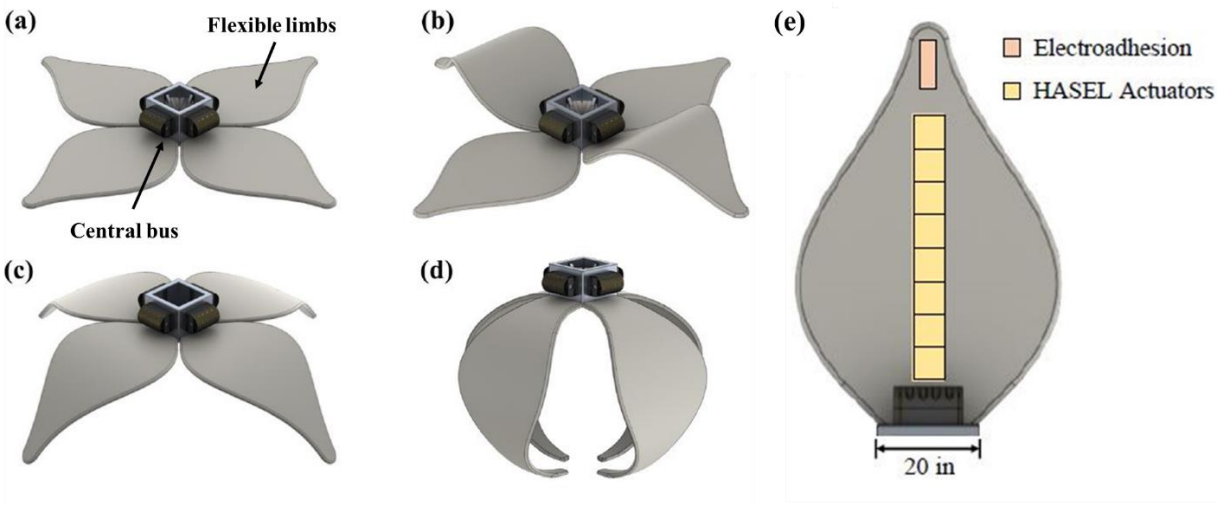

Figure 6.2: The AoES concept. a) Preliminary design of the robot which contains a central bus that houses a digging mechanism, electronics, and an RTG. In this configuration, the robot could anchor to the surface of the asteroid or solar sail. b) actuation of the limbs to cause the robot to crawl, c) hop, d) and land. e) The structure of a limb features HASELs for bending actuation and an electroadhesion anchoring system. (*99*)

6.2.1 Spider-inspired Electrohydraulic Soft-actuated (SES) joints

The AoES will utilize HASEL actuators to bend the soft limbs, since HASELs provide a power and mass efficient actuation mechanism and a large design freedom that can utilize space-grade materials. One geometry of HASEL actuators that was explored for this application was a Spider-inspired Electrohydraulic Soft-actuated (SES) joint, Figure 6.3. These devices consist of a HASEL actuator that is adhered to two passive stiffening layers connected by a flexible hinge. Upon activation, the electrodes zip together and pump the fluid into the hinged region. The increased pressure within this region causes flexion of the joint. The unique combination of electrostatic and hydraulic forces coupled with discrete stiffening layers results in a soft-actuating joint that features efficient force transmission for fast and strong actuation, backdrivability, and the ability to be parallelized to increase functionality.

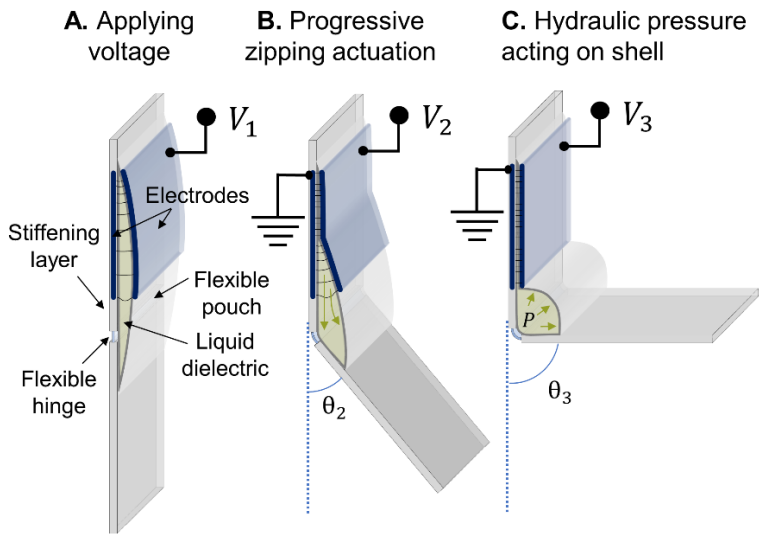

Figure 6.3: Spider-inspired electrohydraulic soft-actuated (SES) joints. a) The actuators consist of a flexible pouch filled with liquid dielectric, and a pair of opposing electrodes on the outside. A stiffening layer is placed on one side to constrain actuation while a flexible hinge provides stability and a passive restoring force. b,c) On application of voltage, Maxwell stress causes the electrodes to zip together progressively, which pressurizes the liquid dielectric (P) and causes flexion of the joint to angle θ.

We presented two methods of combining SES joints to increase the functionality of these soft robotic devices – antagonist arrangements that allow bidirectional actuation and series arrangements that increase flexion angles, Figure 6.4a. The bidirectional actuators (Figure 6.4b-d) are designed such that they share a common inner electrode, while the outer electrodes can be operated independently. Using a custom H-bridge circuit, we selectively activated the left and the right actuators. This joint was capable of nearly ± 20º of actuation, as well as high-speed movement that resembled the thunniform swimming motion seen in many species of fish, such as the yellowfin tuna (*100*). Furthermore, towards the goal of creating maneuverable robots with a large number of independently controlled actuators, we demonstrated an artificial spider limb consisting of three independently controlled SES joints in series, Figure 6.4e-g. The limb was designed with a tapered structure, with the largest actuator positioned at the base of the limb to support the additional torque required to lift the subsequent actuators. The actuators shared a ground

connection, but had independent high voltage leads that were activated using a three-channel high voltage power supply. Figure 6.4f shows discrete and sequential actuation of each joint with a maximum applied voltage of 8 kV; under no load the limb was able to reach nearly 180 degrees of flexion. Inverting the structure, the artificial spider limb was able to easily lift itself with voltage-controlled output angles, Figure 6.4g.

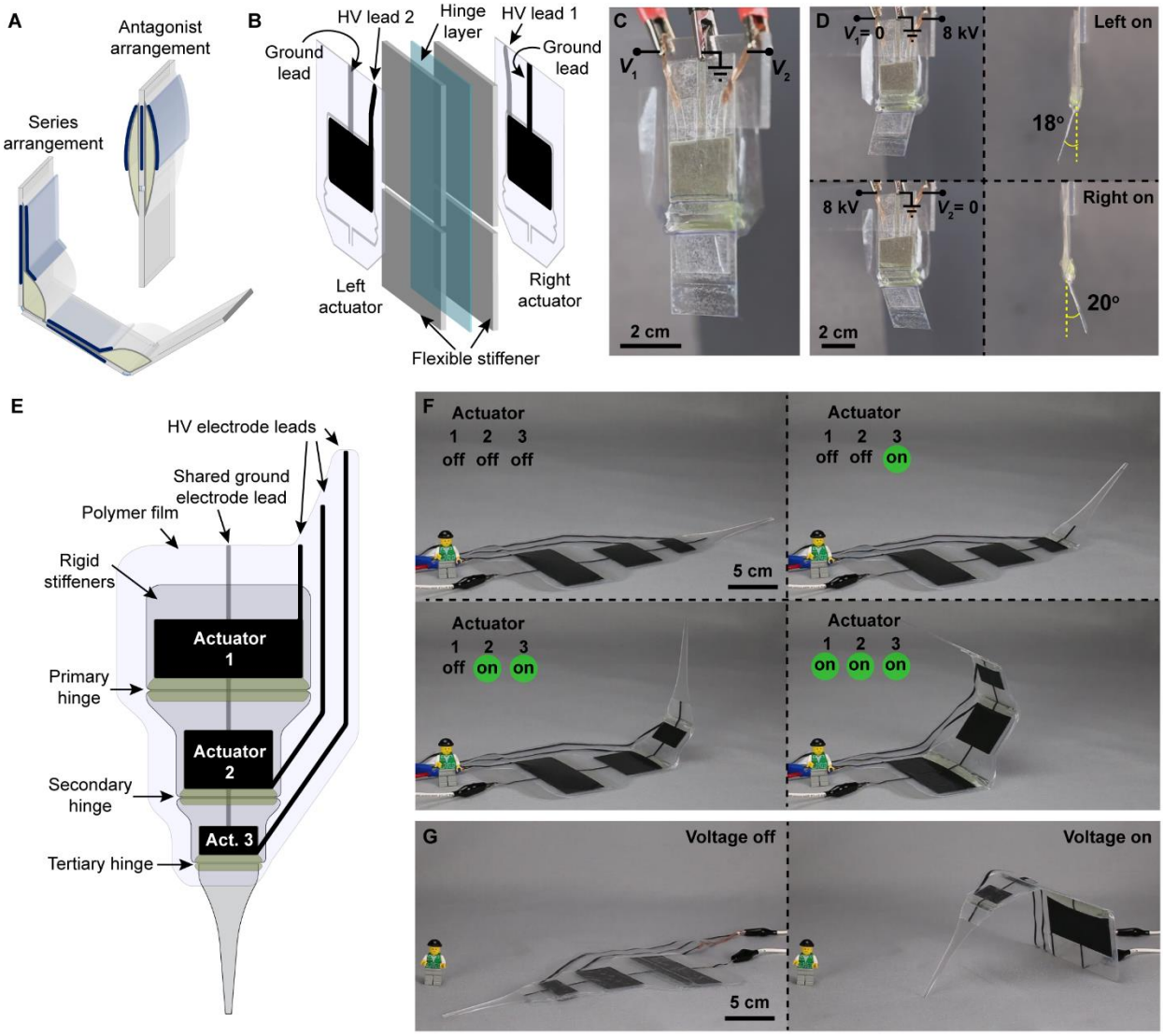

Figure 6.4: Antagonistic SES joints for bidirectional actuation and series arrangement of joints to increase functionality. a) A schematic of a bidirectional and a series arranged joint. b) A bidirectional SES joint was created by placing one actuator on either side of a bidirectional hinge using transfer tape (not shown). The hinge was made from flexible stiffeners attached to a two-side adhesive transparency. A gap in the stiffeners allowed for bidirectional actuation in the hinge. c) A bidirectional SES joint made from two 2x4x1 cm BOPP actuators. Each actuator was

independently controlled using V_1 and V_2. d) Activating the left (top) and right (bottom) actuators separately using a volt age of 8 kV resulted in hinge angles of 18 degrees and 20 degrees respectively. e) By placing several SES joints in series, the overall flexion angle was increased, creating an artificial limb with independently addressable joints. f) Three SES joints activated sequentially with voltages of 8 kV. g) When the actuators were facing downward, the limb could lift itself off the ground.

6.2.2 Electroadhesion

A vital capability of AoES is their ability to adhere to the terrain of the asteroid in order to effectively navigate and mine the surface. These robots will be designed with a large area-to-mass ratio to take advantage of van der Waals forces (*99*) but will possess active adhesion through an electrostatic mechanism known as electroadhesion (EA). This electrically controlled adhesion technology demonstrates excellent adherence (2 N cm^{-2}) to a variety of conductive and insulating substrates, while consuming little power (20 mW N^{-1} of load held) (*101–103*), which would allow for large-area adhesion to the asteroid surface. EA is achieved through electrostatic fringe fields generated between interdigitated electrodes connected to a potential difference, Figure 6.5. These fringe fields polarize the substrate material resulting in an electrostatic attraction that resists normal and shear forces between the EA pad and the substrate.

Electroadhesion is a complex phenomenon that depends heavily on environmental conditions (temperature, humidity, etc.), the surface texture of the EA pad and substrate, the distance between the pad and substrate, as well as dynamic material properties of the pad and substrate that are influenced by high-voltage-polarization/depolarization (*102*, *104*, *105*). These factors make it difficult to develop analytical models that accurately predict the dynamic performance of EA devices, especially when various substrates are considered. Ongoing work utilizes empirical modeling based on experimental data to inform EA design and performance. In general, however, the EA force is determined by the Maxwell stress tensor (similar to HASEL

actuators); and therefore, this force is proportional to the square of the applied electric field as well as the permittivity of the dielectric(s) (*106*).

EA pads can be constructed from a plethora of compliant and lightweight materials (*103*, *107–110*), enabling the design of an anchoring system that can withstand the extreme environments found in space while maintaining a high level of adaptability. Since electroadhesion uses similar operating voltages (~5 kV) as HASEL actuators, the same onboard power supply may be used for both actuation and adhesion, without the need for additional power sources. Figure 6.6 shows a prototype of a crawling robot that integrates an SES joint with EA pads. Through bending actuation and selective anchoring with EA, the robot could crawl up a cardboard substrate at a 16.5º incline

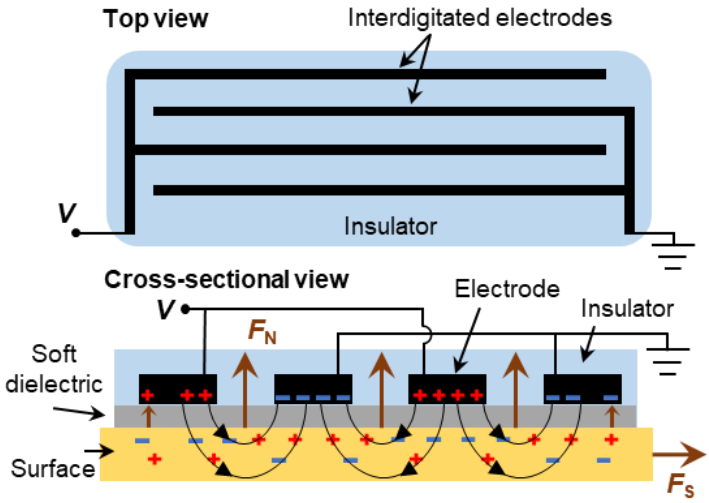

Figure 6.5: Basic design and operating principle of electroadhesion.

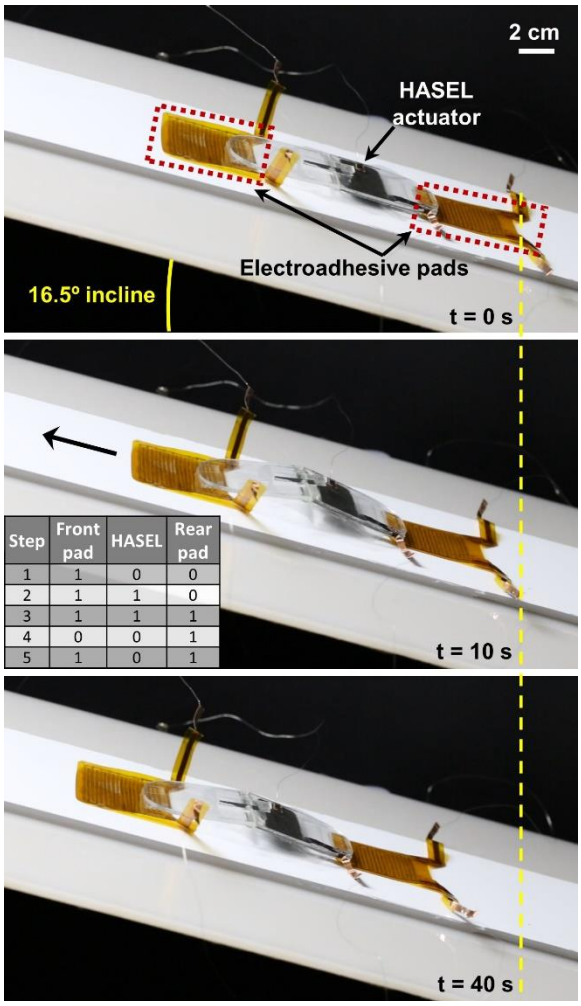

Step	Front pad	HASEL	Rear pad
1	1	0	0
2	1	1	0
3	1	1	1
4	0	0	1
5	1	0	1

Figure 6.6: A crawling robot with integrated electroadhesion. The actuator was an SES joint and the EA pads utilized the geometry seen in Figure 6.5. The EA pads consisted of Kapton tape as the dielectric and insulator and conductive fiber tape as the interdigitated electrodes. The actuation and adhesion steps can be seen in the table within the second image. The binary representation signifies a 1 for activated and a 0 for deactivated. (*99*)

Adhering to dusty, rocky, and unpredictable surfaces is an essential function of AoES. While many EA devices have been demonstrated, like multifunctional grippers and wall-climbing robots (*30*, *108*, *111*, *112*), very few studies analyze EA forces on rough or granular media (*113–115*). Therefore, this work intends to develop and study EA devices that can cling to peculiar surfaces. Our current design for the EA pad can be seen in Figure 6.7a. We use a 12-μm-thick thermoplastic polyurethane (TPU, Shenzhen Tunsing Plastic) film as the soft dielectric. This film

was chosen because of its high mechanical compliance and dielectric constant ($\varepsilon = 8.5$). An off-the-shelf conductive carbon ink (126-03FS, Creative Materials) was used for the electrode material. This ink was diluted with toluene (99.8%, Sigma Aldrich) in a 2:1 ratio in order to obtain a consistency that would allow application as an aerosol via an airbrush. A stencil of the electrode pattern was laser cut from a masking tape and paper composite which was then adhered to the surface of the TPU. The ink was then applied with an airbrush and was left to dry for 12 hrs. The design of the electrodes was a spiral pattern with an overall diameter of 80 mm, a trace width of 1 mm, and a distance between traces of 1 mm. This design was chosen to promote a uniform EA force independent of the direction of the applied shear force (*102*). Once the ink dried, the stencil was carefully removed from the TPU and copper tape (0.25'' thick, Favordrory) was attached to the carbon leads of the EA pad to allow easy electrical connection to a HV amplifier. Then, a 100-µm-thick layer of silicone elastomer (Ecoflex 00-30) was blade cast over the electrodes to ensure electrical isolation. The silicone was left to cure at room temperature for 1 hour. Finally, acrylic mounts were applied to the top and bottom of the pad to easily attach mechanical loads.

An example of the experimental setup and procedure to test the shear force of an EA pad can be seen in Figure 6.7. With the TPU side facing the substrate, the EA pad was charged to 3 kV for 1 minute. Then a force-controlled artificial muscle tester (310-LR, Aurora Scientific 3000) was used to linearly increase the shear force applied to the pad (Figure 6.7d). The measured shear force on several different substrates is summarized in Figure 6.8 and Table 6.1. Notably, the average shear force on metalized PET was 14.44 N. Table 6.1 also shows preliminary results for two granular media: sand and regolith simulant. The regolith is made by the CLASS Exolith lab at the University of Central Florida and is meant to mimic extraterrestrial terrains. While the shear forces obtained in these experiments are quite low compared to the monolithic substrates (average shear

force for sand and regolith were 42 mN and 58 mN, respectively), recall that the AoES will be operating in a microgravity environment. As an example, consider the average EA force on regolith of 58 mN. In Earth's gravity, this adhesive force will pick up about 6 g of regolith, but in a microgravity environment, that same force will pick up 6000 kg of regolith!

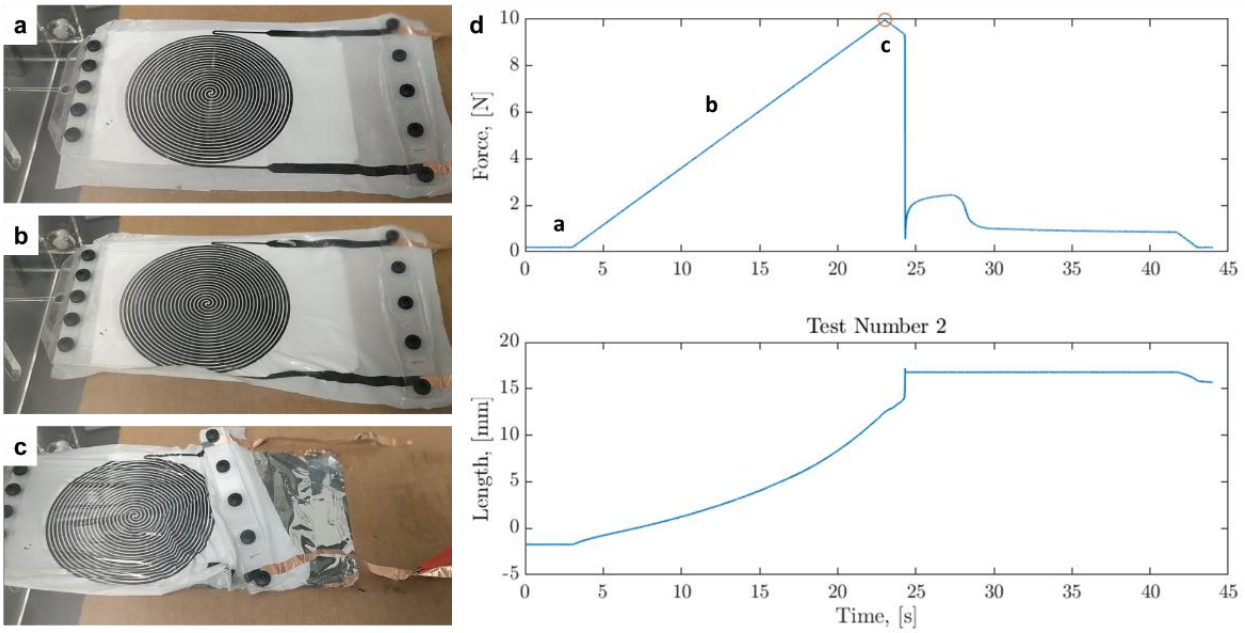

Figure 6.7: Experimental procedure for electroadhesion tests. The substrate in this example is metalized PET. a) A spiral-shaped EA pad is activated under an applied voltage of 3 kV. b) An applied shear force is ramped up linearly. The EA pad stretches slightly as the force is applied. c) Eventually, the applied shear force overcomes the EA force and the pad slips. d) Force and length data as a function of time for one shear test. The corresponding timestamps for images a), b), and c) are shown in the plot of the force data.

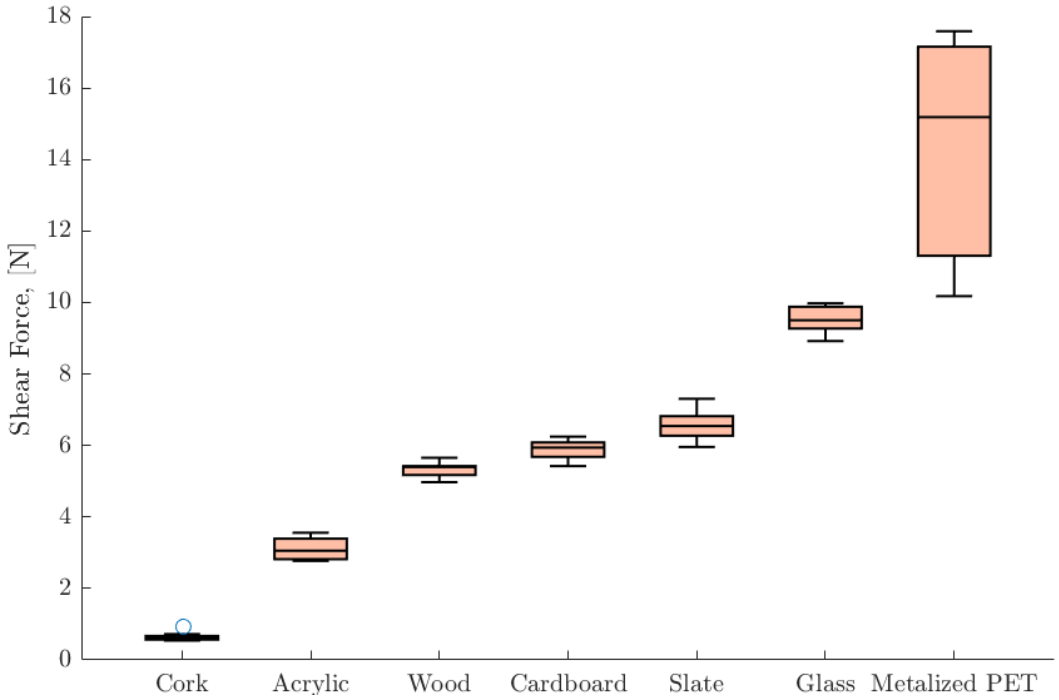

Figure 6.8: Box and whisker plot for the preliminary experimental results of electroadhesion on various substrates. Shear forces generated by electroadhesion were measured on cork, acrylic, wood, cardboard, slate, glass, and metalized PET.

Material	Minimum (N)	Average (N)	Maximum (N)
Sand	0.004	0.042	0.071
Regolith	0.035	0.058	0.078
Cork bark	0.54	0.64	0.93
Acrylic	2.77	3.10	3.56
Wood	4.97	5.33	5.66
Cardboard	5.43	5.88	6.25
Slate	5.96	6.01	7.31
Glass	8.92	9.51	9.97
Metalized PET	10.18	14.44	17.59

Table 6.1: Summary of preliminary results for electroadhesion on various substrates.

6.3 Outlook

6.3.1 Experiments with electroadhesion on granular media

The shear force experiments on granular media pose a challenge that future work will need to be address. The small shear forces measured on granular media are close to the resolution of the artificial muscle tester, which resulted in inconclusive data. These small forces are most likely due to non-uniform contact between the EA pad and the substrate, since the EA force relies on the proximity of the EA pad with the substrate, acting best over distances of micrometers (*102*). Therefore, an experiment must be designed to promote better conformity between the EA pad and the irregular surface of the substrate in order to exert a measurable force. One method to promote conformity can be seen in Figure 6.9, wherein the EA pad is charged and then pressed normal into the substrate (in this case regolith) with a soft foam backing. When the pad was lifted off the surface, it adhered to some granules of regolith. It is important to note that this experimental method relies on cohesive forces between the granules of regolith. These forces are typically small, and therefore may not be detectable with the artificial muscle tester. In such a case, the EA pad can be weighed before activation and then while activated and holding onto granules. The difference in weight can be attributed to the mass of the granules, which can then be correlated to an EA force.

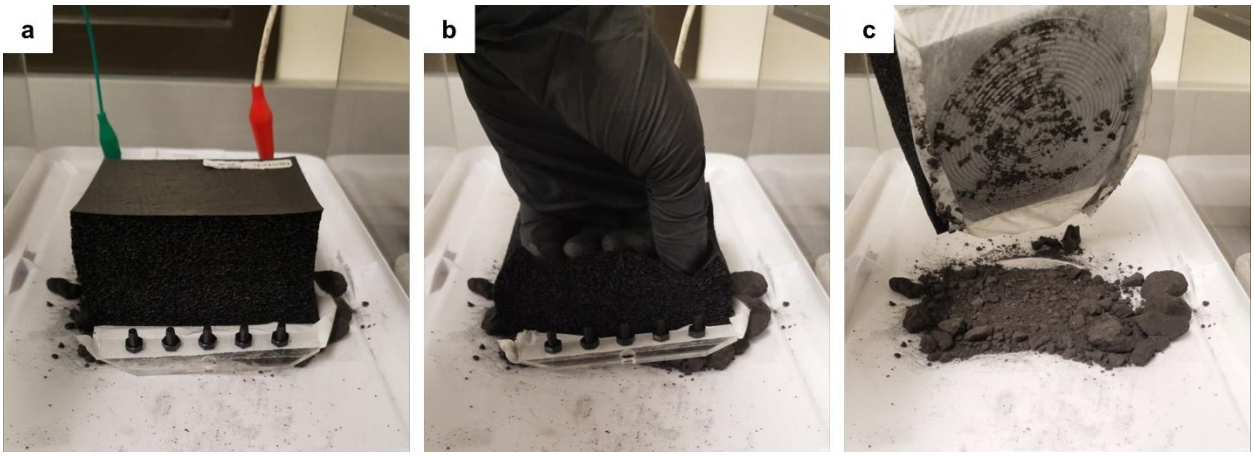

Figure 6.9: Improving conformity between an EA pad and granular media. An example of an experiment where a) a soft foam backing was placed on top of an EA pad that was charged to 4.5 kV while resting on a granular media (regolith). b) With the pad charged, a normal force was applied to the foam, thereby conforming the EA pad to the regolith. c) The pad was lifted from the surface and picked up granules of regolith.

6.3.2 Materials that can withstand the harsh environments encountered in space

The AoES will be required to withstand not only the rocky and dusty surface of the asteroid, but also the harsh conditions of space with temperature swings ranging from -80 ˚C to 150 ˚C, extreme vacuum pressures, and intense radiation. Therefore, the actuation and electroadhesion mechanisms must be designed using materials that can endure these conditions. Below is a list of possible materials for HASEL actuators and EA pads that may be suitable for operation in space:

1) *Solid Dielectrics for HASEL actuators and EA*

Elastomer-based systems: Silicones such as Esterline ELA-SA-401, Parker Hannifin S0383-70, Parker Hannifin S0899-50 are low outgassing (per ASTM E595), and have been tested from -50˚C – 125˚C.

Thin film dielectrics: PET, PEN, Kapton, Teflon, and FEP can be made in a variety of thicknesses, and have been tested for space environments.

2) *Fluidic dielectrics: Working fluid within a HASEL actuator*

Gaseous dielectrics: Nitrogen maintains insulating properties to near-cryogenic temperatures

Cryogenic liquids: Liquid nitrogen has been demonstrated as a dielectric liquid previously

Insulating oils: Low-temperature silicone liquid dielectrics such as PSF-5cSt, which has a working range of -70˚C – 150˚C with low viscosity. Demnum S-200 (perfluoropolyether oil), which has an operating temperature range of -70 ˚C to 300 ˚C, and low off-gassing due to vapor pressures of 3 x 10^{-9} Pa @ 20 ˚C, 2 x 10^{-5} Pa @ 100 ˚C.

3) *Compliant conductors*

Metalized layers: Aluminum metalized layers have been demonstrated as electrodes for HASELs previously.

To date, we have conducted high and low temperature thermal tests on donut HASEL actuators built from 20-µm-thick polyethylene terephthalate (PEL0WS, Multi-Plastics) thermoplastic thin film as the dielectric shell, a low viscosity silicone oil (5 cSt, 317667-1L MKCG6784 Sigma Aldrich) as the liquid dielectric, and screen-printed carbon ink (CI-2051, Engineered Materials Systems) as the electrodes. The preliminary results of these tests are shown in Figure 6.10. Figure 6.10a displays the results of the high temperature tests using one donut actuator. The actuator maintains actuation stroke up to 85 ˚C, but the performances falls off sharply at 93 ˚C. At around 90 ˚C the thermoplastic films between the electrodes are heat-sealed together, which prevents the actuator from displacing the liquid dielectric. Therefore, actuators will need to be designed using thin films that are not thermoplastics or have thermoplastic layers that melt at much higher temperatures (*i.e.* Kapton-120FN616 polyimide film).

Figure 6.10b shows the results of the low temperature tests using a stack of 10 donut HASEL actuators. It was observed that as the temperature reached -45 ˚C and lower, the quasi-static actuation stroke decreased. Since these experiments were conducted with an actuation

frequency of 1 Hz, it is not believed that an increase in the viscosity of the liquid dielectric resulted in a decrease in the quasi-static actuation stroke (*116*). Therefore, two alternative explanations are posited; the mechanics of the thin-film dielectric are affected by the low temperatures, or a frost layer that formed on the actuators prohibited the device from reaching its steady-state deformation. It should be noted that the latter hypothesis would not occur in a vacuum setting (i.e. space) since water molecules would not be present. Based on the datasheet for the thin film, the materials should be able to withstand temperatures as low as -75 ˚C, yet the effects of these temperatures on the mechanics of the film are unknown. Additionally, future experiments will need to analyze the mechanics of the thin-film dielectric at low temperatures, as well as monitor and control the humidity of the test chamber (or perform experiments in a vacuum chamber) to prevent frost from forming on the actuator.

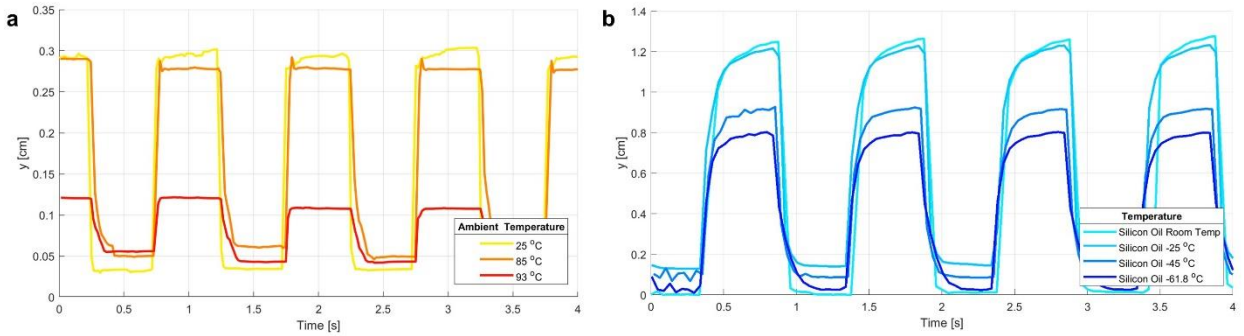

Figure 6.10: Preliminary results for thermal experiments conducted on HASEL actuators that were made from materials used in Chapter 5. The stroke of the actuator was monitored while it was operated at 8 kV and 1 Hz. a) Stroke (y-displacement) of one actuator as a function of time at or above room temperature. b) Stroke of a stack of 10 actuators as a function of time at or below room temperature.

7 Conclusion

7.1 Opportunities to improve HASELs built from elastomers

This dissertation presents state-of-the-art electrohydraulic actuators and their accompanying driving electronics, pushing towards functional untethered soft robots driven by these devices. In Chapter 2, we discuss the first work that described HASEL actuators and their fundamentals. This work focused primarily on constructing actuators from commonly used silicone elastomers, which revealed several interesting characteristics that are yet to be explored. Firstly, the pull-in instabilities of donut HASEL actuators may be exploited for applications that require bi-stable operation or large and rapid response to small changes of the input voltage. Inspired by unique actuation schemes in nature, bi-stable actuation has been utilized successfully in other soft actuator systems (*117–119*). The electrode placement and geometry in a donut HASEL actuator can be modified to achieve new types of functionalities, such as tunable lenses (*120*). Developing theories for both static and dynamic characteristics of elastomeric donut HASEL actuators could aid in the design of actuators for specific applications.

There are many materials-related opportunities to further develop elastomeric HASEL actuators. So far, thick layers (0.1 - 1 mm thick) of commercially available silicone elastomers have been used as the solid dielectrics of elastomeric HASEL actuators, as they are robust and easy to handle. Fabrication techniques for reliably producing HASEL actuators with thin elastomer layers (0.01 mm – 0.1 mm) would allow for operation at lower voltages. Further, efforts to produce high-quality elastomer films in a particulate-free environment would benefit the lifetime of elastomeric HASEL actuators, where dielectric breakdown is often driven by defects in the film layer. Self-healing from dielectric breakdown was successfully demonstrated, but there are opportunities for improvement. Even though HASEL actuators functionally recover from

dielectric breakdown, each breakdown event leads to the formation of gas in the liquid dielectric, and the elastomeric shells remain damaged (holes in the shells do not self-heal, but can self-seal thus preventing liquid-dielectric from leaking out). Repeated breakdown events may therefore result in regions of lower dielectric strength in the actuator and thus reduce performance. Incorporating elastomers which mechanically self-heal from damage as well as gas-permeable elastomers which allow for gas bubbles to quickly clear from the liquid dielectric region would improve the self-healing performance of HASEL actuators.

7.2 Opportunities to improve HASELs built from thermoplastics

In Chapters 3 and 4, we discussed fabrication techniques to rapidly prototype actuators built from thin film thermoplastics. These techniques and associated material systems provide a design freedom that has yet been fully explored. While initial work on thermoplastic HASEL actuators has focused on exploring fundamental actuation modes spanning linear contraction, expansion, curling, and twisting, future work will likely shift towards application-driven designs and new functionalities. For example, integrating thermoplastic actuators with structural components may enable antagonistic groups of actuators that can support and generate both tensile and compressive forces. Further, adding elastic components into thermoplastic HASEL actuators may provide means for mechanical energy storage (and fast release), like the system of muscles and tendons in the human body. These research avenues may be supported by a systematic modeling-based approach that improves the understanding of the electromechanical behavior of thermoplastic HASEL actuators and helps to identify design criteria.

Great potential for the improvement of the performance of thermoplastic HASEL actuators lies in the development of specialized materials. Most materials that have been used to date for

thermoplastic HASEL actuators were originally developed for the packaging industry because they are inexpensive, available in large quantities, and incorporate heat-sealing layers that aid bonding of the films. Even though these films have good mechanical properties, they were not optimized for electrical properties. Other materials such as polyvinylidene fluoride (PVDF) have been optimized for high-voltage applications (*e.g.*, high voltage thin film capacitors) and therefore possess good electrical properties, but poor mechanical properties. New materials with high dielectric constants and high dielectric breakdown strengths, as well as high mechanical strength and flexibility, would drastically expand the scope of practical applications for HASEL actuators.

Electrical and mechanical self-healing performance represents another important factor in actuator lifetime; unlike elastomeric HASEL actuators, thermoplastic actuators show very limited self-healing capabilities to dielectric breakdown, which punctures the polymer film. In designs in which electrodes are placed near the edges of the shell dielectric breakdown often occurs through the heat-seal of the shell, leading to electrical shorting of the actuator; this problem may be mitigated by using self-clearing electrodes, which insulate the damaged region (*121–123*). When dielectric breakdown occurs in the liquid-filled region of the shell, liquid dielectric begins to leak out of the pouch, a problem that may be mitigated by using an appropriate encapsulation. Development of self-healing thin-film layers would allow for more robust operation after dielectric breakdown events and would lead to longer lifetimes.

A multitude of polymer films with unique properties exists—with more being synthesized regularly—that cannot be heat-sealed. The use of adhesives to form shells may expand the range of usable materials and would avoid the heat-sealing process, which can damage the thermoplastic layers and cause premature dielectric breakdown through the heat seal and therefore decrease the maximum performance and the lifetime of actuators. Other methods of fabrication for HASEL

actuators including additive manufacturing are virtually unexplored and may substantially increase the design freedom.

Practical implementations of HASEL actuators will benefit from studies on the lifetime and failure modes present in thermoplastic HASEL actuators. The most prevalent mode of failure for heat-sealed systems is dielectric breakdown through the heat seal, typically near the edge of an electrode. This results in failure well below the critical electric fields measured in the films themselves. At times, this failure is preceded by repeated partial discharges through the air at the heat seal, suggesting potential electrical degradation. Methods to mitigate this failure mode could focus on eliminating partial discharges through air by implementing dielectric coatings, as observed by La et al. (*124*). Studies aiming to understand the effects of electric field concentrations at the edges of electrodes could further enhance actuator lifetime and reliability.

7.3 Opportunities to improve the driving electronics and control of HASELs

In Chapter 5, we develop a pocket sized 10-channel HVPS to drive HASEL actuators. The power supply benefits from the use of PWM-controlled optocouplers to create a charge-controlled actuation scheme. Yet, the realization of highly versatile and adaptable HASEL-driven robots with many degrees of freedom will require great strides in the development of driving electronics and controls. Off-the-shelf components that produce voltages on the order of 10 kV can be bulky and cost prohibitive. These drawbacks could be overcome by designing integrated high voltage circuits that are specific to the electrical requirements of HASEL actuators. Moreover, reducing the operating voltage of HASEL actuators to < 500 V could lead to a dramatic leap in the functionality and compactness of the driving electronics, since well-developed circuitry for piezoelectric actuators could be exploited (*125–127*). However, large arrays of HASEL actuators with high

energy density will require considerably more current than a few milliamperes when operated at their peak speeds; and so, electrical safety will need to be reconsidered for these systems. Techniques like matrix addressing (*92*, *128*, *129*) could be utilized regardless of the required voltage to create a compact electronics package capable of independently addressing hundreds or thousands of actuators, though such systems would require a complex network of high voltage electrical connections that would need to withstand high potential differences between adjacent cables.

While this dissertation does not focus on sensing and control of HASELs, other work to date on self-sensing and closed-loop control of HASEL actuators has been promising. Recently, a reliable, low-cost, and miniaturized self-sensing circuit has been demonstrated for HASEL actuators (*93*); integrating such techniques into the 10-channel HVPS will enable functionality not yet seen from HASELs driven by a compact power supply. Moreover, soft logic developed for DEAs (*69*, *130*, *131*) may be extended to HASEL-based robots to couple actuation, sensing, and local feedback control in an all-soft-matter architecture, closely replicating the cohesive functionality of the muscular and nervous systems.

Gifting soft robots with extended periods of untethered mobility necessitates extremely efficient electronics for actuation, sensing, and computation (*64*). HASEL actuators have demonstrated high full-cycle efficiency and (because they are electrically driven actuators) they are particularly well-suited for creating robots with high system efficiency. Charge recovery circuitry inspired by the field of piezoelectric actuators (*132*, *133*) could be used to improve the system efficiency by recovering the electrical energy discharged from HASEL actuators when they are deactivated. More advanced concepts may utilize the ability of HASEL actuators to operate as

electrostatic generators to convert mechanical energy from environmental perturbations into usable electricity.

7.4 Understanding actuator performance under realistic environment conditions

Chapter 6 discusses potential applications of HASEL actuators as components of robots that explore extraterrestrial environments. We develop actuation mechanisms as well as electroadhesives with the goal of assisting locomotion on diverse and unknown terrains. While the proposal of mining asteroids may seem farfetched, there are lower-hanging opportunities that will help elucidate the efficacy of HASELs in extreme environments. For instance, the robot described in Chapter 6 could be used to explore hard to reach underground caverns for research purposes or search and rescue missions. Additionally, with the recent discovery of abundant amounts of ice on the moon (*134*), the robot could be used as an alternative to lunar rovers, as it presents an unmanned, lightweight, and potentially inexpensive design meant to explore dusty and rocky environments with lower gravity than Earth.

As HASEL actuators find further application in the real world, it will be important to understand their actuation performance, lifetime, and reliability in diverse and dynamic environments here on Earth. For example, the effects of humidity must be studied in detail, as it has been shown to play a role in both the electrical and mechanical performance of dielectric elastomer actuators (*135*, *136*). In addition, studies that focus on the temperature dependence of HASEL actuators are critical to inform a practical design of the devices.

7.5 Closing remarks

The rapidly growing field of soft robotics merges disciplines towards creating the next generation of machines that will shape our world. It is my believe that the work presented here is a foundation with which these new machines can be realized. Though, there is still a long road ahead and only hard work, creativity, and time will tell.

I am honored to have conducted the work presented in this dissertation with my colleagues in the Keplinger research group over the past 5.5 years. Not only has this work been extremely rewarding to me on both a personal and professional level, but it has also helped shaped the field of soft robotics. I am sure that future developments by Christoph and the rest of the team as they continue to explore and push the boundaries of HASEL technology will be nothing short of spectacular. As for myself, the creative spirit instilled in me by the philosophy of the lab will live on as I continue to develop HASEL technology as a part of our spin-out company Artimus Robotics.

8 List of publications

Journal Publications

[7] P. Rothemund, N. Kellaris†, **S. K. Mitchell**†, E. Acome†, C. Keplinger, HASEL artificial muscles - recent progress and future opportunities. *Advanced Materials.* 2003375 (2020). (†Denote equal contributions)

[6] M. R. O'Neill, E. Acome, S. Bakarich, **S. K. Mitchell**, J. Timko, C. Keplinger, R. F. Shepherd, Rapid 3D Printing of Electrohydraulic (HASEL) Tentacle Actuators. *Advanced Functional Materials*. **30**, 2070266 (2020).

[5] X. Wang, **S. K. Mitchell**, E. H. Rumley, P. Rothemund, C. Keplinger, High-Strain Peano-HASEL Actuators. *Advanced Functional Materials*. **30**, 1908821 (2020).

[4] **S. K. Mitchell**, X. Wang†, E. Acome†, T. Martin, K. Ly, N. Kellaris, V. Gopaluni-Venkata, C. Keplinger, An Easy-to-Implement Toolkit to Create Versatile and High-Performance HASEL Actuators for Untethered Soft Robots. *Advanced Science* **6(14)** 1900178 (2019). († Denotes equal contributions)

[3] T. G. Morrissey, **S. K. Mitchell**, A. T. Jaros, E. Ambos, C. Keplinger, Mechanical-to-Electrical Energy Conversion with Variable Electric Double Layers. *Energy Technology*. **7**, 1801007 (2019).

[2] N. Kellaris, V. G. Venkata, G. M. Smith, **S. K. Mitchell**, C. Keplinger, Peano-HASEL actuators: Muscle-mimetic, electrohydraulic transducers that linearly contract on activation. *Science Robotics*. **3**, eaar3276 (2018).

[1] E. Acome, S**. K. Mitchell**, T. G. Morrissey, M. B. Emmett, C. Benjamin, M. King, M. Radakovitz, C. Keplinger, Hydraulically amplified self-healing electrostatic actuators with muscle-like performance. *Science*. **359**, 61–65 (2018).

Conference publications

[1] J. McMahon, **S. K. Mitchell**, K. Oguri, N. Kellaris, D. Kuettel, C. Keplinger, B. Bercovici, in *2019 IEEE Aerospace Conference* (2019), pp. 1–16.

Upcoming publications

[3] **S. K. Mitchell**, T. Martin, C. Keplinger, A pocket-sized 10-channel high voltage power supply. *In advanced preparation*

[2] N. Kellaris, P. Rothemund, Y. Zeng, **S. K. Mitchell**, G. M. Smith, K. Jayaram, C. Keplinger, Spider-inspired electrohydraulic actuators for fast, soft-actuated joints. *In revision*

[1] Z. Yoder, N. Kellaris, C. Chase-Markopoulou, D. Ricken, **S. K. Mitchell**, M. B Emmett, R. F. ff. Weir, J. Segil, C. Keplinger, Design of a High-speed Prosthetic Finger Driven by Peano-HASEL Actuators. *Accepted in Frontiers in Robotics and AI, 2020*

9 References

1. G. M. Whitesides, Soft Robotics. *Angewandte Chemie International Edition*. **57**, 4258–4273 (2018).
2. D. Rus, M. T. Tolley, Design, fabrication and control of soft robots. *Nature*. **521**, 467–475 (2015).
3. D. Trivedi, C. D. Rahn, W. M. Kier, I. D. Walker, Soft robotics: Biological inspiration, state of the art, and future research. *Applied Bionics and Biomechanics*. **5**, 99–117 (2008).
4. A. T. Asbeck, S. M. M. D. Rossi, I. Galiana, Y. Ding, C. J. Walsh, Stronger, Smarter, Softer: Next-Generation Wearable Robots. *IEEE Robotics Automation Magazine*. **21**, 22–33 (2014).
5. J. Byun, Y. Lee, J. Yoon, B. Lee, E. Oh, S. Chung, T. Lee, K.-J. Cho, J. Kim, Y. Hong, Electronic skins for soft, compact, reversible assembly of wirelessly activated fully soft robots. *Science Robotics*. **3**, eaas9020 (2018).
6. M. Sitti, Miniature soft robots — road to the clinic. *Nature Reviews Materials*. **3**, 74–75 (2018).
7. J. W. Booth, D. Shah, J. C. Case, E. L. White, M. C. Yuen, O. Cyr-Choiniere, R. Kramer-Bottiglio, OmniSkins: Robotic skins that turn inanimate objects into multifunctional robots. *Science Robotics*. **3**, eaat1853 (2018).
8. J. D. W. Madden, N. A. Vandesteeg, P. A. Anquetil, P. G. A. Madden, A. Takshi, R. Z. Pytel, S. R. Lafontaine, P. A. Wieringa, I. W. Hunter, Artificial muscle technology: physical principles and naval prospects. *IEEE Journal of Oceanic Engineering*. **29**, 706–728 (2004).

9. R. K. Katzschmann, J. DelPreto, R. MacCurdy, D. Rus, Exploration of underwater life with an acoustically controlled soft robotic fish. *Science Robotics*. **3**, eaar3449 (2018).

10. J. H. Pikul, S. Li, H. Bai, R. T. Hanlon, I. Cohen, R. F. Shepherd, Stretchable surfaces with programmable 3D texture morphing for synthetic camouflaging skins. *Science*. **358**, 210–214 (2017).

11. A. D. Marchese, C. D. Onal, D. Rus, Autonomous Soft Robotic Fish Capable of Escape Maneuvers Using Fluidic Elastomer Actuators. *Soft Robotics*. **1**, 75–87 (2014).

12. S. M. Mirvakili, I. W. Hunter, Artificial Muscles: Mechanisms, Applications, and Challenges. *Advanced Materials*. **30**, 1704407.

13. C. S. Haines, N. Li, G. M. Spinks, A. E. Aliev, J. Di, R. H. Baughman, New twist on artificial muscles. *Proceedings of the National Academy of Sciences*. **113**, 11709–11716 (2016).

14. J. C. Tuthill, E. Azim, Proprioception. *Current Biology*. **28**, R194–R203 (2018).

15. P. Polygerinos, N. Correll, S. A. Morin, B. Mosadegh, C. D. Onal, K. Petersen, M. Cianchetti, M. T. Tolley, R. F. Shepherd, Soft Robotics: Review of Fluid-Driven Intrinsically Soft Devices; Manufacturing, Sensing, Control, and Applications in Human-Robot Interaction. *Advanced Engineering Materials*, 1–22 (2017).

16. T. J. Wallin, J. Pikul, R. F. Shepherd, 3D printing of soft robotic systems. *Nature Reviews Materials*. **3**, 84–100 (2018).

17. S. Li, D. M. Vogt, D. Rus, R. J. Wood, Fluid-driven origami-inspired artificial muscles. *PNAS*. **114**, 13132–13137 (2017).

18. M. A. Robertson, J. Paik, New soft robots really suck: Vacuum-powered systems empower diverse capabilities. *Science Robotics*. **2**, eaan6357 (2017).

19. S. Terryn, J. Brancart, D. Lefeber, G. V. Assche, B. Vanderborght, Self-healing soft pneumatic robots. *Science Robotics*. **2**, eaan4268 (2017).

20. M. A. Meller, M. Bryant, E. Garcia, Reconsidering the McKibben muscle: Energetics, operating fluid, and bladder material. *Journal of Intelligent Material Systems and Structures*. **25**, 2276–2293 (2014).

21. M. Wehner, M. T. Tolley, Y. Mengüç, Y.-L. Park, A. Mozeika, Y. Ding, C. Onal, R. F. Shepherd, G. M. Whitesides, R. J. Wood, Pneumatic Energy Sources for Autonomous and Wearable Soft Robotics. *Soft Robotics*. **1**, 263–274 (2014).

22. M. T. Tolley, R. F. Shepherd, B. Mosadegh, K. C. Galloway, M. Wehner, M. Karpelson, R. J. Wood, G. M. Whitesides, A Resilient, Untethered Soft Robot. *Soft Robotics*. **1**, 213–223 (2014).

23. R. F. Shepherd, F. Ilievski, W. Choi, S. A. Morin, A. A. Stokes, A. D. Mazzeo, X. Chen, M. Wang, G. M. Whitesides, Multigait soft robot. *PNAS*. **108**, 20400–20403 (2011).

24. A. A. Stokes, R. F. Shepherd, S. A. Morin, F. Ilievski, G. M. Whitesides, A Hybrid Combining Hard and Soft Robots. *Soft Robotics*. **1**, 70–74 (2013).

25. R. Pelrine, High-Speed Electrically Actuated Elastomers with Strain Greater Than 100%. *Science*. **287**, 836–839 (2000).

26. G.-Y. Gu, J. Zhu, L.-M. Zhu, X. Zhu, A survey on dielectric elastomer actuators for soft robots. *Bioinspir. Biomim.* **12**, 011003 (2017).

27. C. Keplinger, M. Kaltenbrunner, N. Arnold, S. Bauer, Capacitive extensometry for transient strain analysis of dielectric elastomer actuators. *Appl. Phys. Lett.* **92**, 192903 (2008).

28. S. Rosset, B. M. O'Brien, T. Gisby, D. Xu, H. R. Shea, I. A. Anderson, Self-sensing dielectric elastomer actuators in closed-loop operation. *Smart Mater. Struct.* **22**, 104018 (2013).

29. G. Kovacs, L. Düring, S. Michel, G. Terrasi, Stacked dielectric elastomer actuator for tensile force transmission. *Sensors and Actuators A: Physical*. **155**, 299–307 (2009).

30. J. Shintake, S. Rosset, B. Schubert, D. Floreano, H. Shea, Versatile Soft Grippers with Intrinsic Electroadhesion Based on Multifunctional Polymer Actuators. *Adv. Mater.* **28**, 231–238 (2016).

31. I. A. Anderson, T. C. H. Tse, T. Inamura, B. M. O'Brien, T. McKay, T. Gisby, A soft and dexterous motor. *Appl. Phys. Lett.* **98**, 123704 (2011).

32. A. T. Conn, J. Rossiter, in *Electroactive Polymer Actuators and Devices (EAPAD) 2011* (International Society for Optics and Photonics, 2011; https://www.spiedigitallibrary.org/conference-proceedings-of-spie/7976/79761Z/Antagonistic-dielectric-elastomer-actuator-for-biologically-inspired-robotics/10.1117/12.880438.short), vol. 7976, p. 79761Z.

33. H. Mößinger, H. Haus, M. Kauer, H. F. Schlaak, in *Electroactive Polymer Actuators and Devices (EAPAD) 2014* (International Society for Optics and Photonics, 2014; https://www.spiedigitallibrary.org/conference-proceedings-of-spie/9056/90563C/Tactile-feedback-to-the-palm-using-arbitrarily-shaped-DEA/10.1117/12.2045302.short), vol. 9056, p. 90563C.

34. J. Cao, L. Qin, H. P. Lee, J. Zhu, in *Electroactive Polymer Actuators and Devices (EAPAD) 2017* (International Society for Optics and Photonics, 2017; https://www.spiedigitallibrary.org/conference-proceedings-of-

spie/10163/101631X/Development-of-a-soft-untethered-robot-using-artificial-muscle-actuators/10.1117/12.2260375.short), vol. 10163, p. 101631X.

35. T. Li, G. Li, Y. Liang, T. Cheng, J. Dai, X. Yang, B. Liu, Z. Zeng, Z. Huang, Y. Luo, T. Xie, W. Yang, Fast-moving soft electronic fish. *Science Advances*. **3**, e1602045 (2017).

36. R. Pelrine, R. D. Kornbluh, Q. Pei, S. Stanford, S. Oh, J. Eckerle, R. J. Full, M. A. Rosenthal, K. Meijer, in *Smart Structures and Materials 2002: Electroactive Polymer Actuators and Devices (EAPAD)* (International Society for Optics and Photonics, 2002; https://www.spiedigitallibrary.org/conference-proceedings-of-spie/4695/0000/Dielectric-elastomer-artificial-muscle-actuators-toward-biomimetic-motion/10.1117/12.475157.short), vol. 4695, pp. 126–137.

37. S. Diaham, S. Zelmat, M. L. Locatelli, S. Dinculescu, M. Decup, T. Lebey, Dielectric breakdown of polyimide films: Area, thickness and temperature dependence. *IEEE Transactions on Dielectrics and Electrical Insulation*. **17**, 18–27 (2010).

38. G. Kofod, W. Wirges, M. Paajanen, S. Bauer, Energy minimization for self-organized structure formation and actuation. *Appl. Phys. Lett.* **90**, 081916 (2007).

39. H. S. Lee, H. Phung, D.-H. Lee, U. K. Kim, C. T. Nguyen, H. Moon, J. C. Koo, J. Nam, H. R. Choi, Design analysis and fabrication of arrayed tactile display based on dielectric elastomer actuator. *Sensors and Actuators A: Physical*. **205**, 191–198 (2014).

40. C. S. Haines, M. D. Lima, N. Li, G. M. Spinks, J. Foroughi, J. D. W. Madden, S. H. Kim, S. Fang, M. J. de Andrade, F. Göktepe, Ö. Göktepe, S. M. Mirvakili, S. Naficy, X. Lepró, J. Oh, M. E. Kozlov, S. J. Kim, X. Xu, B. J. Swedlove, G. G. Wallace, R. H. Baughman, Artificial Muscles from Fishing Line and Sewing Thread. *Science*. **343**, 868–872 (2014).

41. J. Mu, M. J. de Andrade, S. Fang, X. Wang, E. Gao, N. Li, S. H. Kim, H. Wang, C. Hou, Q. Zhang, M. Zhu, D. Qian, H. Lu, D. Kongahage, S. Talebian, J. Foroughi, G. Spinks, H. Kim, T. H. Ware, H. J. Sim, D. Y. Lee, Y. Jang, S. J. Kim, R. H. Baughman, Sheath-run artificial muscles. *Science*. **365**, 150–155 (2019).

42. M. Kanik, S. Orguc, G. Varnavides, J. Kim, T. Benavides, D. Gonzalez, T. Akintilo, C. C. Tasan, A. P. Chandrakasan, Y. Fink, P. Anikeeva, Strain-programmable fiber-based artificial muscle. *Science*. **365**, 145–150 (2019).

43. S. Tawfick, Y. Tang, Stronger artificial muscles, with a twist. *Science*. **365**, 125–126 (2019).

44. A. Miriyev, K. Stack, H. Lipson, Soft material for soft actuators. *Nature Communications*. **8**, 1–8 (2017).

45. H. Wang, Y. Yao, X. Wang, L. Sheng, X.-H. Yang, Y. Cui, P. Zhang, W. Rao, R. Guo, S. Liang, W. Wu, J. Liu, Z.-Z. He, Large-Magnitude Transformable Liquid-Metal Composites. *ACS Omega*. **4**, 2311–2319 (2019).

46. M. Garrad, G. Soter, A. T. Conn, H. Hauser, J. Rossiter, in *2019 2nd IEEE International Conference on Soft Robotics (RoboSoft)* (2019), pp. 74–79.

47. E. Acome, S. K. Mitchell, T. G. Morrissey, M. B. Emmett, C. Benjamin, M. King, M. Radakovitz, C. Keplinger, Hydraulically amplified self-healing electrostatic actuators with muscle-like performance. *Science*. **359**, 61–65 (2018).

48. Z. Suo, Theory of dielectric elastomers. *Acta Mechanica Solida Sinica*. **23**, 549–578 (2010).

49. Y. Bai, B. Chen, F. Xiang, J. Zhou, H. Wang, Z. Suo, Transparent hydrogel with enhanced water retention capacity by introducing highly hydratable salt. *Appl. Phys. Lett.* **105**, 151903 (2014).

50. N. Kellaris, V. G. Venkata, G. M. Smith, S. K. Mitchell, C. Keplinger, Peano-HASEL actuators: Muscle-mimetic, electrohydraulic transducers that linearly contract on activation. *Science Robotics*. **3**, eaar3276 (2018).

51. M. M. Sadeghi, H. S. Kim, R. L. B. Peterson, K. Najafi, Electrostatic Micro-Hydraulic . *Journal of Microelectromechanical Systems*. **25**, 557–569 (2016).

52. F. Carpi, G. Frediani, D. D. Rossi, Hydrostatically Coupled Dielectric Elastomer Actuators. *IEEE/ASME Transactions on Mechatronics*. **15**, 308–315 (2010).

53. S. K. Mitchell, X. Wang, E. Acome, T. Martin, K. Ly, N. Kellaris, V. G. Venkata, C. Keplinger, An Easy-to-Implement Toolkit to Create Versatile and High-Performance HASEL Actuators for Untethered Soft Robots. *Advanced Science*. **0**, 1900178.

54. J. Ou, M. Skouras, N. Vlavianos, F. Heibeck, C.-Y. Cheng, J. Peters, H. Ishii, (ACM Press, 2016; http://dl.acm.org/citation.cfm?doid=2984511.2984520), pp. 121–132.

55. R. Niiyama, X. Sun, C. Sung, B. An, D. Rus, S. Kim, Pouch Motors: Printable Soft Actuators Integrated with Computational Design. *Soft Robotics*. **2**, 59–70 (2015).

56. H. Sareen, U. Umapathi, P. Shin, Y. Kakehi, J. Ou, H. Ishii, P. Maes, (ACM Press, 2017; http://dl.acm.org/citation.cfm?doid=3025453.3025898), pp. 3669–3680.

57. F. Carpi, C. Salaris, D. D. Rossi, Folded dielectric elastomer actuators. *Smart Mater. Struct.* **16**, S300 (2007).

58. P. Coelho, A. Kaliontzopoulou, M. Rasko, A. van der Meijden, A ‘striking’ relationship: scorpion defensive behaviour and its relation to morphology and performance. *Functional Ecology*. **31**, 1390–1404 (2017).

59. S. Schlatter, P. Illenberger, S. Rosset, Peta-pico-Voltron: An open-source high voltage power supply. *HardwareX*. **4**, e00039 (2018).

60. D. McCoul, S. Rosset, N. Besse, H. Shea, Multifunctional shape memory electrodes for dielectric elastomer actuators enabling high holding force and low-voltage multisegment addressing. *Smart Mater. Struct.* **26**, 025015 (2017).

61. A. Poulin, M. Imboden, F. Sorba, S. Grazioli, C. Martin-Olmos, S. Rosset, H. Shea, An ultra-fast mechanically active cell culture substrate. *Scientific Reports*. **8**, 9895 (2018).

62. G. Moretti, M. Duranti, M. Righi, R. Vertechy, M. Fontana, in *Electroactive Polymer Actuators and Devices (EAPAD) XX* (International Society for Optics and Photonics, 2018; https://www.spiedigitallibrary.org/conference-proceedings-of-spie/10594/105940W/Analysis-of-dielectric-fluid-transducers/10.1117/12.2297082.short), vol. 10594, p. 105940W.

63. S. Pourazadi, A. Shagerdmootaab, H. Chan, M. Moallem, C. Menon, On the electrical safety of dielectric elastomer actuators in proximity to the human body. *Smart Mater. Struct.* **26**, 115007 (2017).

64. S. I. Rich, R. J. Wood, C. Majidi, Untethered soft robotics. *Nature Electronics*. **1**, 102–112 (2018).

65. H. Philamore, I. Ieropoulos, A. Stinchcombe, J. Rossiter, Toward Energetically Autonomous Foraging Soft Robots. *Soft Robotics*. **3**, 186–197 (2016).

66. C. Schunk, L. Pearson, E. Acome, T. G. Morrissey, N. Correll, C. Keplinger, M. E. Rentschler, J. S. Humbert, System Identification and Closed-Loop Control of a Hydraulically Amplified Self-Healing Electrostatic (HASEL) Actuator, 6.

67. Marette Alexis, Poulin Alexandre, Besse Nadine, Rosset Samuel, Briand Danick, Shea Herbert, Flexible Zinc–Tin Oxide Thin Film Transistors Operating at 1 kV for Integrated Switching of Dielectric Elastomer Actuators Arrays. *Advanced Materials*. **29**, 1700880 (2017).

68. P. Thummala, Z. Zhang, M. A. E. Andersen, D. Maksimovic, R. Sarban, in *2014 IEEE International Electric Vehicle Conference (IEVC)* (2014), pp. 1–8.

69. E.-F. M. Henke, S. Schlatter, I. A. Anderson, Soft Dielectric Elastomer Oscillators Driving Bioinspired Robots. *Soft Robotics* (2017), doi:10.1089/soro.2017.0022.

70. N. Kellaris, V. G. Venkata, P. Rothemund, C. Keplinger, An analytical model for the design of Peano-HASEL actuators with drastically improved performance. *Extreme Mechanics Letters*. **29**, 100449 (2019).

71. X. Wang, S. K. Mitchell, E. H. Rumley, P. Rothemund, C. Keplinger, High-Strain Peano-HASEL Actuators. *Advanced Functional Materials*. **30**, 1908821 (2020).

72. P. Rothemund, N. Kellaris, C. Keplinger, How inhomogeneous zipping increases the force output of Peano-HASEL actuators. *Extreme Mechanics Letters*. **31**, 100542 (2019).

73. R. D. Barnes, *Invertebrate zoology* (Saunders College, Philadelphia, PA, 1982).

74. C. A. Edwards, P. J. Bohlen, Biology and ecology of earthworms, Chapman and Hall Press. *London, United Kingdom.[Google Scholar]* (1996).

75. S. K. Sarna, Colonic Motility: From Bench Side to Bedside. *Colloquium Series on Integrated Systems Physiology: From Molecule to Function*. **2**, 1–157 (2010).

76. J. H. Sherman, D. S. Luciano, A. J. Vander, *Human physiology: the mechanisms of body function* (McGraw-Hill, 1985).

77. R. H. Baughman, Playing Nature's Game with Artificial Muscles. *Science*. **308**, 63–65 2005).

78. S. Lenz, B. Holz, S. Hau, S. Seelecke, Development of a high voltage source for dielectric elastomer actuators (DEA), 5.

79. X. Ji, X. Liu, V. Cacucciolo, M. Imboden, Y. Civet, A. E. Haitami, S. Cantin, Y. Perriard, H. Shea, An autonomous untethered fast soft robotic insect driven by low-voltage dielectric elastomer actuators. *Science Robotics*. **4** (2019), doi:10.1126/scirobotics.aaz6451.

80. M. Taghavi, T. Helps, J. Rossiter, Electro-ribbon actuators and electro-origami robots. *Science Robotics*. **3**, eaau9795 (2018).

81. S. Bauer, M. Paajanen, in *Smart Structures and Materials 2006: Electroactive Polymer Actuators and Devices (EAPAD)* (International Society for Optics and Photonics, 2006; https://www.spiedigitallibrary.org/conference-proceedings-of-spie/6168/61682K/Electromechanical-characterization-and-measurement-protocol-for-dielectric-elastomer-actuators/10.1117/12.674559.short), vol. 6168, p. 61682K.

82. C. Keplinger, M. Kaltenbrunner, N. Arnold, S. Bauer, Röntgen's electrode-free elastomer actuators without electromechanical pull-in instability. *PNAS*. **107**, 4505–4510 (2010).

83. T. A. Gisby, E. P. Calius, S. Xie, I. A. Anderson, in *Electroactive Polymer Actuators and Devices (EAPAD) 2008* (International Society for Optics and Photonics, 2008; https://www.spiedigitallibrary.org/conference-proceedings-of-spie/6927/69271C/An-adaptive-control-method-for-dielectric-elastomer-devices/10.1117/12.776503.short), vol. 6927, p. 69271C.

84. T. A. Gisby, S. Xie, E. P. Calius, I. A. Anderson, in *Electroactive Polymer Actuators and Devices (EAPAD) 2009* (International Society for Optics and Photonics, 2009; https://www.spiedigitallibrary.org/conference-proceedings-of-spie/7287/728707/Integrated-sensing-and-actuation-of-muscle-like-actuators/10.1117/12.815645.short), vol. 7287, p. 728707.

85. M. Landgraf, U. Zorell, T. Wetzel, S. Reitelshöfer, I. S. Yoo, J. Franke, in *Electroactive Polymer Actuators and Devices (EAPAD) 2015* (International Society for Optics and Photonics, 2015; https://www.spiedigitallibrary.org/conference-proceedings-of-spie/9430/943014/Dielectric-elastomer-actuators-as-self-sensing-devices--a-new/10.1117/12.2083572.short), vol. 9430, p. 943014.

86. B. O'Brien, T. Gisby, S. Q. Xie, E. Calius, I. Anderson, in *Electroactive Polymer Actuators and Devices (EAPAD) 2010* (International Society for Optics and Photonics, 2010; https://www.spiedigitallibrary.org/conference-proceedings-of-spie/7642/764220/Biomimetic-control-for-DEA-arrays/10.1117/12.847834.short), vol. 7642, p. 764220.

87. M. Landgraf, S. Reitelshöfer, J. Franke, M. Hedges, in *2013 3rd International Electric Drives Production Conference (EDPC)* (2013), pp. 1–7.

88. S. Reitelshöfer, M. Landgraf, I. S. Yoo, J. Hörber, C. Ramer, C. Ziegler, J. Franke, in *5th IEEE RAS/EMBS International Conference on Biomedical Robotics and Biomechatronics* (2014), pp. 803–808.

89. A. Marette, R. I. Haque, X. Ji, R. Hinchet, H. R. Shea, D. Briand, Triboelectric-TFT Flip-Flop for Bistable Latching of Dielectric Elastomer Actuators. *Advanced Electronic Materials*. **5**, 1900205 (2019).

90. R. Ruiz-Torres, O. M. Curet, G. V. Lauder, M. A. MacIver, Kinematics of the ribbon fin in hovering and swimming of the electric ghost knifefish. *Journal of Experimental Biology*. **216**, 823–834 (2013).

91. E. D. Youngerman, B. E. Flammang, G. V. Lauder, Locomotion of free-swimming ghost knifefish: anal fin kinematics during four behaviors. *Zoology*. **117**, 337–348 (2014).

92. S. Lee, K. Jung, J. Koo, S. Lee, H. Choi, J. Jeon, J. Nam, H. Choi, in *Smart Structures and Materials 2004: Electroactive Polymer Actuators and Devices (EAPAD)* (International Society for Optics and Photonics, 2004; https://www.spiedigitallibrary.org/conference-proceedings-of-spie/5385/0000/Braille-display-device-using-soft-actuator/10.1117/12.539739.short), vol. 5385, pp. 368–380.

93. K. Ly, N. Kellaris, D. McMorris, B. K. Johnson, E. Acome, V. Sundaram, M. Naris, J. S. Humbert, M. E. Rentschler, C. Keplinger, N. Correll, Miniaturized Circuitry for Capacitive Self-Sensing and Closed-Loop Control of Soft Electrostatic Transducers. *Soft Robotics* (2020), doi:10.1089/soro.2020.0048.

94. B. K. Johnson, V. Sundaram, M. Naris, E. Acome, K. Ly, N. Correll, C. Keplinger, J. S. Humbert, M. E. Rentschler, Identification and Control of a Nonlinear Soft Actuator and Sensor System. *IEEE Robotics and Automation Letters*. **5**, 3783–3790 (2020).

95. J. Cadick, *Electrical Safety Handbook* (McGraw-Hill Professional, 2012; https://lib.hpu.edu.vn/handle/123456789/20805).

96. IEC-479-2 | Effects of current passing through the human body. Part 2: Special aspects - Chapter 4: Effects of alternating current with frequencies above 100 Hz - Chapter 5: Effects of special waveforms of current - Chapter 6: Effects of unidirectional single impulse

currents of short duration | Document Center, Inc., (available at https://www.document-center.com/standards/show/IEC-479-2/history/).

97. O. Z. Roy, A. S. Podgorski, Tests on a shocking device—the stun gun. *Med. Biol. Eng. Comput.* **27**, 445–448 (1989).

98. R. M. Fish, L. A. Geddes, Conduction of Electrical Current to and Through the Human Body: A Review. *Eplasty*. **9** (2009) (available at https://www.ncbi.nlm.nih.gov/pmc/articles/PMC2763825/).

99. J. McMahon, S. K. Mitchell, K. Oguri, N. Kellaris, D. Kuettel, C. Keplinger, B. Bercovici, in *2019 IEEE Aerospace Conference* (2019), pp. 1–16.

100. R. E. Shadwick, D. A. Syme, Thunniform swimming: muscle dynamics and mechanical power production of aerobic fibres in yellowfin tuna (Thunnus albacares). *Journal of Experimental Biology*. **211**, 1603–1611 (2008).

101. H. Prahlad, R. Pelrine, S. Stanford, J. Marlow, R. Kornbluh, in *2008 IEEE International Conference on Robotics and Automation* (2008), pp. 3028–3033.

102. J. Guo, J. Leng, J. Rossiter, Electroadhesion Technologies for Robotics: A Comprehensive Review. *IEEE Transactions on Robotics*, 1–15 (2019).

103. J. Germann, B. Schubert, D. Floreano, in *2014 IEEE/RSJ International Conference on Intelligent Robots and Systems* (2014), pp. 3933–3938.

104. J. Guo, T. Bamber, J. Singh, D. Manby, P. A. Bingham, L. Justham, J. Petzing, J. Penders, M. Jackson, Experimental study of a flexible and environmentally stable electroadhesive device. *Appl. Phys. Lett.* **111**, 251603 (2017).

105. J. Guo, T. Bamber, M. Chamberlain, L. Justham, M. Jackson, Optimization and experimental verification of coplanar interdigital electroadhesives. *J. Phys. D: Appl. Phys.* **49**, 415304 (2016).

106. J. D. West, J. Mici, J. F. Jaquith, H. Lipson, Design and optimization of millimeter-scale electroadhesive grippers. *J. Phys. D: Appl. Phys.* **53**, 435302 (2020).

107. H. Prahlad, R. E. Pelrine, A. Wong-Foy, R. D. Kornbluh, B. K. McCoy, Materials for electroadhesion and electrolaminates (2016), (available at https://patents.google.com/patent/US9401668B2/en).

108. R. Chen, A Gecko-Inspired Electroadhesive Wall-Climbing Robot. *IEEE Potentials*. **34**, 15–19 (2015).

109. S. Diller, C. Majidi, S. H. Collins, in *2016 IEEE International Conference on Robotics and Automation (ICRA)* (2016), pp. 682–689.

110. J. Guo, K. Elgeneidy, C. Xiang, N. Lohse, L. Justham, J. Rossiter, Soft pneumatic grippers embedded with stretchable electroadhesion. *Smart Mater. Struct.* **27**, 055006 (2018).

111. G. Gu, J. Zou, R. Zhao, X. Zhao, X. Zhu, Soft wall-climbing robots. *Science Robotics*. **3**, eaat2874 (2018).

112. J. Cao, L. Qin, J. Liu, Q. Ren, C. C. Foo, H. Wang, H. P. Lee, J. Zhu, Untethered soft robot capable of stable locomotion using soft electrostatic actuators. *Extreme Mechanics Letters*. **21**, 9–16 (2018).

113. J. Guo, M. Tailor, T. Bamber, M. Chamberlain, L. Justham, M. Jackson, Investigation of relationship between interfacial electroadhesive force and surface texture. *J. Phys. D: Appl. Phys.* **49**, 035303 (2015).

114. J. Guo, T. Bamber, J. Petzing, L. Justham, M. Jackson, Experimental study of relationship between interfacial electroadhesive force and applied voltage for different substrate materials. *Appl. Phys. Lett.* **110**, 051602 (2017).

115. J. Guo, T. Hovell, T. Bamber, J. Petzing, L. Justham, Symmetrical electroadhesives independent of different interfacial surface conditions. *Appl. Phys. Lett.* **111**, 221603 (2017).

116. P. Rothemund, S. Kirkman, C. Keplinger, Dynamics of electrohydraulic soft actuators. *PNAS*. **117**, 16207–16213 (2020).

117. P. Rothemund, A. Ainla, L. Belding, D. J. Preston, S. Kurihara, Z. Suo, G. M. Whitesides, A soft, bistable valve for autonomous control of soft actuators. *Science Robotics*. **3** (2018), doi:10.1126/scirobotics.aar7986.

118. J. T. B. Overvelde, T. Kloek, J. J. A. D'haen, K. Bertoldi, Amplifying the response of soft actuators by harnessing snap-through instabilities. *PNAS*. **112**, 10863–10868 (2015).

119. R. Baumgartner, A. Kogler, J. M. Stadlbauer, C. C. Foo, R. Kaltseis, M. Baumgartner, G. Mao, C. Keplinger, S. J. A. Koh, N. Arnold, Z. Suo, M. Kaltenbrunner, S. Bauer, A Lesson from Plants: High-Speed Soft Robotic Actuators. *Advanced Science*. **7**, 1903391 (2020).

120. X. Cheng, M. Yu, J. Ma, B. Li, Y. Zhang, P. Wang, Z. Jiao, An entirely soft varifocal lens based on an electro-hydraulic actuator. *Smart Mater. Struct.* **29**, 045017 (2020).

121. H. Stoyanov, P. Brochu, X. Niu, C. Lai, S. Yun, Q. Pei, Long lifetime, fault-tolerant freestanding actuators based on a silicone dielectric elastomer and self-clearing carbon nanotube compliant electrodes. *RSC Advances*. **3**, 2272–2278 (2013).

122. W. Yuan, H. Li, P. Brochu, X. Niu, Q. Pei, Fault-tolerant silicone dielectric elastomers. *International Journal of Smart and Nano Materials*. **1**, 40–52 (2010).

123. C.-H. Li, C. Wang, C. Keplinger, J.-L. Zuo, L. Jin, Y. Sun, P. Zheng, Y. Cao, F. Lissel, C. Linder, X.-Z. You, Z. Bao, A highly stretchable autonomous self-healing elastomer. *Nat Chem*. **8**, 618–624 (2016).

124. T.-G. La, G.-K. Lau, Inhibiting electro-thermal breakdown of acrylic dielectric elastomer actuators by dielectric gel coating. *Appl. Phys. Lett.* **108**, 012903 (2016).

125. L. Huang, Z. Zhang, M. A. E. Andersen, in *2012 47th International Universities Power Engineering Conference (UPEC)* (2012), pp. 1–6.

126. M. Karpelson, G.-Y. Wei, R. J. Wood, Driving high voltage piezoelectric actuators in microrobotic applications. *Sensors and Actuators A: Physical*. **176**, 78–89 (2012).

127. M. Karpelson, G.-Y. Wei, R. J. Wood, in *2009 IEEE International Conference on Robotics and Automation* (2009), pp. 2217–2224.

128. P. Andersson, R. Forchheimer, P. Tehrani, M. Berggren, Printable All-Organic Electrochromic Active-Matrix Displays. *Advanced Functional Materials*. **17**, 3074–3082 (2007).

129. K. Takei, T. Takahashi, J. C. Ho, H. Ko, A. G. Gillies, P. W. Leu, R. S. Fearing, A. Javey, Nanowire active-matrix circuitry for low-voltage macroscale artificial skin. *Nature Materials*. **9**, 821–826 (2010).

130. B. M. O'Brien, E. P. Calius, T. Inamura, S. Q. Xie, I. A. Anderson, Dielectric elastomer switches for smart artificial muscles. *Appl. Phys. A*. **100**, 385–389 (2010).

131. N. Chau, G. A. Slipher, B. M. O'Brien, R. A. Mrozek, I. A. Anderson, A solid-state dielectric elastomer switch for soft logic. *Appl. Phys. Lett.* **108**, 103506 (2016).

132. D. Campolo, M. Sitti, R. S. Fearing, Efficient charge recovery method for driving piezoelectric actuators with quasi-square waves. *IEEE Transactions on Ultrasonics, Ferroelectrics, and Frequency Control*. **50**, 237–244 (2003).

133. M. Buchmann, Voltage multiplier with charge recovery (2008), (available at https://patents.google.com/patent/US7382634B2/en).

134. C. I. Honniball, P. G. Lucey, S. Li, S. Shenoy, T. M. Orlando, C. A. Hibbitts, D. M. Hurley, W. M. Farrell, Molecular water detected on the sunlit Moon by SOFIA. *Nature Astronomy*, 1–7 (2020).

135. R. D. Kornbluh, R. Pelrine, H. Prahlad, A. Wong-Foy, B. McCoy, S. Kim, J. Eckerle, T. Low, in *Electroactivity in Polymeric Materials*, L. Rasmussen, Ed. (Springer US, Boston, MA, 2012; https://doi.org/10.1007/978-1-4614-0878-9_3), pp. 67–93.

136. X. Liu, J. Zhang, H. Chen, Ambient humidity altering electromechanical actuation of dielectric elastomers. *Appl. Phys. Lett.* **115**, 184101 (2019).